

University of Strathclyde
Faculty of Science
Department of Physics

Czech Technical University in Prague
Faculty of Nuclear Sciences and Physical Engineering
Department of Physical Electronics

Developments for single molecule studies

by

Dalibor Pánek

A thesis presented in fulfilment of the requirements for
the degree of Doctor of Philosophy

2010

Declaration of authenticity

This thesis is the result of the author's original research. It has been composed by the author and has not been previously submitted for examination which has led to the award of a degree.

Copyright

The copyright of this thesis belongs to the author under the terms of the United Kingdom Copyright Acts as qualified by University of Strathclyde Regulation 3.50. Due acknowledgement must always be made of the use of any material contained in, or derived from, this thesis.

Acknowledgements

I would like to thank both my supervisors Professor David Birch and Doc. RNDr. Vlastimil Fidler, CSc. for their thoughtful guidance and patience. I am most grateful to them for giving me the opportunity to take part in the research. Thanks must be extended to Dr. Jan Olof Karolin for the close supervision of my projects, thorough discussions, and valuable advices.

I am indebted to all my colleagues and friends for their personal support and encouragement. My special thanks go to Ing. Miroslav Dvořák, Ph.D., Dr. Alison Cleary, Bc. Radka Havlíková, Dr. Gill Macnaught, and RNDr. Martin Michl, Ph.D.

I would also like to thank people from the mechanical and the electronic workshop for their help with technical issues, namely John Revie, John Broadfood, and Mark Hutcheon.

I would like to thank Scottish Universities Physics Alliance (SUPA) for awarding me a studentship.

Last but not least, I must thank to my family for their unconditional love and support.

Abstract

Single molecule fluorescence spectroscopy has attracted considerable attention over the past two decades. Measurement on a single entity provides an opportunity to avoid ensemble averaging which is always present in conventional bulk fluorescence measurements. This makes single molecule spectroscopy particularly interesting for biophysics and biochemistry where heterogeneous systems are often encountered.

The general interest of this thesis is in studies of single immobilised molecules carried out at room temperature. One of the major issues of single molecule spectroscopy is finding a suitable immobilising medium. Inorganic silica matrices prepared by the sol-gel method have a great potential to provide a close-to-natural immobilising environment even for sensitive biomolecules and thus allow investigation of their natural behaviour on the most fundamental level. In order to be able to tailor both physical and chemical properties of the final gel, it is of great importance to develop reliable methods to control each stage of polymerisation. In one part of this thesis, applications of fluorescent probes to investigation of sol-gels properties, as well as monitoring the gel assembly process, are discussed.

The thesis further presents studies of the genetically engineered glucose binding protein labelled with the environmentally sensitive dye badan. This system was developed in a search for an appropriate recognition-reporter unit to serve as a part of fluorescence-based sensor for continuous blood glucose monitoring. This labelled biomolecule represents an interesting subject for a single molecule study. Due to technical reasons however, single molecule spectroscopy could not be applied in this case. Therefore, conventional ensemble fluorescence spectroscopy methods were used to characterise behaviour of the labelled protein at different glucose concentrations.

The last part of the thesis deals with instrumental aspects of single molecule imaging and spectroscopy. The aim of the work was to assess the applicability of a freshly installed commercial microscope α -SNOM (WITec GmbH) in single molecule fluorescence studies and at the same time to adopt the technique for future experiments in our research group.

List of Publications

1. A.M. Macmillan, D. Pánek, C.D. McGuinness, J.C. Pickup, D. Graham, W. Ewen Smith, D.J.S. Birch, and J.O. Karolin. Improved biocompatibility of protein encapsulation in sol-gel materials, *Journal of Sol-Gel Science and Technology*, 49(2):380–384, 2009.
2. J. Karolin, D. Panek, A. MacMillan, O. Rolinski, and D. Birch. Fluorescence biosensing in nanopores. In *Engineering in Medicine and Biology Society, 2009. EMBC 2009. Annual International Conference of the IEEE*, pages 4154–4157. IEEE, 2009.
3. D. Pánek, J.O. Karolin, K. Wynne, and D.J.S. Birch. Alumina porous nano-structure characterised by fluorescence spectroscopy. Talk presented at *6th Prague Workshop on Photoinduced Molecular Processes (PIMoP)*, Prague, Czech Republic, April 2008
4. D. Pánek, J.O. Karolin, K. Wynne, and D.J.S. Birch. Fluorescence in hydrated Al₂O₃ nano-channel array. Poster presented at *SUPA 2008 annual meeting*, University of Glasgow, United Kingdom, June 2008
5. D. Pánek, J.O. Karolin, D.J.S. Birch. Engineering nanopores lit by fluorescence. Poster presented at *FluoroFest Workshop 2009*, Prague, Czech Republic, June 2009
6. A.M. Macmillan, J.O. Karolin, C.D. McGuinness, D. Pánek, J.C. Pickup, D.J.S. Birch. Single-molecule fluorescence detection of allophycocyanin (APC) entrapped in a silica sol-gel glass under physiological conditions. Poster presented at *10th Conference on Methods and Applications of Fluorescence: Spectroscopy, Imaging and Probes*, Salzburg, Austria, September 2007
7. A.M. Macmillan, D. Pánek, J.O. Karolin, C.D. McGuinness, J.C. Pickup, D.J.S. Birch. Replicating nature’s building blocks in silica sol-gel nanopores, Poster presented at *SUPA 2007 annual meeting*, University of Edinburgh, United Kingdom, June 2007

Glossary of abbreviations and mathematical symbols

A	absorbance
α, α_i	pre-exponential factor
AFM	atomic force microscopy
APC	allophycocyanin
APD	avalanche photodiode
badan	6-bromoacetyl-2-(dimethylamino)naphthalene
badan-GBP152C	badan-labelled H152C mutant of glucose binding protein
β	angle between transition dipole moments
β_i	pre-exponential factor of multi-exponential fluorescence anisotropy decay
CCD	charge coupled device
d	diameter or density
D	coefficient of diffusion
DDEM	donor–donor energy migration
E	energy
ϵ	molar absorption coefficient, extinction coefficient
ϵ_0	permittivity of vacuum
η	viscosity
FRET	Förster resonance energy transfer
FWHM	full width at half maximum
GBP	glucose binding protein
Γ	radiative decay rate
h	Planck constant
k	transition rate
k_B	Boltzmann constant
$I, I(t), I_0$	light intensity
IRF	instrument response function
J	overlap integral
k_B	Boltzmann constant
K_q	bimolecular quenching constant
κ^2	orientation factor

L	litre, dm ³
λ	light wavelength
μ	transition dipole moment or micro- ($\times 10^{-6}$)
n	index of refraction
\bar{N}	ratio of dye and particle concentrations
N_A	Avogadro constant
$N.A.$	numerical aperture
Nd:YAG	neodymium-doped yttrium aluminium garnet
[NP]	silica particle concentration
ν	light frequency
prodan	6-propionyl-2-(dimethylamino)naphthalene
PBS	phosphate buffered saline
ψ	atomic or molecular state wavefunction
Φ	quantum yield
r_0	fluorescence anisotropy in time zero
$r_{SS}, r(t)$	steady-state and time-resolved fluorescence anisotropy
R	radius
R_0	Förster radius
RET	resonance energy transfer
RhB	rhodamine B
Rh6G	rhodamine 6G
S_0, S_1, S_2	singlet states
SNOM	scanning near-field optical microscopy
SNR	signal-to-noise ratio
$S_{X:Y}$	stoichiometric ratio of components X and Y
σ	collision radius
t	time
T	temperature
T_1	triplet state
TAC	time-to-amplitude converter
TCSPC	time-correlated single photon counting
TMOS	tetramethyl orthosilicate
Trp	tryptophan
τ, τ_i	lifetime, i -th lifetime component
θ	rotational correlation time
[Q]	quencher concentration
V	volume

Contents

1	Introduction	1
2	Theory	5
2.1	Absorption	8
2.2	Fluorescence	8
2.2.1	Fluorescence lifetime	8
2.2.2	Quenching of fluorescence	9
2.2.3	Resonance energy transfer	11
2.2.4	Fluorescence anisotropy	12
2.3	Phosphorescence	14
2.4	Raman scattering	14
3	Experimental methods	16
3.1	Instrumentation and data collection	16
3.1.1	Steady-state spectra	16
3.1.2	Time-resolved fluorescence	17
3.1.3	Fluorescence microscopy	19
3.2	Data analysis	22
3.2.1	Fluorescence decay reconvolution	22
3.2.2	Fitting of electronic spectra	24
4	Host matrix studies	26
4.1	Interaction of Rhodamine 6G and colloidal silica	27
4.1.1	Introduction	27
4.1.2	Experimental results	30
4.1.3	Discussion	41
4.2	Perylene fluorescence quenched by cobalt ions in sol-gels	45
4.2.1	Introduction	45
4.2.2	Experimental results	46
4.2.3	Discussion	58
4.3	Improved biocompatibility of silica sol-gels	61
4.3.1	Introduction	61
4.3.2	Experimental	62
4.3.3	Results and discussion	63

5	Glucose sensing with engineered GBP	68
5.1	Introduction	68
5.2	Experimental	71
5.3	Results and discussion	72
5.3.1	Steady-state spectra	74
5.3.2	Time-resolved studies	75
6	Single molecule detection	86
6.1	Introduction	86
6.2	Experimental results	86
6.2.1	Sample preparation and impurity issues	87
6.2.2	Single molecule imaging	88
6.2.3	Single molecule spectra	92
6.2.4	Allophycocyanin single molecule fluorescence	94
6.3	Summary and discussion	96
7	Conclusion	98

Chapter 1

Introduction

Photophysical properties of a fluorophore are strongly influenced by interactions with its immediate environment. A fluorophore probes its surroundings with a volume of possibly a few cubic nanometers. Fluorescence thus provides a valuable interface between the microscopic and macroscopic world. This makes fluorescence spectroscopy an important analytical tool in medicine, biochemistry, biophysics, and material sciences. The recent progress in optical microscopy instrumentation made it possible to detect emission from a single fluorophore. Spectroscopic experiments on a single entity give an unprecedented opportunity to observe behavior which cannot be distinguished when classical ensemble spectroscopic methods are used. For instance, if a fluorophore can transfer between fluorescent and nonfluorescent states in both directions, the measurement of a single molecule fluorescence intensity reveals blinking of fluorescence. By analysis of traces of single molecule emission intensity, lifetimes of the two states can be directly measured and the heterogeneity of the ensemble can be assessed. When a large number of molecules is observed, their blinking is out of phase and one can measure only intensity that is averaged in both time and molecular ensemble.

Various techniques have been successfully employed for single molecule detection. These techniques include atomic force microscopy, electron microscopy, light absorption, fluorescence, and surface-enhanced Raman scattering. First spectroscopy experiments on single dopant molecules in condensed phase were performed in 1989 by Kador and Moerner. They used frequency modulation spectroscopy combined with either Stark or ultrasonic modulation of the absorption line to detect single pentacene in *para*-terphenyl crystal at 1.5 K in the far wings of the inhomogeneously broadened absorption spectrum [1, 2]. Orrit and Bernard demonstrated also on pentacene in *para*-terphenyl that much higher signal-to-noise ratio can be achieved when fluorescence excitation spectroscopy is used instead of doubly modulated absorption [3]. Since then, the number of publications on single molecule fluorescence spectroscopy has been rapidly growing, especially after it was demonstrated that single molecule detection is possible using confocal microscopy, which is relatively inexpensive and easy to implement.

Single molecule fluorescence detection is possible only when the background signal and detection noise are adequately suppressed so that the signal exceeds fluctuations [4, 5]. Modern semiconductor detectors have high efficiency and

low dark current. The dominant source of fluctuation are therefore stray light, scattered light, both elastically (Rayleigh) and inelastically (Raman), and autofluorescence¹. Many single molecule detection techniques therefore utilise various optical microscopy techniques to reduce the observed volume of the sample. At room temperature, single molecule fluorescence has been studied by scanning near-field optical microscopy, confocal microscopy, wide field epifluorescence, two-photon microscopy, total internal reflection microscopy, and using zero-mode waveguides [1, 4, 6–10].

There are two main approaches of single molecule fluorescence studies at room temperature – measurements on diffusing molecules and on immobilised molecules [7]. In the first method, fluorescence from a small volume (typically < 0.1 fL) of a diluted solution of a dye is monitored as a function of time. As fluorophores diffuse in and out, bursts of single molecule emission are observed. In this method, the time available for observation of a single molecule is limited by the time it takes for the molecule to diffuse through the volume. The observation time can be extended by using an appropriate immobilisation method. Thus, kinetic processes, such as enzyme catalysis and protein folding, can be observed for several seconds and longer. In order to prevent translational diffusion of a fluorophore, it can be tethered to a surface, covalently or non-covalently, or it can be entrapped in a transparent solid such as a polymer film or a gel.

Single molecule fluorescence spectroscopy is of particular interest for studies of biomolecular systems because they exhibit both single-molecule operations and heterogeneity [20–23]. To study processes such as protein folding or interaction between biomolecules on single molecule level, it is necessary to develop suitable immobilising aqueous environments that would preserve the nature of the investigated biomolecule. Entrapment can be achieved in water-filled organic gels like agarose or poly(acrylamide) gels. Inorganic silica matrices prepared by sol–gel method can also be used for biomolecule encapsulation with some unique advantages.

Although many useful information have been obtained from single molecule experiments, most of the articles, that were published before the work on this thesis started, were on proof-of-principle experiments that were carried out in order to establish and systematize the new methodology. The true expansion of applications of the technique was still expected to come. It is only recently that a notable commercial application of single molecule fluorescence spectroscopy was introduced by Pacific Biosciences – single molecule real time DNA sequencing [24, 25].

About this thesis

This thesis generally focuses on methods of single molecule imaging and spectroscopy of immobilised fluorophores carried out at room temperature. Particular attention is given to fluorescence methods of characterising material properties of inorganic silica sol–gel matrices as these can provide a suitable immobilising environment even for sensitive biomolecules.

¹ “It is not difficult to detect the fluorescence of a single molecule but not to detect anything else” – R. A. Keller

Chapter 2 gives an overview of theoretical fundamentals of interaction between photons and molecules with an emphasis on phenomena and concepts that are encountered in the following chapters. Main measurement and data analysis techniques are summarised in chapter 3 together with a description of instruments used in experiments.

The general topic of experimental projects presented in chapter 4 is the characterisation of inorganic silica matrices using absorption and fluorescence spectroscopy. Silica sol-gels are built from spherical particles, typically 2–5 nm in diameter, that are fused together into clusters. These clusters form a three-dimensional highly porous structure of almost fractal-like chains, resulting in a macroscopically solid, jelly-like material. The structure can be used for encapsulation of sensitive biomolecules such as proteins. In this case, a hydrated silica matrix is formed around individual protein molecules, which keeps them immobilised in a close-to-natural environment. Thus, sol-gels can be used as a host material for biomolecules in single molecule imaging and spectroscopy. Material properties of sol-gels are strongly dependent on the size distribution and the spatial arrangement of the nanoparticles in space. Fluorescence spectroscopy techniques are well suited for monitoring the assembly process as well as the resulting host matrix properties.

Section 4.1 deals with some aspects of a method of silica nanoparticle size measurement using fluorescence anisotropy decay analysis. When multiple fluorophores are attached to a surface of a small spherical particle, excitation energy migration between the fluorophores may occur, leading to depolarisation of fluorescence. Since the efficiency of the transfer is strongly dependent on the distance between the fluorophores, the phenomenon of energy migration can, in principle, be used to measure the size of a nanoparticle. Experiments presented in section 4.1 were carried out in order to test the possibility of using silica nanoparticles in a stabilised colloidal solution labelled by laser dye rhodamine 6G as a reference system to study donor-donor energy migration on a spherical surface.

Section 4.2 describes how structural changes during the sol-gel process influence dynamic quenching of perylene fluorescence by Co^{2+} ions. The aim was to extend previous study on possibility of using the perylene - Co^{2+} pair for characterisation of silica gel morphology based on recovering a donor-acceptor distance distribution function from a recorded fluorescence decay [26]. For such application, it is necessary to know the mechanism of fluorophore and quencher interaction through all stages of the sol-gel process.

In section 4.3 it is demonstrated how the environment-sensitive fluorescent probe prodan can be utilised for optimisation of protocols for protein encapsulation in silica sol-gels. The biocompatibility of a tetramethyl orthosilicate sol-gel monolith was demonstrated by preserving the trimer protein allophycocyanin in its native form for up to 500 h.

Chapter 5 presents photophysical properties of a genetically engineered glucose/galactose binding protein labelled with the environmentally sensitive dye badan. The labelled protein was designed by the group of professor John Pickup (King's College London) in an effort to develop a low-cost sensor for continuous monitoring of blood glucose via fluorescence [27]. The system exhibits an impressive glucose-induced change in fluorescence intensity which makes it a good candidate for clinical use. In conjunction with a suitable immobilisation method, the labelled protein could provide the ultimate single glucose molecule

sensitivity. Unfortunately, single molecule spectroscopy could not be applied to study this particular system due to technical reasons. Therefore, conventional ensemble fluorescence spectroscopy methods were used in this instance to characterise behaviour of the labelled protein at different concentrations of glucose.

Chapter 6 discusses practical aspects of single molecule imaging and spectroscopy. Although single molecule fluorescence spectroscopy is fast becoming a routine technique, its implementation is far from straightforward. One can expect that extensive experiments on a reference sample may be necessary in order to adopt the technique before it can be used to investigate a system of interest. Chapter 6 presents such introductory experiments on a freshly installed commercial microscope α -SNOM (WITec GmbH). The aim of the work was to become familiar with procedures of preparing samples for single molecule imaging and assess the applicability of the microscope in single molecule fluorescence spectroscopy.

Chapter 2

Theory

Visible absorption and emission spectra of atoms consist of distinct spectral lines which originate in transitions between discrete atomic energy levels. Light interacts with atoms by essentially three processes – *absorption*, *spontaneous emission* and *stimulated emission* [28].

If an atom in the ground state described by a wavefunction ψ_g is placed in electromagnetic field, it can undergo a transition to the excited state ψ_e by absorbing a quantum of the field with energy equal to the difference between the ground state and the excited state energy,

$$h\nu = E_e - E_g \quad (2.1)$$

The probability per unit time of transition from the ground to the excited state $\psi_g \rightarrow \psi_e$ is proportional to the spectral field energy density $\rho(\nu)$ (energy of electromagnetic field per unit volume and unit frequency interval),

$$w_{ge} = B_{ge}\rho(\nu)$$

where the constant of proportionality B_{ge} is called the Einstein coefficient for absorption. It can be shown that it is equal [29]

$$B_{ge} = \frac{2\pi^2|\boldsymbol{\mu}_{eg}|^2}{3\epsilon_0 h^2},$$

where $h = 6.626 \times 10^{-34}$ J s is the Planck constant and $\epsilon_0 = 8.854 \times 10^{-12}$ F m⁻¹ is the permittivity of vacuum. The transition dipole moment $\boldsymbol{\mu}_{eg}$ of the transition from the ground to the excited state with wavefunctions ψ_g and ψ_e respectively, is defined as

$$\boldsymbol{\mu}_{eg} = \int \psi_e^* \hat{\boldsymbol{\mu}} \psi_g d\mathbf{r} \quad (2.2)$$

where $d\mathbf{r} = dx dy dz$ and

$$\hat{\boldsymbol{\mu}} = e \left(\sum_i x_i, \sum_i y_i, \sum_i z_i \right)$$

is the dipole moment operator. The integration in 2.2 goes over all space. The size of the transition dipole moment can be regarded as the measure of the charge redistribution that accompanies the transition.

When the atom is found in the excited state, it can undergo a transition to the ground state while a photon of the energy given by 2.1 is released. This can happen either by stimulated emission or spontaneous emission. In the case of stimulated emission, the transition probability per unit time is given by

$$w_{eg}^{st} = B_{eg}\rho(\nu)$$

where $B_{eg} = B_{ge}$ is the Einstein coefficient for stimulated emission. The probability rates for both absorption stimulated emission are proportional to the intensity of the electromagnetic field. Spontaneous emission, on the other hand, is independent of the presence of the field. Its probability per second is

$$w_{eg}^{sp} = A_{eg} = \frac{16\pi^3\nu^3}{3\epsilon_0hc^3}|\boldsymbol{\mu}_{eg}|^2 = \frac{8\pi h\nu^3}{c^3}B_{eg}. \quad (2.3)$$

A_{eg} is called the Einstein coefficient for spontaneous emission.

In the case of polyatomic molecules, in addition to electronic transitions discussed above, transitions between rotational and vibrational states also occur. This leads to closely spaced groups of spectral lines [30, 31]. In liquids and solids, spectral lines are broadened due to collisions with surrounding molecules [32]. When the broadening is larger than the separation of different spectral lines, a spectral continuum arises.

Transitions between two different molecular states are constrained by *selection rules* [30, 31]. The rules are derived through the transition dipole integral

$$\int_{-\infty}^{\infty} \psi_2^* \hat{\boldsymbol{\mu}} \psi_1 d\mathbf{r}, \quad (2.4)$$

where the overall wavefunction $\psi_j, j = 1, 2$ can be in the Born-Oppenheimer approximation written as the product of individual vibrational, electronic, and spin wavefunctions, $\psi_j = \psi_{j,el} \times \psi_{j,vib} \times \psi_{j,sp}$ [30, 31]. The rotational contribution to the selection rules can be neglected in liquids and solids. If the integral in 2.4 is non-zero, the transition is allowed. If it is zero, the transition is forbidden. The selection rule for vibronic transitions (i.e. transitions with simultaneous change in electronic and vibrational energy levels), is called the *Franck-Condon principle*. It states that the probability of a vibronic transition is proportional to an overlap integral between vibrational wavefunctions of the two states that are involved in the transition,

$$\int \psi_{2,vib}^* \psi_{1,vib} d\mathbf{r},$$

the so-called Franck-Condon factor.

Figure 2.1 shows a diagram named after Polish physicist Aleksander Jabłoński [5, 31]. It is used to illustrate energy states of a molecule and transitions between them. The energy states are arranged vertically. The vibrational ground states of each electronic state are indicated by thick horizontal lines, higher (excited) vibrational states with thinner lines. There are many various versions of the Jabłoński diagram. In this particular diagram, radiative transitions, i.e. excitation and relaxation transitions accompanied by absorption or emission of a photon, are indicated by solid arrows pointing to the final state. Non-radiative processes are indicated by wavy arrows. A fluorophore is usually excited to a

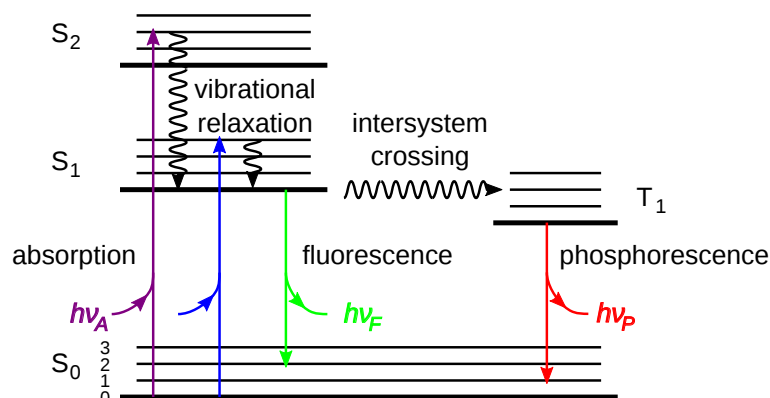


Figure 2.1: Jablonski diagram

higher vibrational state of S_1 or S_2 . In a condensed phase environment, absorption is followed by rapid (picosecond) *vibrational relaxation* to the lowest vibrational state of S_1 . The vibrational energy is dissipated through interaction of the molecule with its surrounding. Therefore it cannot occur in an isolated molecule. The molecule can then undergo a transition to the ground state, $S_1 \rightarrow S_0$, which is accompanied by emission of a photon. This process is called *fluorescence*. Because of the speed of vibrational relaxation, fluorescence generally occurs from the lowest vibrational state of S_1 . Therefore, the emitted fluorescence photon has lower energy than the absorbed photon - the fluorescence band is red-shifted in respect to the absorption. This phenomenon is called *Stokes shift*. Alternatively to fluorescence, the molecule can undergo *intersystem crossing* - a conversion to the triplet state, $S_1 \rightarrow T_1$. The radiative transition from T_1 to the ground state is known as *phosphorescence* ($T_1 \rightarrow S_0$) and for large organic molecules typically has a lifetime of the order of milliseconds to seconds. A molecule in S_1 can also directly transfer to a higher vibrational level of the ground state by non-radiative *internal conversion*, which can happen even in an isolated molecule in gas-phase.

In condensed phase media, the molecular photophysics is strongly affected by interaction of the fluorophore with its environment. A fluorophore dissolved in a liquid solvent is close to equilibrium with surrounding solvent molecules. If it is electronically excited by absorption of a photon, the charge redistribution accompanying the transition causes that solvent molecules interacting with the fluorophore start to reorient in order to establish new equilibrium with the excited molecule. This rearrangement is known as *solvent relaxation*. The energy difference between the non-relaxed (so-called the *Franck-Condon state*) and the relaxed state is larger for more polar solvent. Therefore, the position of the emission band is shifted to longer wavelengths with increasing polarity of the solvent. In general, fluorophores that are polar themselves (such as badan or prodan) are more sensitive to solvent polarity than non-polar dyes (perylene, pyrene).

Until new equilibrium between the solvent and the excited molecule is established, fluorescence occurs from partially relaxed energy states. This can be monitored by time-resolved spectroscopy as the dynamic Stokes shift of fluores-

cence spectra. The rate of solvent relaxation depends on the solvent viscosity. For small solvent molecules (water, methanol) at room temperature, it happens on much faster time scale than nanosecond fluorescence and femtosecond spectroscopy techniques, such as fluorescence up-conversion, must be used to resolve the solvation dynamics [33]. If the time scale of solvent relaxation is comparable to the lifetime of the excited state (e.g., in the hydrophobic backbone region of a phospholipid bilayer [34]), the process can be resolved with time-correlated single photon counting technique described in chapter 3.

2.1 Absorption

Light passing through a media containing a dye is attenuated due to the process of light absorption. The intensity I of the light transmitted through the sample is given by the *Lambert-Beer law*,

$$I = I_0 10^{-\epsilon c L}, \quad (2.5)$$

where I_0 is the intensity of the incident light, ϵ is the (decadic) molar absorption coefficient (usually given in units $\text{M}^{-1}\text{cm}^{-1}$), c the dye concentration (in $\text{mol} \times \text{litre}^{-1} = \text{M}$) and L is the light path length through the sample (given in cm). The molar absorption coefficient ϵ , also called the extinction coefficient, describes the ability of a chromophore to absorb light - it is directly proportional to the cross-section for absorption. *Absorbance* (or optical density) of the sample is defined as

$$A = -\log_{10} \frac{I}{I_0} = \epsilon c L. \quad (2.6)$$

2.2 Fluorescence

Inspection of fluorescence properties – spontaneous photoemission following after absorption of light – can yield various information about the fluorophore and its environment. Several concepts and phenomena related to fluorescence, that are relevant in the context of this thesis, are introduced in this section.

2.2.1 Fluorescence lifetime

Suppose we have an ensemble of molecules that are excited at the same time $t = 0$ by an infinitesimally short pulse of light (so-called δ -function) from the ground state S_0 to the excited state S_1 . The excited state is depopulated by radiative transitions with the rate Γ (fluorescence) and non-radiative transitions with the rate k_{nr} . The change of the excited state population N_1 in the time t after excitation is given by

$$\frac{dN_1}{dt} = -(\Gamma + k_{nr})N_1. \quad (2.7)$$

Reciprocal of the radiative decay rate, $\tau_r = \frac{1}{\Gamma}$, is called the *radiative lifetime*, or sometimes the *natural lifetime*. It is the lifetime of an excited molecule in the absence of non-radiative transitions. In some cases (e.g. perylene), the

radiative decay rate can be calculated from absorption and emission spectra corresponding to $S_0 \leftrightarrow S_1$ transitions, using

$$\Gamma \simeq 2.88 \times 10^9 n^2 \frac{\int I(\nu) d\nu}{\int \nu^{-3} I(\nu)} \int \nu^{-1} \epsilon(\nu) d\nu, \quad (2.8)$$

where n is the index of refraction, $I(\nu)$ is the fluorescence emission density (as a function of wavenumber ν), $\epsilon(\nu)$ is the molar absorption coefficient. This formula does not account for an interaction with the solvent or a change of geometry of the excited state.

Integration of 2.7 gives

$$\ln(N_1) = \int \frac{dN_1}{N_1} = \int -(\Gamma + k_{nr}) dt = -(\Gamma + k_{nr})t + \text{const.} \quad (2.9)$$

so, the excited state population develops in time according to

$$N_1(t) = N_1(0) \exp[-(\Gamma + k_{nr})t] = N_1(0) e^{-\frac{t}{\tau}}, \quad (2.10)$$

where

$$\tau = \frac{1}{\Gamma + k_{nr}} \quad (2.11)$$

is the excited state lifetime. Equation 2.10 can be interpreted in terms of observed fluorescence intensity, i.e.

$$I(t) = I_0 e^{-\frac{t}{\tau}} \quad (2.12)$$

The *fluorescence quantum yield* is a measure of the efficiency with which the absorbed light produces fluorescence. It is defined as the number of photons emitted due to radiative transitions from S_1 to S_0 per one absorbed photon,

$$\Phi_F = \frac{\text{number of photons emitted}}{\text{number of photons absorbed}}. \quad (2.13)$$

By definition, the fluorescence quantum yield is the ratio of the radiative decay rate to the overall rate of de-excitation processes, thus

$$\Phi_F = \frac{\Gamma}{\Gamma + k_{nr}} = \frac{\tau}{\tau_r}. \quad (2.14)$$

2.2.2 Quenching of fluorescence

Any process which leads to a decrease of fluorescence intensity is called *fluorescence quenching*. Apart from trivial effects, such as a change in optical properties of the sample or irreversible destruction of the fluorophore molecular structure, it can be caused, for instance, by a long-range energy transfer to an acceptor molecule, complex formation, and collisions. If the quencher interacts with the fluorophore in the excited state, the process is referred to as *dynamic quenching*. When the interaction inhibits excitation to occur, for example by the formation of a ground state complex, it is referred to as *static quenching*. A convenient way to distinguish whether the decrease of the fluorescence intensity is caused by static or dynamic quenching is to study the lifetime of the fluorophore in presence and absence of the quencher. In the case of static

quenching, the number of fluorophore molecules able to emit a photon after photoexcitation decreases, while the photophysics of unquenched fluorophores remains unaltered. On contrary, dynamic quenching increases the non-radiative decay rate, thus the fluorescence lifetime decreases.

Static quenching is caused by the formation of a non-fluorescent ground state complex between the fluorophore and the quencher. Immediately after such a complex absorbs light, it returns to the ground state by radiationless de-excitation. The complex has unique photophysical properties - it often exhibits an absorption spectrum that is different from the fluorophore and the quencher spectrum. Even in the absence of a quencher, self-quenching of fluorescence may occur due to the formation of non-fluorescent dye aggregates.

An important case of dynamic quenching is collisional quenching which is caused by diffusive encounters. This type of quenching requires molecular contact of the excited fluorophore and the quencher within the van der Waals radii. Therefore, the quenching is sensitive to factors influencing the rate of collisions. There are several de-excitation mechanisms upon contact between the fluorophore and the quencher, for example photo-induced electron transfer, Dexter energy exchange and heavy atom effect. It is often difficult to determine which effect is responsible for quenching. In addition, quenching can be caused by a combination of different mechanisms.

The frequency of collisions between the fluorophore and the quencher is proportional to the quencher concentration, $\sim K_0[Q]$. The proportionality constant, K_0 , is the bimolecular rate constant. It can be calculated from the *Smoluchowski equation*

$$K_0 = 4\pi N_A(\sigma_f + \sigma_q)(D_f + D_q) = 4\pi N_A\sigma D$$

where $N_A = 6.022 \times 10^{23}$ is the Avogadro constant, σ is the collision radius, and D is the sum of diffusion coefficients of the fluorophore and the quencher. Since not all collisions result in quenching of the excited fluorophore, a quenching efficiency f_q is included in the equation for the quenching rate

$$k_q = K_q[Q] = f_q K_0[Q], \quad (2.15)$$

where $K_q = f_q K_0$ is the bimolecular quenching constant which reflects the quenching efficiency or accessibility of the fluorophore by the quencher.

Quenching due to collisions introduces an additional non-radiative de-excitation mechanism which depopulates the fluorophore excited state. Equation 2.7 is then modified to

$$\frac{dN_1}{dt} = -\left(\frac{1}{\tau_0} + K_q[Q]\right) N_1, \quad (2.16)$$

where τ_0 is the fluorescence lifetime of the fluorophore in absence of the quencher. The fluorescence intensity then decays as

$$I(t) = I_0 \exp\left[-t\left(\frac{1}{\tau_0} + K_q[Q]\right)\right] = I_0 e^{-\frac{t}{\tau}}.$$

Fluorescence decays exponentially with the lifetime τ that is reduced compared to τ_0 due to collisions of the fluorophore with the quencher according to

$$\frac{1}{\tau} = \frac{1}{\tau_0} + K_q[Q] \quad (2.17)$$

Transient effects in quenching

In reality, a fluorescence decay in some cases becomes non-exponential in presence of a quencher due to transient effects [36–38]. Due to the evolution of the ensemble of fluorophores, the rate of collisions between the fluorophore and the quencher is time-dependent (assuming $f_q = 1$),

$$K_q(t) = 4\pi N_A \sigma D \left[1 + \sigma(\pi D t)^{-1/2} \right].$$

The time dependence originates in a random distribution of distances between fluorophores and quenchers. Excited fluorophores located closer to quenchers are quenched more rapidly. The excited state population then decays as

$$\frac{dN_1}{dt} = - \left(\frac{1}{\tau_0} + K_q(t)[Q] \right) N_1. \quad (2.18)$$

The decay law for the fluorescence intensity is then

$$I(t) = I_0 \exp \left[-at - 2b\sqrt{t} \right], \quad (2.19)$$

where

$$\begin{aligned} a &= \frac{1}{\tau_0} + 4\pi D \sigma N_A [Q], \\ b &= 4\sigma^2 N_A \sqrt{\pi D} [Q]. \end{aligned} \quad (2.20)$$

Stern-Volmer plot

Equation 2.17 can be re-written for the steady-state fluorescence intensity,

$$\frac{\tau_0}{\tau} = \frac{I_0}{I} = 1 + K_q \tau_0 [Q] \quad (2.21)$$

which is referred to as the *Stern-Volmer equation*. Plot of I_0/I dependence on the quencher concentration, $[Q]$, is called the *Stern-Volmer plot*, which is used to inspect the quenching process. According to 2.21, the dependence is expected to be linear, intercepting one on y -axis. The slope of the dependence – the Stern-Volmer constant – is equal to $K_q \tau_0$ in the case of exclusively collisional quenching. Static quenching also results in linear Stern-Volmer plot, but, unlike in the case of collisional quenching, τ_0/τ does not depend on the quencher concentration. A Stern-Volmer plot can deviate from linearity for various reasons.

2.2.3 Resonance energy transfer

Another mechanism of dynamic fluorescence quenching is *resonance energy transfer* (RET), also called *Förster resonance energy transfer* (FRET), or, inappropriately, fluorescence resonance energy transfer. It is a long-range radiationless transfer of excitation energy from a fluorescent donor to an acceptor which happens through Coulombic interaction often called a dipole-dipole coupling. RET can also occur between two entities of the same species, i.e. two fluorophores. The rate of RET depends on the donor-acceptor distance, an overlap of the donor emission and the acceptor absorption spectra, and the relative orientation of transition dipole moments of the donor and the acceptor.

The rate constant of RET depends on the distance R between the donor and the acceptor as

$$k_T(t) = \frac{1}{\tau_D} \left(\frac{R_0}{R} \right)^6, \quad (2.22)$$

where τ_D is the excited state lifetime of the donor in absence of the acceptor and R_0 is so-called *Förster distance*. By definition, the efficiency of energy transfer at $R = R_0$ is 50%. Förster distance can be calculated from

$$R_0^6 = \frac{9 \times 10^{-3} (\ln 10) \kappa^2 \Phi_D}{128 \pi^5 N_A n^4} \int_0^\infty \lambda^4 I_D(\lambda) \epsilon(\lambda) d\lambda, \quad (2.23)$$

(λ is in m and the result is in m⁶), where κ^2 is the factor describing the relative orientation in space of transition dipoles of the donor and the acceptor, Φ_D is the donor quantum yield, N_A is the Avogadro constant, n the refractive index, λ the wavelength, $I_D(\lambda)$ the spectral radiant intensity of the donor, and ϵ_A is the molar decadic extinction coefficient of the acceptor. The term

$$J = \int_0^\infty \lambda^4 I_D(\lambda) \epsilon(\lambda) d\lambda$$

is called the *overlap integral*. The extinction coefficient is given in units of M⁻¹cm⁻¹ and the wavelength is in nanometers. The Förster distance can be calculated using the simplified formula

$$R_0 = 9.78 \times 10^3 (\kappa^2 n^{-4} \Phi_D J)^{1/6} \quad (\text{Å})$$

where the result is in angstroms (1 Å = 10⁻¹⁰ m).

The *orientation factor* κ^2 can in principle take values from 0 (perpendicular transition moments) to 4 (collinear and in line). For randomly oriented dipole moments (e.g. in fluid solutions), $\kappa^2 = \frac{2}{3}$. The donor fluorescence intensity decays as

$$I(t) = I_0 \exp \left[-\frac{t}{\tau_D} - 2\gamma \sqrt{\frac{t}{\tau_D}} \right], \quad (2.24)$$

The parameter γ is given by

$$\gamma = \frac{2\pi^{3/2} N_A R_0^3 [A]}{3} = \frac{[A]}{[A_0]},$$

where $[A]$ is the acceptor concentration given in mol m⁻³ and $[A_0] = \frac{3}{2\pi^{3/2} N_A R_0^3}$ is the critical concentration.

2.2.4 Fluorescence anisotropy

Polarised light is preferentially absorbed by fluorophores with their transition moments aligned parallel to the direction of the excitation light polarization. This results in a partially oriented population of excited fluorophores and in partially polarised fluorescence emission. Fluorescence anisotropy is defined as

$$r = \frac{I_{\parallel} - I_{\perp}}{I_{\parallel} + 2I_{\perp}} \quad (2.25)$$

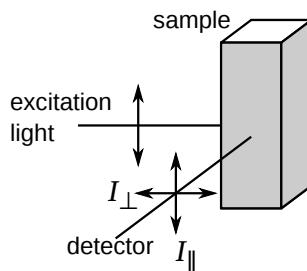


Figure 2.2: To the definition of fluorescence anisotropy

where I_{\parallel} is the intensity of fluorescence polarized vertically (i.e. in parallel to the vertically polarized excitation light) and I_{\perp} is the intensity of fluorescence polarized horizontally (see figure 2.2). There are several phenomena that can lower the anisotropy value. In a homogeneous solution of fluorophores, the fluorescence is depolarized by rotational diffusion. For a non-spherical molecule, the anisotropy decays with up to five correlation times

$$r(t) = \sum_{i=1}^5 r_{0i} e^{-\frac{t}{\theta_i}},$$

where θ_i are correlation times and r_{0i} are fractional anisotropies. The anisotropy $r = \sum_i r_{0i}$ at $t = 0$ is equal to

$$r_0 = \frac{3 \cos^2 \beta - 1}{5},$$

where β is the angle between the absorption and emission dipole moments of the fluorophore. Therefore, r_0 takes value between -0.2 (perpendicular dipole moments) and 0.4 (parallel). At $\beta = 54.7^\circ$, so-called *magic angle*, $r_0 = 0$.

The anisotropy decay function depends on the geometry of the fluorophore, the orientation of transition dipole moments within the dye molecule, and interaction with surrounding solvent molecules. Since some correlation times can be very close in magnitude, the number of anisotropy decay parameters can decrease. In practice, no more than three correlations times are expected. For an isotropically rotating molecule, all correlation times equal in magnitude, and the decay of anisotropy is single-exponential

$$r(t) = r_0 e^{-\frac{t}{\theta}}, \quad (2.26)$$

with the *rotational correlation time*¹

$$\theta = \frac{\eta V}{k_B T}, \quad (2.27)$$

where η is the viscosity, $V = 4/3\pi r^3$ is the volume of the rotating sphere, $k_B = 1.38 \times 10^{-23} \text{ J}\cdot\text{K}^{-1}$ is the Boltzmann constant, and T is the temperature in

¹The correlation time is related to the *rotational diffusion coefficient* D_r by $\theta = (6D_r)^{-1}$. For a sphere, $D_r = \frac{k_B T}{8\pi r^3 \eta}$

kelvin, K. Thus, the measurement of anisotropy decays can be used for example to estimate the size and the shape of a rotating object labelled with a fluorescent probe.

The molecule of Rhodamine 6G is an example of a spherical rotor with single-exponential anisotropy decay. The anisotropy decay of perylene, on the other hand, is two-exponential.

The value of steady-state fluorescence anisotropy can be calculated according

$$r_{ss} = \frac{\int_0^\infty r(t)I(t)dt}{\int_0^\infty I(t)dt}. \quad (2.28)$$

In the general case, when both fluorescence and anisotropy decay multi-exponentially, 2.28 becomes

$$r_{ss} = \frac{\sum_i \sum_j \frac{\tau_i \alpha_i \theta_j r_{0j}}{\tau_i + \theta_j}}{\sum_k \tau_k \theta_k}$$

2.3 Phosphorescence

Photoemission due to the transition from the first triplet state T_1 to the ground state S_0 is called phosphorescence. Triplet states have a different spin multiplicity than singlet states. The molecule can transfer to a triplet state from a photo-excited singlet state by so-called intersystem crossing. The transition from T_1 to the ground state S_0 , is “forbidden” because it must be accompanied by the change of the spin multiplicity. Phosphorescence still occurs, it happens however on a significantly longer time scale than fluorescence, typically milliseconds. Some compounds have triplet state lifetimes of the order of minutes or even several hours. In liquid solutions at room temperature, phosphorescence is kinetically unfavoured and most molecules in the triplet state return to ground state by non-radiative paths prior to emission. This results in a low quantum yield of phosphorescence.

If fluorescence from a single fluorophore is observed, a transition to a triplet state leads to decrease of fluorescence signal - the fluorophore image disappears. When the fluorophore returns to the ground state from the triplet state within the observation period, fluorescence switching on and off (blinking) is observed.

2.4 Raman scattering

Most of the light scattered by a sample has the same wavelength as the excitation light, i.e. it is scattered elastically (*Rayleigh scattering*). A small fraction of the scattered light has the wavelength different from that of the excitation light. This is caused by inelastic *Raman scattering*. Unlike in the case of Rayleigh scattering, Raman scattering is accompanied by a change in rotational, vibrational, or electronic energies of interacting molecules. In the case of liquids and solid materials, transitions occur between different vibrational levels. An incident photon is absorbed and emitted by the molecule of the scattering medium via a virtual electronic state. The energy difference between the incident and the scattered light is equal to the difference between the energy levels of the molecule. The scattered light can have either lower or higher energy than the incident light. If the molecule ends up in a higher energy state, the scattered

light is red-shifted, we talk about Stokes shift. Anti-Stokes (blue) shift occurs, when the molecule loses its energy in the scattering process. The shape of the Raman spectrum is given by selection rules and the occupation of different rotational-vibrational energy states. Stokes and anti-Stokes bands are symmetrically distributed around the Rayleigh band. In thermal equilibrium, the population of lower energy states is higher (given by Boltzmann distribution), which means that Stokes bands have higher intensities than anti-Stokes.

When studying fluorescence of dye molecules dissolved in a liquid solvent or doped in a solid media (such as glass), the spectrum of the light inelastically scattered by the host material may overlay with the dye fluorescence and significantly distort recorded spectra. The presence of a Raman peak is often observed when working with dilute solutions or a dye with low-quantum yield. The energy difference between the excitation and the scattered light is independent on the wavelength of the excitation light. It is given by the difference between vibrational energy levels of the solvent. Therefore, Raman bands can be identified by changing the excitation wavelength and evaluating the shift of bands in the spectrum.

In single molecule fluorescence imaging, the scattered and the reflected excitation light significantly contributes to the background signal, which limits the signal-to-noise ratio. Unlike the reflected and the elastically scattered light, Raman bands overlaying with the monitored fluorescence band cannot be filtered out by the use of cut-off filters. The necessity of reducing the background signal is the reason why techniques such as near-field, total reflection, and confocal microscopy are used in order to minimize the observed volume and thus reduce Raman scattering.

Chapter 3

Experimental methods

In this chapter, main experimental techniques used in this thesis are introduced together with a brief description of measuring devices. Principles of measuring methods are presented with emphasis on time-resolved fluorescence measurement and fluorescence confocal microscopy. Methods used for statistical analysis of recorded fluorescence decays and spectra are also explained here.

3.1 Instrumentation and data collection

3.1.1 Steady-state spectra

Absorption

Absorption spectra were recorded with Lambda 2 UV/Vis (PerkinElmer) spectrophotometer or UV 1601 (Schimadzu). Both instruments work on the same principle. Two light sources are used – a halogen lamp for measurements in the visible region, 350 - 900 nm, and a deuterium lamp to cover the UV region down to 190 nm. A single-grating monochromator is used to select the required wavelength from the continuous spectrum produced by the appropriate lamp. The quasi-monochromatic light is routed to the sample compartment. The light transmitted through a sample (usually contained in a square cuvette with 1 cm path length) is then monitored by a detector. The detector signal is recorded while the wavelength of the light is scanned. Most spectrometers allow to correct for the background by measurement in *double-beam geometry*, in which the difference between two signals is recorded – one light beam is passing through the studied sample, second through a “blank” sample, containing the host medium only. However, it turned out that for the experiments presented here, the most reliable method was to record the sample absorption spectrum and the background spectrum separately and subtract them afterwards. This approach allows for better control over various influences affecting the measurement. The background originates in the absorption of light by the solvent itself, scattering, and reflections from the cuvette walls. Because the material and the geometry of each cuvette may differ slightly, when possible, the background and sample absorption were recorded using the same cuvette.

Fluorescence

Steady state fluorescence spectra were recorded with FluoroMax-2 (ISA/Jobin Yvon/Spex) spectrofluorometer. It comprises of a xenon (Xe) lamp for excitation, two monochromators (one for selecting excitation wavelength and second for emission) with adjustable slits for selecting the bandwidth and a R928 (Hamamatsu) photomultiplier. The excitation and emission spectra were recorded by scanning the respective monochromator, while keeping the other wavelength fixed. Fluorescence emission spectra presented in this thesis have not been corrected for the wavelength dependency of the detector quantum efficiency.

For recording steady state anisotropy spectra with FluoroMax-2, a manually controlled, home-built polariser holder was used. Grating monochromators are usually polarising the transmitted light to some extent, which results in different detection sensitivity for vertically and horizontally polarised light. Therefore, a scaling factor must be also recorded for each wavelength – so-called *G-factor*. It is defined as

$$G(\lambda) = \frac{S_V(\lambda)}{S_H(\lambda)},$$

where S_V and S_H are the detection sensitivities for vertically and horizontally polarised emission. *G-factor* can be calculated using

$$G(\lambda) = \frac{I_{HV}(\lambda)}{I_{HH}(\lambda)}, \quad (3.1)$$

where $I_{HV}(\lambda)$ is the intensity recorded with the excitation polariser in horizontal position (i.e., blocking the vertically polarized light) and the emission polariser in the vertical position. $I_{HH}(\lambda)$ is defined accordingly. The anisotropy is then

$$r = \frac{I_{VV} - G \times I_{VH}}{I_{VV} + 2G \times I_{VH}}. \quad (3.2)$$

3.1.2 Time-resolved fluorescence

Decays of fluorescence were measured by *time correlated single photon counting* (TCSPC) which is a well established method in time-resolved fluorescence spectroscopy. A modular system based on FluoroCube (HORIBA Jobin Yvon) lifetime spectrofluorometer was used for recording of fluorescence decays. For fluorescence excitation, a set of pulsed light emitting diodes and laser diodes (IBH NanoLED) was available. The *full width at half maximum* (FWHM) of pulses is $\lesssim 300$ ps for diode lasers and ~ 1 ns for light emitting diodes. Depending on the experimental set-up, monochromators or sheet polarisers could be included in the excitation and emission path. An IBH TBX-04 photomultiplier module was used as a detector. To recover fluorescence kinetics from recorded decay data by reconvolution (see 3.2.1), Decay Analysis Software v6.1 (DAS6, IBH) was used [39].

Time Correlated Single Photon Counting is one of the most common techniques for measuring fluorescence lifetimes. The principle of the method is repetitive measurement of the relative interval between the moment of excitation and photon emission [40]. The higher number of photon detection event is accumulated, the higher is the statistical precision. TCSPC can be employed in both ensemble and single-molecule measurements.

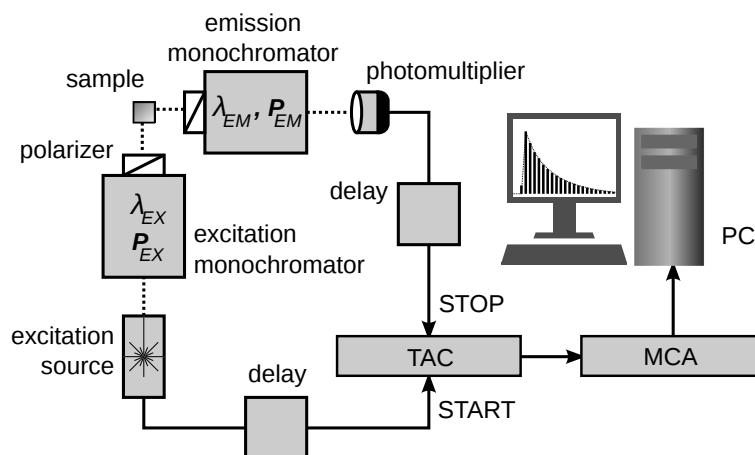


Figure 3.1: Principle layout of a TCSPC experiment

Principle of TCSPC operation

The diagram of the TCSPC principal set up is shown in figure 3.1. A pulsed light source repetitively excites the sample. A signal that is synchronous with the excitation source is fed to the START input of the *time-to-amplitude converter* (TAC). The synchronisation signal may be derived from the excitation source using a photo-diode, photomultiplier, or the drive circuit of the power supply. Upon detection of an electrical pulse on the START input, a condenser built in the TAC starts to charge up by a constant current. The signal from the detector of fluorescence is connected to the STOP input of the TAC. Charging of the condenser is stopped when a fluorescence photon is detected and a pulse with an amplitude proportional to the capacitor voltage is generated at the output of the TAC. The amplitude of the pulse is proportional to the time interval between START and STOP pulses arrival. In the case that no STOP pulse is detected during an interval called the *TAC range*, the capacitor is discharged and no output is generated. The TAC output is analysed by a multichannel analyser (MCA) which is usually accomplished by a specialized computer card. The electrical pulse amplitude is converted by a calibrated digital-to-analog converter to a time channel and stored in the computer memory. A histogram of the number of photon detection in each time channel is then constructed. The histogram resembles a fluorescence decay of the sample convoluted with the response of the instrument.

Pile-up effect

Multiple detection during a single excitation cycle leads to the so-called “pile-up problem”. The principle of TAC operation described above allows only the first detection event to be recorded. If there is a probability of detecting more than one photon during a single excitation cycle, the resulting histogram seemingly indicates a higher probability of photon detection in shorter times after excitation. To avoid this histogram distortion, the intensity upon the fluorescence detector must be controlled to ensure that no more than a single photon

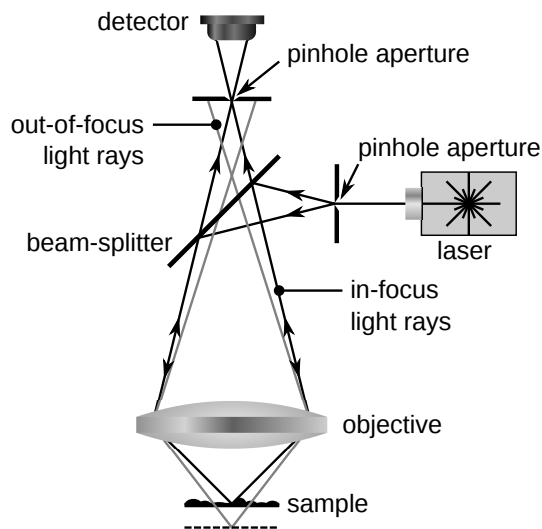


Figure 3.2: Principle set up of a confocal microscope

is detected during one excitation cycle. In practice, the number of fluorescence photon detection per second is kept smaller than 2% of the excitation pulse rate.

Reverse mode of operation

The TCSPC diagram depicted in figure 3.1 is the set up in so-called *forward mode* of operation. A START signal has the same frequency as the excitation source. During the majority of TAC cycles, STOP pulses do not arrive within the TAC range interval and the TAC is kept busy much more than needed. Since the photon detection per second must be limited due to the pile-up problem, it is advantageous to excite the sample with highest possible frequency that allows depopulation of all fluorophores during the excitation cycle. At higher repetition rates, the forward mode of operation has a clear disadvantage. The proportion of the STOP pulse rate and the TAC output rate significantly increases. This is because the number of operation cycles of the TAC is limited by the length of a reset period (the *dead time*) during which the TAC does not accept any input. The probability of the STOP pulse arriving during the reset cycle increases and many detection events are lost. In order to utilize full potential of the TAC, TCSPC can be operated in the *reverse mode* in which the fluorescence detector is connected to the START input of the TAC and excitation source synchronisation signal is connected to the STOP input. In the reverse mode, the STOP pulse should be delayed to ensure that it arrives at the TAC input later than the START pulse.

3.1.3 Fluorescence microscopy

The principal set up of a confocal microscope is shown in figure 3.2. A point-like light source is focused by an objective onto a sample. The reflected light or fluorescence is then focused by the same objective into a pinhole placed in front

of a detector. The pinhole transmits only the central part of the focused beam. Rays that do not come from the objective focal plane (indicated by grey lines in figure 3.2) can not reach the detector, which enhances the contrast strongly. Alternatively, the transmitted excitation light or fluorescence from the sample can be collected by a second objective. The image is formed by line-by-line scanning across the sample and recording the detector signal from each point of the scanned area. This can be accomplished either by scanning the sample placed on a piezoelectric stage or by scanning the beam by a pair of mirrors. The beam-scanning method can be used in reflection set up, where both excitation and reflected beams are scanned by x and y scanning mirrors. This ensures that the excitation spot is always focused on the detector pinhole. When stage scanning is used, the beams remain stationary with respect to the optics, which means that objective aberrations do not influence the resulting image and good images can be recorded even when using cheaper optics. Scanning the stage also makes optics alignment much easier, if the transmitted light is detected.

The resolution of the image depends on the size of the excitation light spot in the object focal plane of the objective, as well as the size of the detector pinhole [41]. The parameter describing resolution of a microscope objective is *numerical aperture*

$$N.A. = n \sin \Theta, \quad (3.3)$$

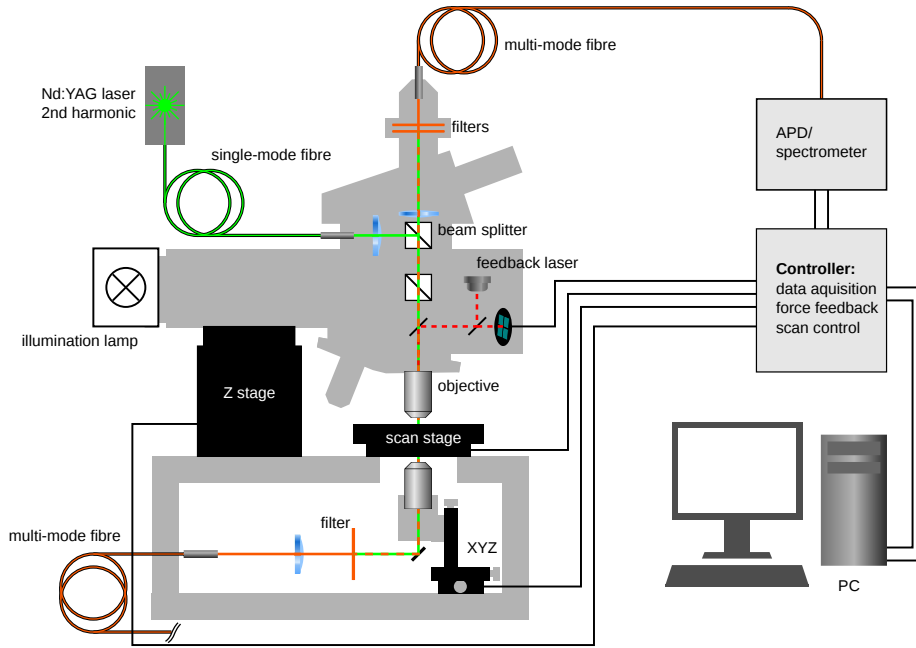
where n is the refractive index of the medium between the objective and the sample and Θ is the angle under which the light from the sample is collected by the objective lens. Since the refractive index of air is $n = 1$, the numerical aperture of an objective working in air is always smaller than 1. Higher resolution can be achieved with oil immersion objectives with $N.A.$ reaching 1.4. According to the Rayleigh criterion, the diffraction limited resolution at optimal conditions is [42]

$$\Delta = 0.61 \frac{\lambda}{N.A.}, \quad (3.4)$$

where λ is the light wavelength.

Fluorescence images were recorded using the α -SNOM (WITec GmbH, Germany) microscope [43]. The layout of the microscope is shown in figure 3.3. The instrument has a versatile design allowing various applications. It can be used for scanning confocal microscopy, atomic force microscopy (AFM), or scanning near-field optical microscopy (SNOM) using a special silicon cantilever with an aluminium coated pyramidal tip [44] on its end. In the SNOM mode, a sub-wavelength sized aperture in the aluminium coating on the tip apex serves as a point-like near-field source. In the confocal microscopy mode, the microscope can be operated in the reflection or transmission mode. For imaging of single molecule fluorescence, the confocal microscopy in reflection was found to be the most convenient arrangement.

A compact continuous Nd:YAG laser is used as an excitation source for SNOM and confocal microscopy. The maximal available output power is 100 mW at 532 nm (second harmonic). The excitation intensity is regulated manually by a shutter driven by a micrometer screw. The excitation light is delivered to the microscope body by a single-mode polarisation-preserving optical fibre. The light is collimated in the microscope body and focused onto a sample by the infinity corrected microscope objective. In the reflection set up, fluorescence

Figure 3.3: Layout of the α -SNOM microscope

together with the reflected excitation light is collected by the same objective. The reflected light is filtered out by a bandpass filter and fluorescence is focused into a multi-mode fibre which delivers fluorescence to a detector. The sample is placed on a high-precision, piezoelectrically driven scanning stage. A two-dimensional image is acquired by scanning the stage line by line and plotting a signal from the detector. The cores of the single-mode and multi-mode fibres serve as the pinholes for confocal microscopy.

For imaging purposes, the light collected from the sample is coupled through the multi-mode fibre to a SPCM-AQR (Perkin-Elmer) avalanche photodiode (APD) module with over 65% photon detection efficiency at 650 nm. The module gives a standard pulsed output (TTL) synchronised with detection events. Alternatively, the multi-mode fibre can be connected to a spectrograph. An Acton SP2300i (Princeton Instruments) monochromator with 300 mm focal length is used. It has a triple turret with 150, 600 and 1200 g/mm gratings mounted, so the monochromator dispersion can be chosen depending on the application and the required spectral resolution. The monochromator has two detector ports. One is equipped with a DV401A-BV (Andor) back-illuminated CCD camera allowing the spectrum of the collected light to be recorded. The second port is equipped with an additional APD module for imaging at a single wavelength (e.g., when performing Raman microscopy).

3.2 Data analysis

3.2.1 Fluorescence decay reconvolution

Pulse techniques, such as TCSPC described in section 3.1.2, are used to measure fluorescence kinetics of a sample, i.e., the response of the sample to an infinitely short excitation pulse, so-called δ -function. For example, in the case of mono-exponential fluorescence decay, the fluorescence response to the δ -pulse at $t = 0$ is

$$I(t) = \begin{cases} 0 & \text{for } t < 0, \\ I_0 e^{-t/\tau} & \text{for } t \geq 0. \end{cases}$$

However, due to the limited response speed of the detection system and non-zero duration of the excitation light pulses, the influence of the instrument on recorded data cannot be neglected.

Under linear conditions (i.e., the sample is far below saturation), the recorded decay $Y(t)$ is given by the convolution of the fluorescence kinetics $I(t)$ and the *instrument response function* $P(t)$,

$$Y(t) = P \otimes I = \int_{-\infty}^{+\infty} P(t - \tau) I(\tau) d\tau = I \otimes P,$$

where P itself is given by the convolution of the excitation pulse shape $E(t)$ and the response of the detection system $D(t)$,

$$P(t) = D \otimes E.$$

In order to recover fluorescence decay free of instrumental influence, reconvolution of recorded decay data with instrument response function is used [39]. The instrument response function (also called the *prompt*), is usually recorded under the same conditions as the fluorescence decay, with the sample replaced by a light scatter. Using a scatter for recording the prompt causes that the prompt is recorded at different wavelength than the fluorescence decay. However, the wavelength dependency of the detector response is often negligible.

The fluorescence decay is not recorded as a continuous function $Y(t)$ of time, but as a number of counts in discrete time intervals - channels, $Y(i)$. The convolution of two discrete functions must be used instead of integral.

In the process of reconvolution, a proper theoretical model function $I(t)$ for the fluorescence decay is chosen, for example the single- or multi-exponential model, or the function given by 2.24 or 2.19. This function is then convoluted with the recorded prompt, which yields fit data points,

$$F(i) = \sum_{n=-\infty}^{+\infty} P(i - n) I(n).$$

These fit points are then compared to recorded data points $Y(i)$ by the *least squares method*. Parameters of the fluorescence model functions are optimized by iteration to minimize the sum of weighted residuals

$$\chi^2 = \sum_{i=1}^N \left[\frac{Y(i) - F(i)}{\sigma(i)} \right]^2 \quad (3.5)$$

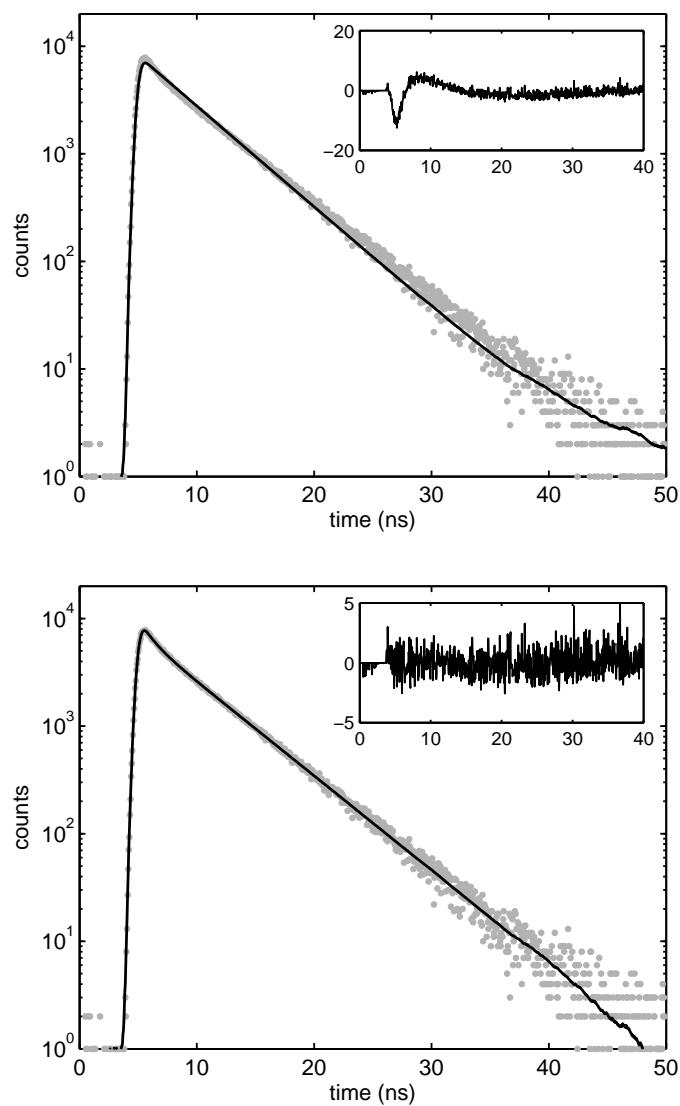


Figure 3.4: **Top:** An example of a bad fit - synthetic data generated with a two-decay-time kinetic model (grey dots) fitted by the mono-exponential function (black solid line). Residuals plotted in the inserted box are clearly correlated. **Bottom:** A good fit - the same data fitted with the two-exponential function.

where $\sigma(i)$ is the expected standard deviation. For the Poisson distributed noise, $\sigma(i) = \sqrt{I(i)} \approx \sqrt{Y(i)}$. For a good fit, $\chi^2 \approx N - \nu$, where N is the number of channels and ν is the number of fit parameters. In practice, the normalized $\chi_N^2 = \frac{\chi^2}{N-\nu}$ value is used, which should be close to 1 for a good fit. The goodness of the fit should be further verified by inspecting the weighted residuals

$$R(i) = \frac{Y(i) - F(i)}{\sigma(i)},$$

which should be randomly distributed around zero, showing no correlation (see the example in figure 3.4).

3.2.2 Fitting of electronic spectra

It is often desired to reduce a large set of data representing a fluorescence or absorption spectral band of a studied dye to a few parameters describing the bands positions and shape. Smooth electronic spectra of complex organic molecules can be often well described by the analytical four-parameter *log-normal function* defined as [45–50]

$$I_{LN}(\lambda) = \begin{cases} I_{max} \exp \left[-\frac{\ln 2}{\ln^2 \rho} \ln \frac{\alpha - \lambda}{\alpha - \lambda_{max}} \right] & \text{for } \lambda < \alpha, \\ 0 & \text{for } \lambda \geq \alpha, \end{cases} \quad (3.6)$$

where $\rho = \frac{\lambda_{max} - \lambda_-}{\lambda_+ - \lambda_{max}}$ is the asymmetry parameter, $\alpha = \lambda_{max} + \frac{w\rho}{\rho^2 - 1}$ is the function limiting point, and $w = \lambda_+ - \lambda_-$ is the bandwidth. It is obvious that $I_{max} = I(\lambda_{max})$ and $I(\lambda_-) = I(\lambda_+) = I_{max} \exp[-\ln 2] = \frac{I_{max}}{2}$. The log-normal function is limiting to Gaussian function for $\rho \rightarrow 1$,

$$I_G(\lambda) = I_{max} \exp \left[-4 \ln 2 \frac{(\lambda - \lambda_{max})^2}{w^2} \right]$$

In the fitting procedure, recorded spectrum points are compared to the log-normal function by the method of least squares, similarly to the fitting method described in the previous section. Optimal parameters λ_{max} , I_{max} , w and ρ are found, minimizing the difference between the analytical and recorded data points. As it is demonstrated in figure 3.5 on the example of badan dissolved in two different solvents, the log-normal function sometimes fits excellently the recorded spectrum and sometimes not so well - especially when the vibrational structure of the band is significantly manifested. In some cases, a suitable choice of data weights can ensure better affinity of the fitted function in the region of interest.

A custom written script was used for fitting electronic spectra by Matlab R2009b (Mathworks) software.

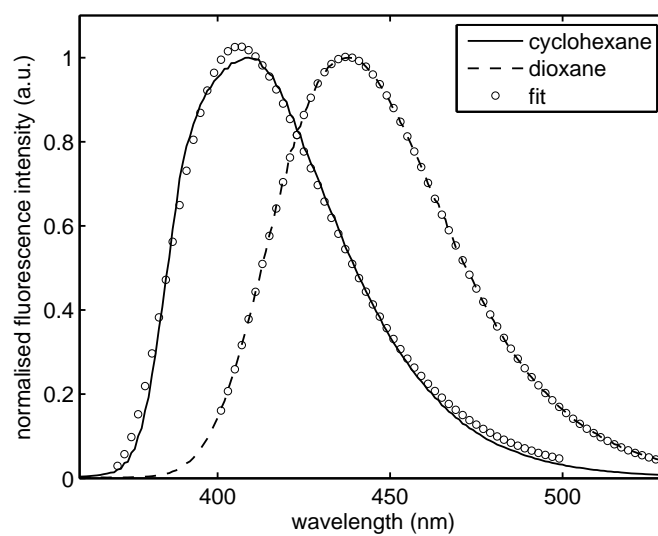


Figure 3.5: Comparison of fitted functions of badan dissolved in cyclohexane and dioxane

Chapter 4

Host matrix studies

The sol-gel process is a wet-chemical technique in which a liquid solution (colloidal **sol**) is gradually evolving towards a **gel** – network containing both liquid and interconnected solid particles [51]. Various sol-gel protocols are used for preparation of monolithic glasses, ceramics, anorganic membranes, protective thin-film coatings, and other materials. Precursors in the sol-gel process consist of metal or metalloid element surrounded by various ligands. Typical examples are semi-metal alkoxides tetramethyl orthosilicate (TMOS) and tetraethyl orthosilicate (TEOS) that are both widely used in sol-gel research. They undergo hydrolysis and polycondensation reactions to form a sol – a colloidal suspension of solid particles in a liquid. Particle sizes are typically 1 – 1000 nm, i.e., they are small enough to exhibit Brownian motion. As the sol evolves, particles can eventually aggregate and form three-dimensional microporous network. An example of gel formation from TMOS as a precursor is depicted in figure 4.11 (section 4.2, page 46).

Water-filled inorganic silica matrices prepared by the sol-gel method provide an excellent host material for fluorophore immobilisation. They are of particular importance for single biomolecule studies and fluorescence-based sensing using analyte-sensitive biomolecules [52]. Fluorescent macromolecules (such as the fluorophore-labelled protein described in chapter 5) are entrapped in the microporous matrix whereas smaller analyte molecules may diffuse through the structure and interact.

Both physical and chemical properties of the resulting gel can be tailored through a variety of parameters of sol-gel processing, such as the sol composition, temperature, pH, etc. Despite the numerous studies focused on the synthesis of silica matrices by the sol-gel method, there are still some points open to questions. In order to be able to optimise properties of the final product for an intended application, it is of great importance to develop reliable methods to control each stage of polymerisation. It has been shown that fluorescent molecular probes can be used to monitor the sol-gel process *in situ* without interfering in its natural course [53–59]. Application of fluorescent probes in investigation of inorganic silica matrix properties on the microscopic scale is the general subject of this chapter. Due to the variety of phenomena discussed here, each section is provided with a more specific introduction.

4.1 Interaction of Rhodamine 6G and colloidal silica

4.1.1 Introduction

It has been shown that fluorescence spectroscopy techniques can be used for nanoparticle size measurement in colloidal solution [53–56]. When a fluorescent dye is attached to a spherical particle, the recorded fluorescence depolarization reports on Brownian rotation of the particle. The rotational correlation time obtained by the time-resolved anisotropy measurement can be used to calculate the size of the nanoparticle through relationship 2.27, page 13. Using this technique, particle sizes of $\sim 1 - 10$ nm can be measured with several advantages compared to other conventional methods such as small angle X-ray scattering, small angle neutron scattering, transmission electron microscopy and light scattering.

This section presents studies of the interaction between Rhodamine 6G (Rh6G) and silica nanoparticles in colloidal solution Ludox (W. R. Grace & Co.). The topic is related to experiments carried out previously in the Photophysics group in order to establish fluorescence depolarisation measurements as a standard nanometrology technique to measure size of spherical nanoparticles [53]. Due to electrostatic attraction, a cationic Rh6G fluorophore is non-covalently bound to a negatively charged surface of a silica nanoparticle. The fluorophore is participating in the particle's rotation, thus the decay of the fluorescence anisotropy reports on the speed of rotation and therefore the size of the particle. However, if the probability of occurrence of more than one fluorophore bound to a single particle is increased, energy transfer from one fluorophore to another can happen. This process, known as donor-donor energy migration (DDEM), contributes to the fluorescence depolarisation. Because the probability of energy transfer depends strongly on the distance between the two fluorophores, analysis of the fluorescence anisotropy decay can, in principle, be used to extract information on the particle size. The development of particle size measurement method utilising analysis of fluorescence depolarisation measurements in terms of DDEM would expand the variety of available fluorescence spectroscopy technique in nanometrology. The primary aim of experiments presented in this section was to examine Rh6G/Ludox solutions as a reference system to study DDEM on the surface of well defined spherical particles. Preliminary experiments indeed showed decrease of fluorescence anisotropy with increasing number of fluorophores per particle. However, more detailed study, that is to be presented here, leads to a conclusion that the anisotropy decrease is governed by formation of dye aggregates, rather than DDEM.

Ludox

Ludox® is a registered trademark currently owned by W. R. Grace & Co., who acquired Ludox colloidal silica business from E. I. du Pont de Nemours & Co. in 2000. Colloidal silica is used in a wide range of applications in material research and industry. For example, it is often used as an additive for modifying surface properties of solid materials. Ludox is a stabilised aqueous dispersion of silicon dioxide particles with a well defined spherical shape and uniform size. Although negatively charged particles in Ludox repel each other,

	SM30	AM30	AS40
stabilising counter ion	Sodium	Sodium	Ammonium
particle charge	Negative	Negative	Negative
aver. particle diameter (nm)	7	12	22
specific surface area (m^2g^{-1})	345	230	135
silica (as SiO_2), (wt%)	30	30	40
pH (at 25° C)	10.2	8.9	9.1
titratable alkali, (wt%)	0.58 (Na_2O)	0.24 (Na_2O)	0.16 (NH_3), 0.08 (Na_2O)
$\text{SiO}_2/\text{Na}_2\text{O}$ (by wt)	52	125	255
chlorides (as NaCl), (wt%)	0.010	0.007	0.002
sulfates (as Na_2SO_4), (wt%)	0.030	0.006	0.005
density (25° C) (g mL^{-1})	1.22	1.21	1.30
concentration (mol L^{-1})	1.35×10^{-3}	2.81×10^{-4}	6.63×10^{-5}

Table 4.1: Ludox properties

when the colloid is exposed to atmosphere for a sufficiently long time, silica particles start to fuse together into clusters and eventually form a gel. There are several Ludox products available with different composition and particle size. Colloids used in this thesis, Ludox AS40, AM30, and SM30, have particle diameter 22, 12, and 7 nm, respectively. Properties of these colloidal solutions are listed in table 4.1. All, except the silica particle concentration, are taken from the data sheets [60]. The manufacturer does not provide any data on heterogeneity in the particle size distribution. Scanning electron microscopy measurements on dried AS40 confirmed a relatively narrow size distribution with a standard deviation of 2.5 nm [53]. However, there might be batch-to-batch variations of the average particle size [53].

The molar concentration of silica particles in Ludox colloidal solution was estimated from the specifications given by manufacturer in [60]. The number of particles in a certain volume of the colloid can be calculated by dividing the mass of silica in this volume by the mass of one nano-particle (spherical shape is assumed). The resulting formula for molar concentration of silica nanoparticle is then

$$[\text{NP}] = \frac{pd_{\text{colloid}}}{d_{\text{silica}}4/3\pi R^3 N_A},$$

where p is weight percentage of silica in the colloid, d_{colloid} is the total density of the colloid, d_{silica} is the silica density, R is the particle radius, and $N_A = 6.022 \times 10^{23} \text{ mol}^{-1}$ is the Avogadro constant.¹ The density of silica in the colloid, can be estimated using

$$d_{\text{silica}} = p \times \left(\frac{1}{d_{\text{colloid}}} - \frac{1-p}{d_{\text{water}}} \right)^{-1},$$

when assuming that the content of substances other than water and silica can be neglected. Then

$$[\text{NP}] = \frac{1}{4/3\pi R^3 N_A} \left(1 - \frac{d_{\text{colloid}}}{d_{\text{water}}}(1-p) \right) \quad (4.1)$$

¹Avogadro's number is the number of "elementary entities", usually atoms, molecules or particles, in one mole.

	nominal	bias	$\Delta[\text{NP}]/[\text{NP}]$
R	11 nm	1 nm (9.1%)	-0.230
d_{colloid}	1.295 g/mL	0.05 g/mL (3.9%)	-0.135
p	0.40	0.05 (12.5%)	0.290

Table 4.2: Error of the estimation of the silica particle concentration. Example of AS40

Ludox	m_1 (g)	m_2 (g)	%	p
SM30	5.3740	1.7345	32.3	0.3
AM30	6.4621	1.9801	30.6	0.3
AS40	7.5158	3.1489	41.9	0.4

Table 4.3: Measurement of silica content in Ludox: the weight of the sample before (m_1) and after (m_2) water evaporation, the percentage of m_2/m_1 and the silica content p as stated by the manufacturer

It may be useful to show how large is the error of the silica nanoparticle concentration estimated using the equation 4.1. Since the data sheets do not provide any precision of the experimentally measured parameters, the formula for error propagation can not be applied. Instead, we can try to vary parameters by certain amounts and see what effect this would have on the resulting concentration value. This is a form of sensitivity analysis, that can give insight, what the systematic error can be. When the value of variable x is biased by $\Delta x \ll x$, the relative change in the value of function $f(x)$ is $f(x + \Delta x)/f(x)$. Thus

$$\frac{\Delta[\text{NP}]}{[\text{NP}]} = \frac{[\text{NP}](R + \Delta R, d_{\text{colloid}} + \Delta d_{\text{colloid}}, p + \Delta p) - [\text{NP}](R, d_{\text{colloid}}, p)}{[\text{NP}](R, d_{\text{colloid}}, p)}.$$

This means, that if, for example, the real proportion of silica in AS40 would be overestimated by 0.05 (which is approx 13%), the resulting value would be overestimated by 30%. From the values in the last column in table 4.2, one can conclude that there can be a large error in the particle concentration calculated using 4.1. As was already noticed, the actual variations of nominal values of R , d_{colloid} and p are not known, so the bias values in table 4.2 are based on a mere guess. They are, however, quite realistic. For example, the actual content p of silica in colloidal Ludox can be checked simply by weighting a Ludox sample before and after liquid phase evaporation. The result of such experiment is shown in table 4.3. Samples were left in oven for 24 hours at $\sim 60^\circ \text{C}$. After that samples gelled and cracked. The silica content in Ludox is the ratio of the dry sample to the wet sample weight, m_2/m_1 . As can be seen, the actual value of p may differ by few percent from the nominal value.

Rhodamine 6G

Rhodamine 6G (Rh6G) is a water soluble fluorescent dye from the xanthene family of dyes. It is a cationic dye which makes it suitable for non-covalent labelling of Ludox silica particles with negatively charged surface. Rh6G has absorption maximum at 529 nm with molar absorption coefficient $116,000 \text{ M}^{-1}\text{cm}^{-1}$, the

emission band has maximum at 550 nm (measured in ethanol), and quantum yield 0.95 in ethanol and 0.9 in water [61]). The fluorescence decay of Rh6G is mono-exponential with ≈ 4 ns lifetime. Rh6G is often used as a laser dye, thanks to its high photostability and the fact that it can be excited by the second harmonic of a Nd:YAG laser (at 532 nm) – one of the most common solid-state lasers. Another advantage of using Rh6G as a probe in colloidal silicas is its chemical stability over a wide range of pH.

4.1.2 Experimental results

Ludox colloidal solutions as well as Rhodamine 6G chloride were purchased from Sigma-Aldrich and used without further purification. Several sample preparation procedures were tested, such as successive addition of silica or the dye, mixing two separate solutions of the dye and Ludox, etc. It can be concluded that the photophysical properties of resulting sample were quite independent of the way the additives were mixed. In most experiments presented here, a sample of Rh6G dissolved in distilled water was prepared from a stock solution with a known concentration. The dye concentration was verified by absorbance measurement. Silica was then added to the sample, either directly or from a diluted solution, by a volumetric pipette, typically by $\sim 10 \mu\text{L}$ volume. The dilution effect of the addition on the particle and dye concentrations was accounted for in calculations, although it was quite small.

Let \bar{N} be the ratio of the dye concentration and the particle concentration, $\bar{N} = [\text{Rh6G}]/[\text{NP}]$. At higher dye concentrations, particles occur with different numbers of dye molecules attached to their surface. It is reasonable to suppose that the population of particles labelled by a given number of fluorophores follows Poisson distribution with \bar{N} as the mean number of fluorophores per particle.

Absorption spectra

Colloidal silica is a scattering medium. In fact, it is an advantageous material for preparing light scatter for TSCPC measurements (section 3.1.2). Therefore, the background absorption was always recorded using a “blank” sample containing Ludox of the same concentration and no dye. Of all three Ludox solutions studied, AS40 (largest particle diameter) scatters light most effectively and SM30 least. The most reproducible way to record absorption was to prepare aqueous solution of Rh6G and successively increase the Ludox concentration. This, however, prevents to record background with exactly the same sample – a different blank sample had to be prepared – which reduces somewhat the precision of the measurement.

At sufficiently low dye concentration, $\bar{N} \ll 1$, the absorption spectrum of Rh6G in Ludox resembles the spectrum in aqueous solution in both position and amplitude (comparison not shown). The shape of the spectrum also overlaps with fluorescence excitation spectrum. As follows from the fluorescence anisotropy measurements (presented below), most of fluorophores are attached to silica particles at $\bar{N} \ll 1$. This means that binding has no effect on absorption spectrum. However, when the ratio of dye concentration is increased, the absorption spectrum is distorted. A second peak around 500 nm appears, which

is an indication of dye aggregation (see the discussion in 4.1.3). The peak at 500 nm is more pronounced with higher \bar{N} . Moreover, at similar values of \bar{N} , the aggregation is stronger when the particle radius is smaller, i.e., it is most noticeable with SM30.

Figure 4.1 shows the absorption spectra of Rh6G in Ludox solution recorded at different nanoparticle concentrations. At a certain concentration range, it appears that spectra intersect at a single wavelength, 508.00 ± 1.35 nm - an *isosbestic point* (figure 4.1, top). The presence of the isosbestic point indicates that strictly two species are present in the solution - in this case monomers and dimers of Rh6G. The values of the molar absorption coefficient of monomer and dimer are equal at the isosbestic point. At higher \bar{N} , absorption spectra do not cross at a single point (figure 4.1, bottom), probably due to formation of higher aggregates (trimers, tetrameres, etc.).

As was mentioned above, samples for absorption measurements were prepared from a solution of Rh6G in water (zero nanoparticle concentration) by gradual increase of the silica nanoparticle concentration between each scan by addition of $\sim 10^{-5}$ L of Ludox solution with a known silica concentration. The dye concentration is best estimated from the absorption spectrum of the sample in absence of silica and known extinction coefficient of Rh6G in water. When the silica concentration is increased, some dimers dissociate to monomers which results in increase of absorbance at 529 nm (monomer peak absorption) and decrease at 500 nm (dimer peak). The change of the spectral shape was instantaneous with respect to the measurement speed (the entire scan of the absorption spectrum takes ~ 2 minutes).

Fluorescence

The fluorescence emission of Rh6G in Ludox at $\bar{N} \ll 1$ is shifted to shorter wavelengths by ≈ 4 nm with respect to the emission band of Rh6G in neat water (figure 4.2). A bathochromic shift towards the emission in water was observed, when \bar{N} was increased. A significant decrease of fluorescence intensity with increasing \bar{N} was observed. This decrease was reversible in a sense that by adding more silica to the sample (i.e. by allowing more surface to form monomers) the intensity increased.

The overlap between Rh6G absorption and emission spectra gives an opportunity for energy transfer to occur between fluorophores located on a surface of one nanoparticle. This might lead to depolarisation of fluorescence by donor-donor energy migration. It is instructive to compare the particle sizes listed in table 4.1 with Förster radius (see section 2.2.3) which gives the distance of 50% probability for non-radiative energy transfer. An overlap integral (for discrete data points a summation) was calculated from measured absorption and fluorescence emission spectra according to

$$J = \frac{\sum_i I(\lambda_i) \epsilon(\lambda_i) \lambda_i^4}{\sum_j I(\lambda_j)},$$

where $I(\lambda_i)$ is the recorded fluorescence intensity at wavelength λ_i , and $\epsilon(\lambda_i)$ is the extinction coefficient at λ_i . The Förster radius is then

$$R_0 = 9.78 \times 10^3 \sqrt{\kappa^2 n^{-4} \Phi_D J} \text{ (\AA)}$$

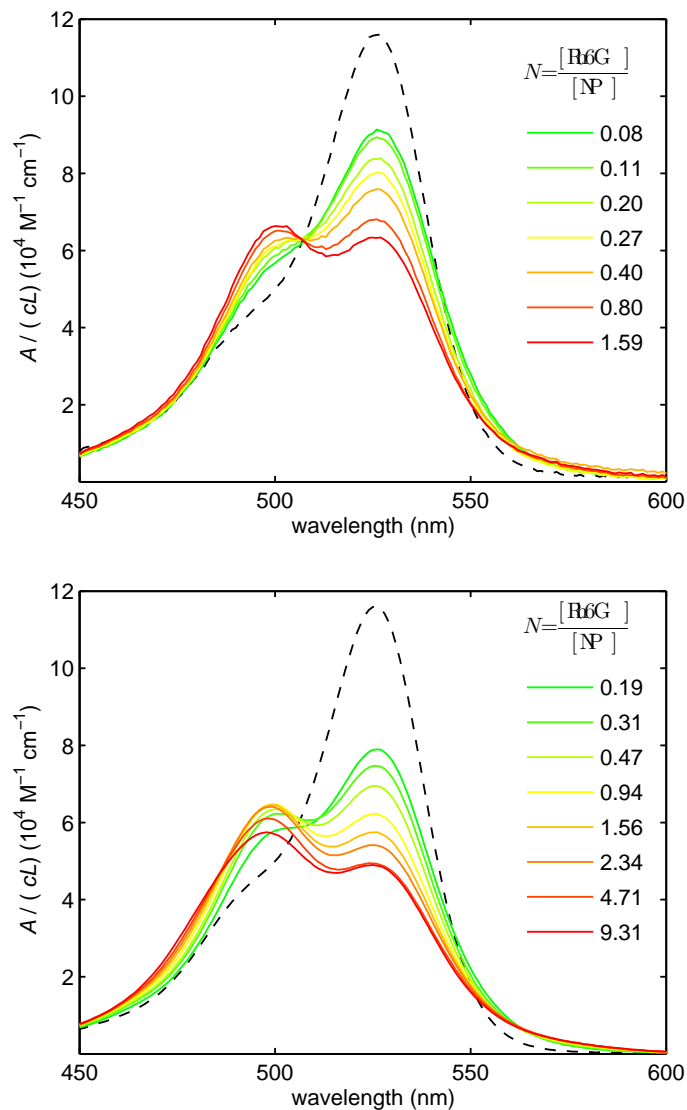


Figure 4.1: Absorption spectra of Rh6G in diluted Ludox SM30. The ratios of the dye and nanoparticle concentrations were \bar{N} ($[\text{Rh6G}]:[\text{NP}]$ in μM) = 0.08 (0.70:8.78), 0.11 (0.70:6.16), 0.20 (0.71:3.55), 0.27 (0.71:2.67), 0.40 (0.71:1.79), 0.80 (0.72:0.90), 1.59 (0.72:0.44) (**top**), and 0.19 (2.82:15.00), 0.31 (2.95:9.42), 0.47 (3.02:6.43), 0.94 (3.10:3.29), 1.56 (3.13:2.00), 2.34 (3.14:1.34), 4.71 (3.16:0.67), 9.31 (3.17:0.34) (**bottom**). The dashed lines represent absorption spectra of Rh6G in water.

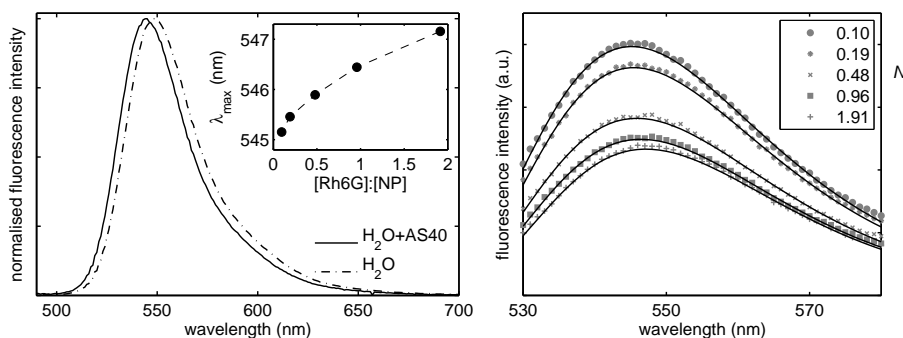


Figure 4.2: **Left:** The comparison of the normalised fluorescence emission spectra of Rh6G in water and in diluted Ludox AS40. The inserted graph shows the dependency of the wavelength λ_{max} of the fluorescence emission maximum on the ratio of the dye and particle concentrations (recorded with SM30). **Right:** Fluorescence emission spectra of Rh6G in diluted Ludox SM30 recorded at different particle concentrations. Fitted spectra are represented by solid lines.

where $\kappa^2 = 2/3$ is the orientation factor, $n = 1.34$ refractive index of water, and $\Phi_D = 0.9$ is the quantum yield of Rhodamine 6G in water. The resulting values of Förster radius for donor-donor energy transfer are $R_0 = 53 \text{ \AA}$ for Rh6G in water and $R_0 = 56 \text{ \AA}$ for spectra of $1.4 \times 10^{-7} \text{ M}$ Rh6G in diluted AS40, $[\text{NP}] = 1.9 \times 10^{-6} \text{ M}$, $\bar{N} = 0.07$.

Fluorescence decays were recorded using a laser diode emitting at 405 nm as excitation source. A polariser at *magic angle* (54.7°) was inserted in the detection path. Fluorescence lifetime of Rh6G in colloidal Ludox at $\bar{N} \ll 1$ is the same as lifetime recorded in neat water. The rate of fluorescence decay is very similar even at higher \bar{N} , however, a second lifetime component must be included to obtain a good fit. The minor change of fluorescence lifetime does not correspond to the extent of fluorescence steady state intensity decrease. As was described in section 2.2.2, this is an indication of static quenching.

A dependence of fluorescence anisotropy on \bar{N} was studied. For each value of \bar{N} , steady-state fluorescence spectra of Rh6G in Ludox solutions were recorded with parallel and crossed excitation and emission polarisers. Fluorescence anisotropy spectra were then calculated according to equation 3.2. An example of recorded steady-state fluorescence anisotropy spectrum is shown in figure 4.3. While the emission anisotropy is constant across the fluorescence band, the excitation anisotropy is slightly lower at shorter excitation wavelengths.

Fluorescence anisotropy measurements as well as fitted fluorescence decay parameters are summarised in table 4.6 on page 44. The anisotropy values were calculated by averaging the anisotropy spectra over the emission band (530 – 580 nm). The standard deviation from the mean value is expressed as the precision of the anisotropy measurement in the table.

Plots constructed from fluorescence anisotropy data in table 4.6 are shown in figure 4.4. Steady-state anisotropy decreases monotonically with increasing \bar{N} for all Ludox types. Error bars in both plots represent the standard deviation

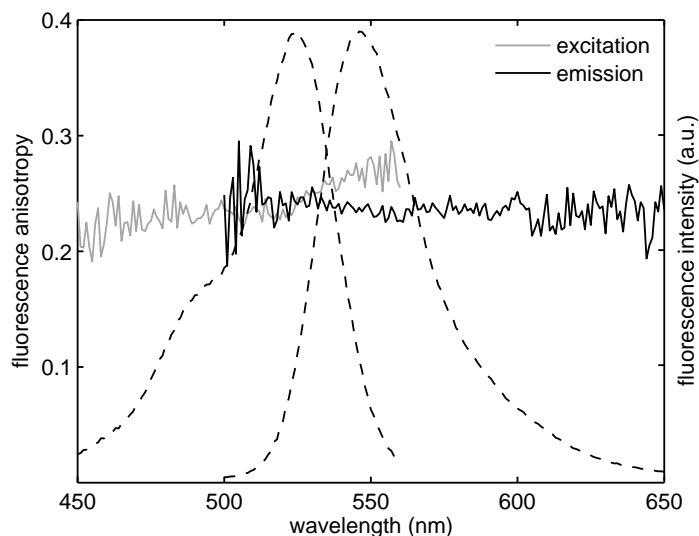


Figure 4.3: Fluorescence excitation and emission anisotropy spectrum of Rh6G in diluted Ludox SM30, dye concentration $0.3 \mu\text{M}$, nanoparticle concentration $1.4 \mu\text{M}$, $\bar{N} = 0.21$. Fluorescence excitation and emission intensity is also shown (dashed). Excitation wavelength for the emission scan was 490 nm, emission wavelength for the excitation scan was 570 nm.

from the mean value.

Figure 4.5 shows fluorescence anisotropy decays of Rh6G in a solution of AS40. For comparison, the anisotropy decay of Rh6G in neat water is also shown. The measured rotational correlation time of Rhodamine 6G in water is 190 ps which is in quite good agreement with previously reported values measured by various techniques (180 ps [62], 150 ps [63] and 210 ps [64]). Two components can be clearly recognised from the recorded anisotropy decay of Rh6G in AS40 solution. The fast component is of the same order as the correlation time of unbound Rh6G. The longer component, on the other hand, is much longer than the fluorescence lifetime. Therefore, the fluorescence anisotropy appears to be constant after $\gtrsim 2$ ns – it reaches “plateau” value. The long component can be assigned to Rh6G molecules residing on the surface of slow rotating silica nanoparticles.

Figure 4.6 shows the comparison of fluorescence anisotropy decays of Rh6G in diluted SM30, recorded for different silica nanoparticle concentration. It appears that the short correlation time remains constant and only its relative contribution to the fluorescence depolarisation is decreasing with increasing nanoparticle concentration. Recorded fluorescence anisotropy decays were fitted by reconvolution with DAS6 software (IBH) using two-exponential anisotropy decay model,

$$r(t) = \beta_1 \exp\left(-\frac{t}{\theta_1}\right) + \beta_2 \exp\left(-\frac{t}{\theta_2}\right).$$

In order to obtain rational results of the fitting, the value of the long component

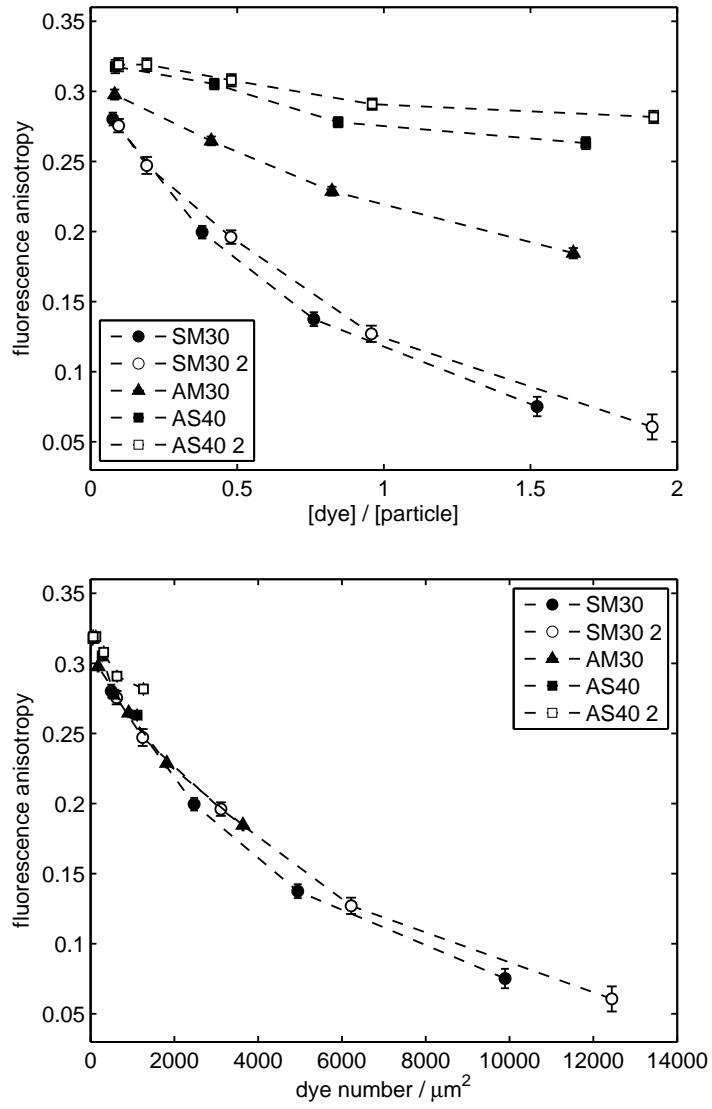


Figure 4.4: Fluorescence steady-state anisotropy as function of dye / particle (**top**) and as a function of particle per unit area (**bottom**)

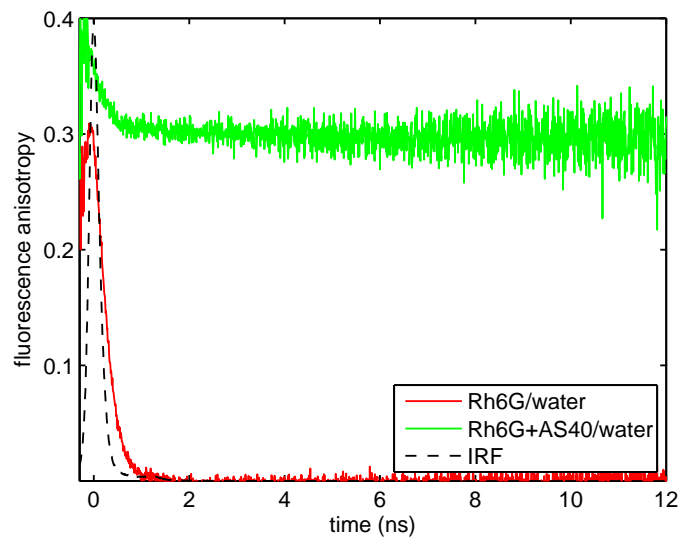


Figure 4.5: Recorded fluorescence anisotropy decay of Rh6G in water and in diluted Ludox AS40 colloidal silica solution.

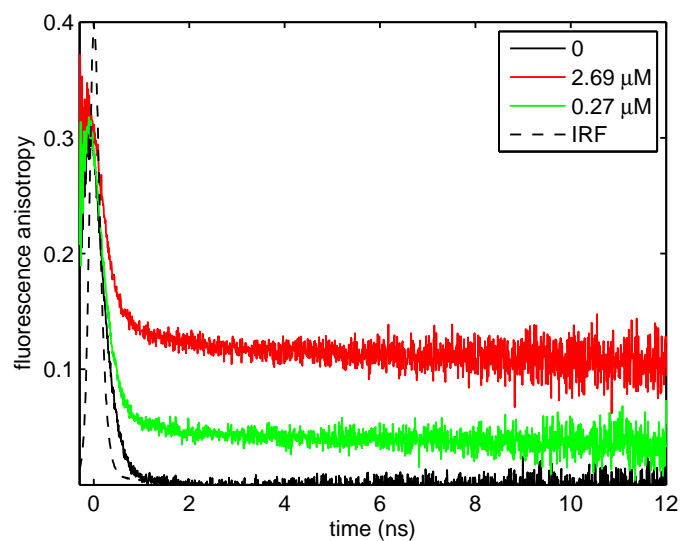


Figure 4.6: Fluorescence anisotropy of Rh6G in SM30 colloidal solution. Dye concentration $0.41 \mu\text{M}$, nanoparticle concentration 0 (black), $2.69 \mu\text{M}$ (red, $\bar{N} = 0.15$) and $0.27 \mu\text{M}$ (green, $\bar{N} = 1.52$)

[Rh6G] (μM)	[NP] (μM)	N	r_0	θ_1 (ns)	β_1	θ_2 (ns)	β_2	χ^2
0.41	0	–	0.41	0.19	0.41	-	0*	1.15
0.41	2.69	0.15	0.39	0.20	0.26	45.0*	0.13	1.20
0.41	0.27	1.52	0.40	0.19	0.35	45.0*	0.05	0.99

Table 4.4: Fitted parameter of anisotropy decay, values of parameters labelled with * were fixed; $r_0 = \beta_1 + \beta_2$.

was fixed during the fitting. A rotational correlation time can be best recovered by reconvolution of anisotropy decay recorded by TCSPC, if it is of the same order as the fluorescence lifetime value. If the correlation time is much longer than the fluorescence lifetime, the anisotropy does not decrease before most fluorophores are de-excited, i.e., the recorded anisotropy appears to be flat in the time “window” provided by fluorescence. In the other extreme, if the correlation time is too short, it simply cannot be resolved by the instrument. To reach higher precision when recording rotational correlation times of larger particles, it is advantageous to use fluorescent dyes with longer fluorescence lifetime, as was shown on measuring the size of silica particles in Ludox with 6-methoxyquinolinium dye [53]. The correlation time corresponding to the slow Brownian rotation of silica nanoparticles (with radius 3.5 nm for SM30) can be estimated by

$$\theta_2 = \frac{\eta V}{k_B T} \approx 45 \text{ ns},$$

where V is particle volume, $\eta = 1.003 \times 10^{-3}$ Pa s is the viscosity of water at 20° C (rather than bulk viscosity of the colloidal solution [53]), k_B Boltzmann constant, and $T = 293.15$ K is the sample temperature. Considering the lifetime of Rh6G, ~ 4 ns, we can not expect to reliably recover the correlation time of approx. 45 ns. By leaving this parameter free in the fitting, we might risk to obtain a rather arbitrary result. Therefore, it is more reasonable to fix θ_2 to the (however crudely) estimated value. Indeed, the effect of changing the estimate of θ_2 by ± 5 ns on the goodness of the fit was negligible.

The fitted parameters of the anisotropy fits are listed in table 4.4. As was hinted above, the shorter rotational correlation time is more or less constant and only the relative contribution of the fast component to the fluorescence depolarisation is changing with different silica concentration. The fitted values of θ_1 are remarkably similar to that recorded for Rh6G in neat water.

Figure 4.7 shows a comparison of fluorescence anisotropy decays of one sample recorded at two different temperatures, $T_1 = 1^\circ\text{C} = 274$ K and $T_2 = 25^\circ\text{C} = 298$ K. The Brownian rotation of particles depends on the sample temperature and microviscosity (equation 2.27) which is itself temperature dependent. As can be expected, the change of the temperature has a little effect on the slow anisotropy decay component corresponding to the particle rotation. The shorter component, on the other hand, is clearly faster at 298 K. The change of the shorter decay component is comparable to the change of the rotational correlation time of Rh6G in water (the decay is also shown in 4.7).

The result of the following experiment illustrates the temporal stability of samples, as well as the reproducibility of sample preparation. Two samples

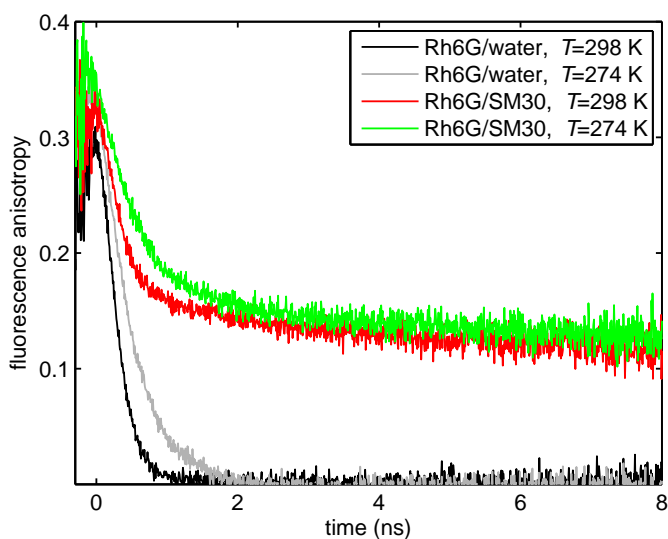


Figure 4.7: Fluorescence anisotropy decays of Rh6G in SM30 solution recorded at two different temperatures. The dye concentration was $[\text{Rh6G}] = 0.36 \mu\text{M}$ and the concentration of silica particles was $[\text{NP}] = 0.45 \mu\text{M}$, $\bar{N} = 0.80$. Anisotropy decays of Rh6G in neat water at the two temperatures are also shown.

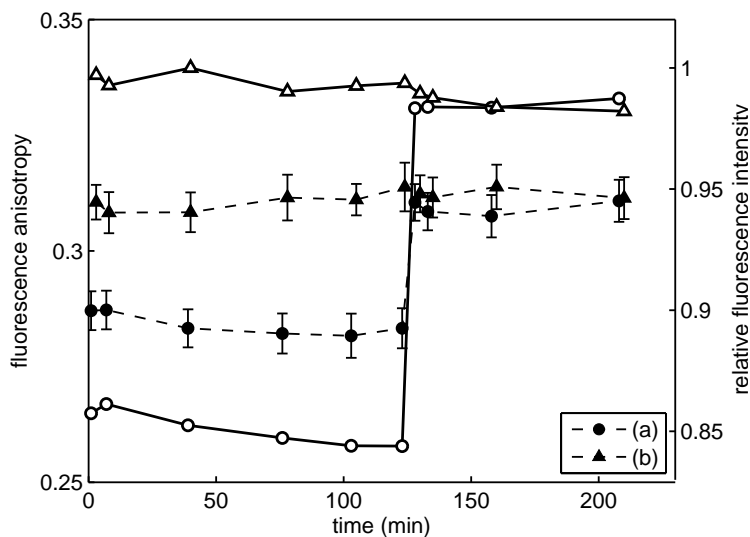


Figure 4.8: Fluorescence intensity and anisotropy dynamics following a step change of the silica nanoparticle concentration. Circles correspond to sample **a** and triangles to sample **b**. Filled markers with error bars represent anisotropy with its standard deviation, fluorescence intensity is represented by empty markers.

were prepared with the same Rh6G concentration $[\text{Rh6G}] = 0.50 \mu\text{M}$, but different concentration of Ludox AS40. Concentration of silica particles was $[\text{NP}]_{\text{a}} = 0.53 \mu\text{M}$ in sample **a** and $[\text{NP}]_{\text{b}} = 4.92 \mu\text{M}$ in sample **b**. Corresponding ratios were $\bar{N}_{\text{a}} = 0.94$ and $\bar{N}_{\text{b}} = 0.10$. Steady-state fluorescence anisotropy and intensity were then continuously monitored. As expected, both anisotropy and intensity of sample **a** (higher \bar{N}) were significantly lower. After approx. 2 hours, the concentration of silica particles in sample **a** was increased to match that of sample **b**, $[\text{NP}]_{\text{a}} = [\text{NP}]_{\text{b}} = 4.92 \mu\text{M}$, $\bar{N}_{\text{a}} = \bar{N}_{\text{b}} = 0.10$. The recorded time dependencies of steady-state fluorescence anisotropy and relative fluorescence intensity are shown in figure 4.8. Both monitored quantities matched immediately after silica was added to sample **a**. It means that the two different samples with the same final composition, however, prepared in different steps, yielded the same result. Based on this experiment, it can be stated that reproducibility of sample preparation, as well as the sample stability (sample **b** was monitored for over 3 hours without substantial change), is fairly good. Furthermore, similar to the conclusion from the absorption measurements, the new equilibrium of the sample after changing $[\text{NP}]$ is established within a few minutes.

Estimation of the free dye content

An experimental estimation of the content of the unbound dye in a sample was attempted. The higher density of silica gives the opportunity to separate the liquid phase of the colloid from the solid phase – nanoparticles – by centrifugation. The liquid phase should then contain dye of the same concentration as the liquid phase of the colloid before the centrifugation (assuming that the centrifugation itself does not alter the unbound dye concentration). Samples containing Rh6G and silica of known concentrations were left overnight at room temperature to stabilise and then centrifuged at 14 krpm (10^3 rounds per minute) for 2 hours. Two phases were clearly recognisable visually – silica at the bottom of the eppendorf test tube, judging by its hue, contained dye of higher concentration than the faint-coloured liquid phase. A sufficient part of the liquid phase could be easily removed with a pipette. The time-resolved fluorescence anisotropy measurement was performed on the removed liquid phase in order to confirm successful separation. The dye concentration in the liquid phase could be estimated by measuring its absorbance. It was found that labelled silica nanoparticles can be well precipitated by centrifugation with AS40 – the recorded fluorescence anisotropy decay of the liquid phase was identical with that of Rh6G in neat water. However, time-resolved anisotropy measurement proved that the complete separation cannot be accomplished using this method with SM30 (the colloid with the smallest particle diameter) and still a substantial amount of labelled particles was present in the seemingly “neat” phase after centrifugation. Therefore, further experiments were proceeded only with AS40.

In order to exclude unexpected effects of centrifugation a test was performed using anionic fluorescein instead of Rh6G. No indication of interaction between fluorescein and silica nanoparticles was observed and the dye concentration in the liquid phase after the procedure described above was found to be the same as in the colloid at the start of the experiment.

Six samples of Rh6G in diluted AS40 solution with different dye and nanoparticle concentrations were prepared. The composition of the samples is listed in

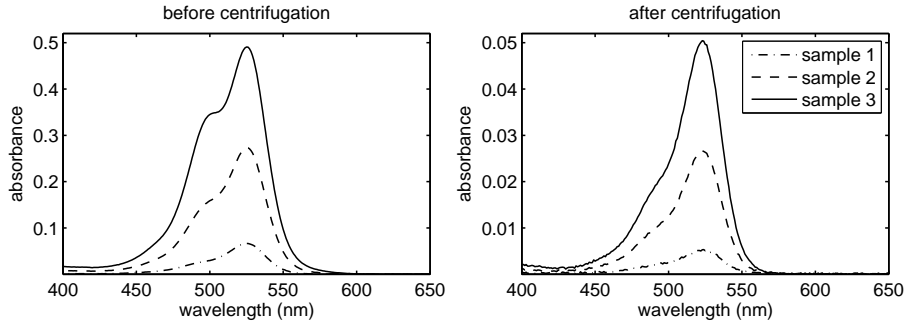


Figure 4.9: Absorption spectra of the samples before (**left**) and after (**right**) the silica particles were removed by centrifugation.

[Rh6G] (μM)	[NP] (μM)	[Rh6G]/[NP]	A_{max}	[Rh6G] _{free} (nM)	f
0.35	1.08	0.32	0.003	32	0.093
1.72	1.07	1.6	0.014	160	0.093
3.38	1.05	3.21	0.029	319	0.094
0.69	2.14	0.32	0.005	59	0.086
3.38	2.11	1.6	0.027	296	0.088
6.65	2.08	3.21	0.050	560	0.084

Table 4.5: Centrifugation data, recorded using Ludox AS40. [NP] - initial nanoparticle concentration, [Rh6G] - initial dye concentration, A_{max} - maximal absorbance of the neat phase after centrifugation, [Rh6G]_{free} - dye concentration corresponding to A_{max} , $f = [\text{Rh6G}]_{\text{free}}/[\text{Rh6G}]$ - fraction of the unbound dye.

table 4.5. The labelled silica particles were precipitated by the centrifugation procedure described above. The dye concentration in the neat solvent was then calculated from the measured absorbance. The recorded absorption spectra of samples before and after removing labelled particles are shown in figure 4.9. The absorption spectrum of the sample with highest dye concentration recorded before centrifugation clearly indicate dye aggregation. The fraction f of the free dye (also listed in table 4.5) was calculated as the ratio of the dye concentration in the separated neat solvent to the initial dye concentration in the prepared sample,

$$f = \frac{[\text{Rh6G}]_{\text{free}}}{[\text{Rh6G}]} = \frac{A_{max}}{\epsilon_{max}[\text{Rh6G}]}$$

The dye concentration in the separated neat solvent was calculated from the recorded absorbance A_{max} and the maximal molar absorption coefficient of Rh6G, $\epsilon_{max} = 116,000 \text{ M}^{-1}\text{cm}^{-1}$.

Resulting values of f listed in table 4.5 indicate that at constant concentration of silica particles, the fraction of unbound dye is independent of the absolute dye concentration. However, there might be a slight dependency on the particle concentration. The mean value of the free dye fraction is $9.33 \pm 0.06\%$ at $[\text{NP}] \approx 1 \mu\text{M}$ and $8.60 \pm 0.20\%$ at $[\text{NP}] \approx 2 \mu\text{M}$. It should be pointed out that during the centrifugation, the concentration of silica particles is extremely non-homogeneous – it is very high at the bottom of the test tube and very low in the “neat” phase – which might influence the result of the experiment. In other words, the resulting values are correct only if we can presume that the centrifugation itself does not affect the equilibrium between bound and unbound fluorophores. Nevertheless, it can be estimated that the fraction of unbound dye is $\lesssim 10\%$ of the total dye concentration in the sample.

4.1.3 Discussion

From the experimental observations, a hypothesis can be proposed. Positively charged Rh6G fluorophores reside on the surface of negatively charged silica nanoparticles and they participate in their slow Brownian rotation which leads (at sufficiently low \bar{N}) to increased fluorescence anisotropy compared to Rh6G in neat water. The size of the nanoparticles has a negligible effect on the steady-state anisotropy because for all colloidal solutions used here, the depolarisation due to particle Brownian rotation happens on much larger scale than the fluorescence decay, $\theta_2 \gg \tau$. If the number of fluorophores per particle is increased, either by increasing the dye concentration or decreasing the silica concentration, dye aggregates are formed on the surface of silica nanoparticles which is manifested by the occurrence of additional peaks in absorption spectra. The aggregate formation is best noticeable with SM30 Ludox solution which has the smallest particle diameter. Most aggregates are probably non-fluorescent, or have low quantum yield, which would explain the decrease of fluorescence intensity with increasing \bar{N} . This would lead to preferential decrease of the relative contribution from fluorophores located on the surface of nanoparticle to overall fluorescence. In that case, the more significant contribution from freely rotating fluorophores (i.e., not attached to the silica surface) would result in a lower anisotropy. In other words, the observed relationship between the steady-state fluorescence anisotropy and \bar{N} indirectly reports on the amount of

aggregation in the sample. This conjecture is further supported by the outcome of the time-resolved anisotropy measurements. The two-exponential character of the anisotropy decay does not change with changing \bar{N} , only relative contributions of the two components. Also, the temperature dependence of the shorter rotational correlation time (figure 4.7) indicates that the fast anisotropy decay component originates in fluorescence depolarisation due to fast Brownian rotation of the unbound fluorophores.

According to the proposed mechanism – preferential static quenching of the bound fluorophores – the decrease of steady state fluorescence anisotropy with \bar{N} (shown in figure 4.4 on page 35) is a result of increasing number of dye aggregates in the sample. It can be noticed that the steady-state anisotropy values plotted as a function of the specific surface of silica in the sample (the plot on bottom) follow the same trend, independently of the particle size and absolute concentrations of the dye and nanoparticles. This indicates that the surface available for a fluorophore to reside on is determining the probability of dye aggregation.

No evidence of donor-donor energy migration was observed. In the presence of DDEM as the exclusive process responsible for fluorescence depolarisation, the fluorescence kinetics, as well as the quantum yield, would remain unaltered. Though it is possible that it occurs between fluorophores located on the surface of one nanoparticle, the depolarisation of the overall fluorescence during the excited state lifetime is dominated by the contribution from the unbound fluorophores.

The tendency of rhodamine dyes to form aggregates in a solution at high concentrations is a well-known and extensively studied phenomenon [65]. Presence of Rh6G dimers can be observed in aqueous solutions at concentrations of $\sim 10^{-4}$ M at room temperature [66]. However, at $\sim 10^{-6}$ M concentration, the vast majority (> 99%) of Rh6G fluorophores exists in monomeric form [66]. Experiments presented in this section demonstrated that adding a small amount of colloidal silica into a low concentrated solution of Rh6G in water will lead to a massive dye aggregation on the surface of silica particles. If the silica particle concentration is increased, a new equilibrium is immediately established which favours more fluorophores as monomers. This indicates that the dimer formation and dissociation is quite dynamic which allows fluorophores to distribute themselves among the particles shortly after the addition. Rh6G dimers in colloidal silica are mostly non-fluorescent because their formation is associated with quenching of fluorescence.

Aggregation of xanthene-derived dyes has been observed in solvents [65–67] as well as in adsorbed state [68–70]. Rh6G, especially, is a very popular dye and there has been interest in incorporating in various host materials. From the context of this thesis, studies of aggregation of rhodamines in silica sol–gels is important [71–75]. The formation of both fluorescent and non-fluorescent dimers has been observed and conditions leading to preferential formation of either of them have been experimentally studied. Photophysical properties of a dimer are determined by the transition dipole moment of a monomer and mutual spatial arrangement of monomer units forming the dimer. The geometry of the aggregate is given by electrostatic interaction of the dye molecule with the surface and with the other monomer unit. According to single exciton theory [76], the important parameter determining the fluorescent or non-fluorescent

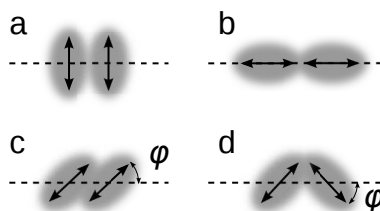


Figure 4.10: Dimer geometry: parallel – non-fluorescent (a), head-to-tail – fluorescent (b), parallel inclined (c) and oblique (d).

character of a dimer is the inclination angle φ between the dipole moments of the monomers and the line connecting their centres (figure 4.10) [68, 71, 75]. For $\varphi > 54.7^\circ$ (magic angle), the dimer is non-fluorescent and its absorption is blue shifted with respect to the monomer band. The dimer exhibits red shifted fluorescence for $\varphi < 54.7^\circ$. The fluorescent dimers are called J-dimers and non-fluorescent H-dimers². A single red shifted absorption band can be observed for J-dimers in parallel inclined or head-to-tail configuration. For oblique geometry, the band splits into two – red and blue shifted with respect to the monomer absorption. In low viscosity solvents at room temperature, only non-fluorescent H-dimers in parallel “sandwich” configuration can be observed [68, 75]. Absorption spectra of Rh6G monomer, dimer and trimer in water have been resolved by applying the law of mass action in analysis of spectra recorded at wide range of concentrations [66]. Adsorption to a surface, on the other hand, gives an opportunity for all possible arrangements to occur [68]. Formation of both H- and J-dimers has been reported for Rh6G in silica sol-gels [71, 73, 74]. Often more dimer configurations coexists in one sample.

There is no experimental evidence of presence of fluorescent J-dimers formation of Rh6G in colloidal silica. No red-shifted fluorescence band or band “shoulder” have been observed at any value of \bar{N} . Not even the recorded lifetimes of Rh6G in Ludox show sufficient change that would indicate dimer fluorescence (J-dimers have longer lifetime than monomer). The small hypsochromic shift of the fluorescence maximum, with respect to the fluorescence band in water, recorded at low \bar{N} can be identified as an effect of monomer binding to the surface of a silica particle. The red shift of emission band maximum with increasing \bar{N} “back” towards that of Rh6G in water (see figure 4.2 on page 33) only supports the increasing dominance of contribution from unbound monomer to the total fluorescence emission. The presence of the isosbestic point in absorption spectra recorded within a certain range of dye and silica concentrations indicate exclusive presence of monomers and dimers. However, formation of higher aggregates (trimers, possibly tetramers), that have spectra different from monomer and dimer, leads to disappearance of the isosbestic point at higher \bar{N} , similar to what was reported for aqueous solutions at high dye concentrations [66].

²J- named after E. E. Jelley and H- as hypsochromic.

Ludox	[NP] (μM)	[Rh6G] (μM)	N	[Rh6G]/ A (μm^{-2})	r_{SS}	I/I_{max}	τ_1 (%) (ns)	τ_2 (%) (ns)
SM30	0.27	0.52	1.91	12439	0.058 ± 0.008	0.64	0.75 (3.21)	3.83 (96.79)
	0.54	0.51	0.96	6219	0.138 ± 0.006	0.57	1.19 (4.89)	3.82 (95.11)
	1.07	0.51	0.48	3110	0.207 ± 0.007	0.71	1.07 (4.49)	3.87 (95.51)
	2.65	0.51	0.19	1244	0.249 ± 0.006	0.92	2.02 (5.8)	4.02 (94.2)
	5.19	0.50	0.10	622	0.279 ± 0.005	1.00	-	3.95 (100)
SM30	0.27	0.41	1.52	9891	0.075 ± 0.010	0.83		
	0.54	0.41	0.76	4946	0.138 ± 0.005	0.77		
	1.07	0.41	0.38	2473	0.200 ± 0.004	0.91		
	5.19	0.40	0.08	495	0.280 ± 0.005	1.00		
AM30	0.25	0.41	1.65	3638	0.185 ± 0.004	0.58	1.99 (6.38)	4.01 (93.62)
	0.50	0.41	0.82	1819	0.229 ± 0.003	0.69	2.03 (5.12)	4.04 (94.88)
	0.99	0.41	0.41	910	0.265 ± 0.003	0.84	2.06 (4.43)	4.08 (95.57)
	4.74	0.39	0.08	182	0.298 ± 0.004	1.00	2.09 (2.79)	4.09 (97.21)
AS40	0.31	0.59	1.92	1263	0.282 ± 0.004	0.73	2.01 (5.45)	4.03 (94.55)
	0.61	0.59	0.96	631	0.291 ± 0.004	0.85	2.04 (3.98)	4.04 (96.02)
	1.22	0.58	0.48	316	0.308 ± 0.004	0.93	2.06 (3.65)	4.04 (96.35)
	2.96	0.57	0.19	126	0.319 ± 0.005	0.99	-	3.99 (100)
	5.67	0.54	0.10	63	0.319 ± 0.005	1.00	-	3.99 (100)
AS40	0.24	0.41	1.69	1111	0.263 ± 0.004	0.80		
	0.48	0.41	0.84	555	0.278 ± 0.004	0.90		
	0.96	0.41	0.42	278	0.305 ± 0.004	0.97		
	4.54	0.38	0.08	56	0.318 ± 0.005	1.00		

Table 4.6: Summary of Ludox measurements

4.2 Perylene fluorescence quenched by cobalt ions in sol–gels

4.2.1 Introduction

In this section, an experimental study of interaction of a fluorescent dye perylene and cobalt ions, Co^{2+} , in silica sol–gels is presented. This topic continues a previous study conducted in the Photophysics group. Salthammer *et. al.* [77] investigated quenching of perylene by $[\text{Co}(\text{H}_2\text{O})_6]^{2+}$ in liquid solutions of different viscosity. They showed that in a high-viscosity solvent (glycerol), the quenching mechanism can be identified as energy transfer from perylene to cobalt by long-range dipole-dipole interaction (Förster resonance energy transfer - FRET), while in a mid- and low-viscosity solvent (ethylene glycol and methanol), the quenching is probably collisional, via short-range exchange (Dexter) interaction. Therefore, under certain conditions, perylene and Co^{2+} can form a FRET donor–acceptor pair [78–80].

My former colleague Gillian Macnaught discussed in her thesis [26] both theoretical and experimental aspects of donor–acceptor distance distribution from fluorescence decays – a concept called *fluorescence nanotomography* [81, 82]. As one part of her thesis, she tested the possibility of using perylene and Co^{2+} as a FRET pair to characterise the structure of a TMOS-derived sol–gel. FRET is very sensitive to the distance between the donor and the acceptor – the rate of the transfer is proportional to R^{-6} , see section 2.2.3. The main idea of fluorescence nanotomography is to utilise the great sensitivity of resonance energy transfer to recover the donor–acceptor distance distribution in the host material of interest by analysing a single fluorescence decay using the *maximum entropy method*.

Macnaught studied the temporal development of fluorescence decays of perylene in sol–gels containing $[\text{Co}(\text{H}_2\text{O})_6]^{2+}$. She observed a shortening of perylene fluorescence lifetime with polymerisation time and applied different kinetic models to analyse the recorded decays in order to comparatively find the best explanation for the observed effect. The best fits were achieved when using a decay model with resonance energy transfer (equation 2.24) accounting for the presence of collisional quenching by adding a single-exponential decay component. Based on this model, Macnaught concluded that until the gel point, collisional quenching is dominant and the dominance decreases due to the increasing viscosity. On the other hand, the influence of FRET is becoming more dominant up to the gel point.

Although the recovery of the donor–acceptor distance from fluorescence decays by the intended method is (at least) complicated by the presence of diffusion controlled quenching, the effect of perylene fluorescence lifetime shortening is related to the change of the sol–gel structure during polymerisation, and the fluorescence decay analysis might give valuable information about micro-environment in complicated porous medium. The primary aim of this section was to reproduce and extend Macnaught’s spectroscopic experiments with perylene and $[\text{Co}(\text{H}_2\text{O})_6]^{2+}$ in sol–gels and to propose an alternative kinetic model and possible interpretation of recorded fluorescence and absorption data.

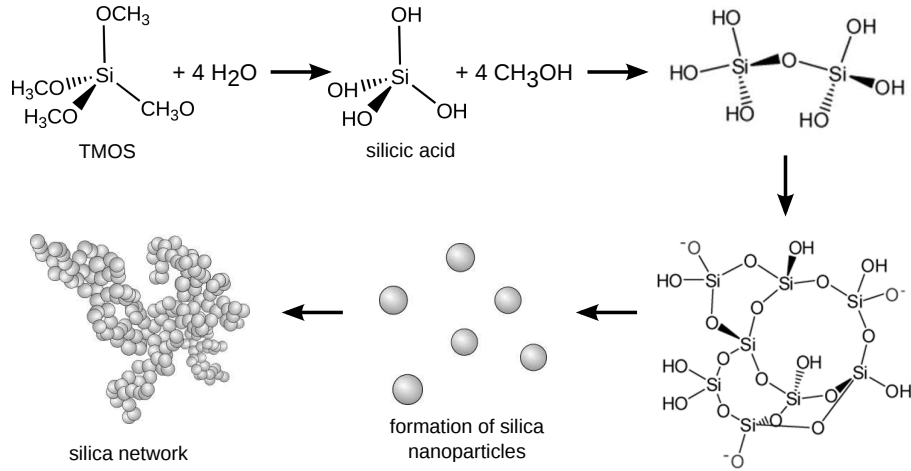


Figure 4.11: The sol-gel process starting by hydrolysis of TMOS

$S_{W:T}$	TMOS (g)	CH ₃ OH (g)	H ₂ O (g)
2	5	4	1.18
6	5	4	3.55

Table 4.7: Composition of sol-gels

4.2.2 Experimental results

Sample preparation

Sol-gels were prepared by mixing TMOS, methanol, and water. The process of gel formation starting with tetramethyl orthosilicate (TMOS) as a precursor is depicted in figure 4.11. It starts by hydrolysis of TMOS to silicic acid. Condensation reactions then result in siloxane bonds (Si-O-Si) and methanol as a by-product. Later, particles are formed that fuse into clusters and chains that eventually link to a porous network. When the network extends through its entire volume, the sample loses its fluidity (*gel point*).

Methanol is added in order to allow mixing of water and TMOS. Methanol is also released during the hydrolysis of TMOS to silicic acid, therefore using methanol as a mixing agent leads to the simplest possible chemical composition of the resulting gel. Sol-gels with two different water contents were prepared. The compositions of the prepared sol-gels are listed in table 4.7. $S_{W:T}$ denotes the mole (stoichiometric) ratio of water and TMOS. In the sol-gel with $S_{W:T} = 2$, all water is consumed by the hydrolysis, the resulting material is formed by a silica porous network filled mainly by methanol. In the case of the sol-gel with $S_{W:T} = 6$, pores of the resulting gel are filled by a mixture of methanol and water. The hydrolysis and gel formation is faster with increasing $S_{W:T}$. Gel point was ~ 184 hours for $S_{W:T} = 2$ and ~ 23 h for $S_{W:T} = 6$ sol-gel. Addition of cobalt chloride hexahydrate in the solution speeds up the polymerisation process. Gel point of $S_{W:T} = 2$ sol-gel containing 20 mM $\text{CoCl}_2 \cdot 6\text{H}_2\text{O}$ was ~ 118 hours and ~ 10 hours for $S_{W:T} = 6$.

H ₂ O mole fraction	λ_{max} (nm)	ϵ_{max} (M ⁻¹ cm ⁻¹)
0	529	11.2
0.64	512	5.7
0.99	511	5.1

Table 4.8: Absorption of [Co(H₂O)₆]²⁺ in water/methanol mixtures

Perylene and cobalt chloride hexahydrate (CoCl₂·6H₂O) were purchased from Sigma-Aldrich and were used as received. Perylene and cobalt were added from stock solutions in methanol of known concentration prior to addition of water which initiates the hydrolysis.

Absorption spectra

Due to the formation of silica particles and clusters, absorption spectra of sol-gels are affected by light scattering. Because the efficiency of Rayleigh scattering is proportional to λ^4 , it is manifested by stronger “tilt” of absorption with increasing polymerisation time with higher apparent absorbance at shorter wavelengths. To eliminate this effect, absorption of a “blank” sol-gel sample, with no perylene and no [Co(H₂O)₆]²⁺ added, was also recorded at different polymerisation times to provide data for background subtraction.

The absorption spectrum of perylene in a sol-gel remains unaltered with polymerisation time (data not shown). Figures 4.12 and 4.13 show the absorption spectra of perylene and cobalt in $S_{W:T} = 2$ and $S_{W:T} = 6$ sol-gel, respectively, recorded at different polymerisation times. It is obvious that for both sol-gel compositions, the absorption of [Co(H₂O)₆]²⁺ changes in the early polymerisation times. This change is due to decrease of the water content in the sample during the polymerisation process. As can be seen in figure 4.15, both the absorption peak position and the maximal extinction coefficient of [Co(H₂O)₆]²⁺ is different in water and in methanol. The measured maximal extinction coefficient of [Co(H₂O)₆]²⁺ is 11.2 M⁻¹cm⁻¹ in methanol and 5.1 M⁻¹cm⁻¹ in water.

Fig 4.14 shows the comparison of absorption of perylene and [Co(H₂O)₆]²⁺ in $S_{W:T} = 2$ and $S_{W:T} = 6$ sol-gel recorded after the gel point. The maximum and position of cobalt absorption in the $S_{W:T} = 2$ sol-gel corresponds to the much smaller water content in the sol-gel (8.3 M⁻¹cm⁻¹ and 527 nm). The absorption spectrum of cobalt in the $S_{W:T} = 2$ sol-gel with the maximal extinction coefficient 5.6 M⁻¹cm⁻¹ at 512 nm indicates more water-like environment.

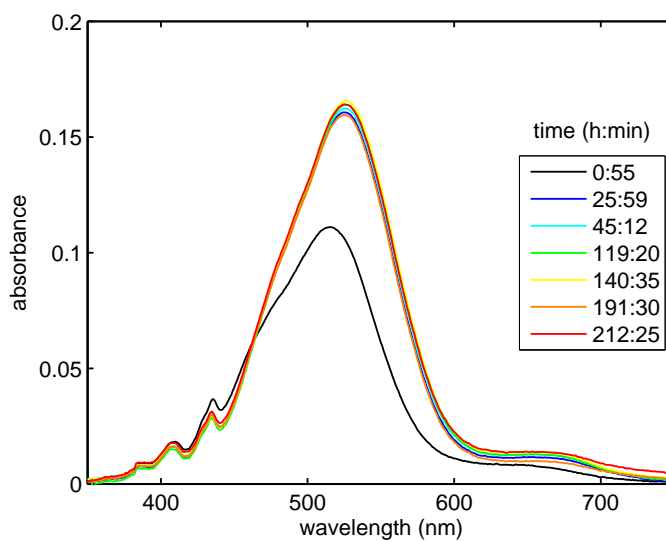


Figure 4.12: Absorption spectra of perylene and cobalt in $S_{W:T} = 2$ sol-gel recorded at different times after sample preparation. Concentration of $[\text{Co}(\text{H}_2\text{O})_6]^{2+}$ is 20 mM. The maximum absorbance corresponds to molar extinction of $8 \text{ M}^{-1}\text{cm}^{-1}$. Concentration of perylene is $0.4 \mu\text{M}$.

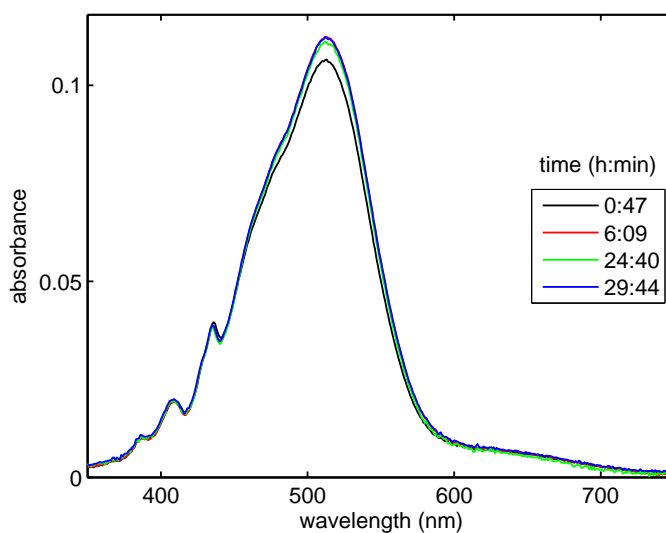


Figure 4.13: Absorption spectra of perylene and cobalt in $S_{W:T} = 6$ gel recorded at different times after sol-gel preparation. Concentration of $[\text{Co}(\text{H}_2\text{O})_6]^{2+}$ was 20 mM. The maximum measured absorbance corresponds to molar extinction coefficient of $5.5 \text{ M}^{-1}\text{cm}^{-1}$. Concentration of perylene is $0.4 \mu\text{M}$.

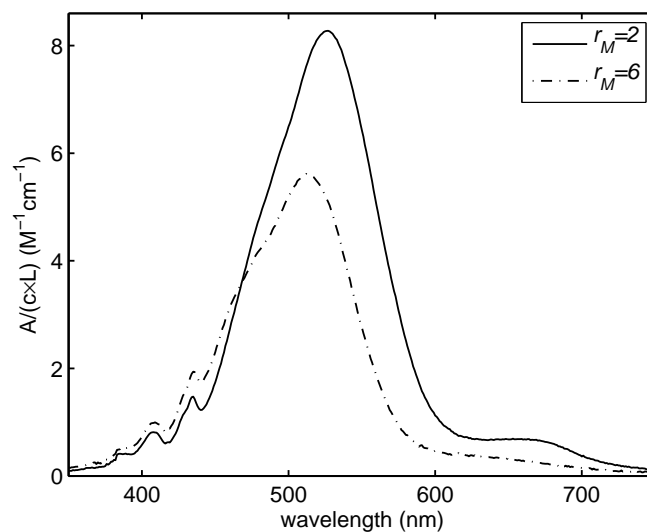


Figure 4.14: Comparison of absorption spectra of $[\text{Co}(\text{H}_2\text{O})_6]^{2+}$ in two sol-gels of different compositions after the gel point. Concentration of $[\text{Co}(\text{H}_2\text{O})_6]^{2+}$ in both samples was 20 mM and perylene 0.4 μM . The absorption spectrum of the sample with $S_{\text{W:T}} = 2$ was measured 140:35 h after sample preparation, absorption spectrum of the sample with $S_{\text{W:T}} = 6$ was measured 29:44 h after preparation.

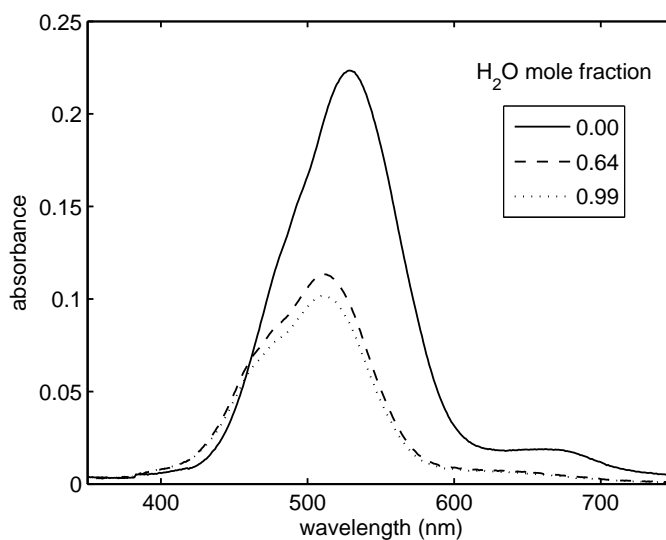


Figure 4.15: Absorption spectra of $[\text{Co}(\text{H}_2\text{O})_6]^{2+}$ in methanol and water/methanol mixture. The concentration of $[\text{Co}(\text{H}_2\text{O})_6]^{2+}$ was 20 mM in all three samples.

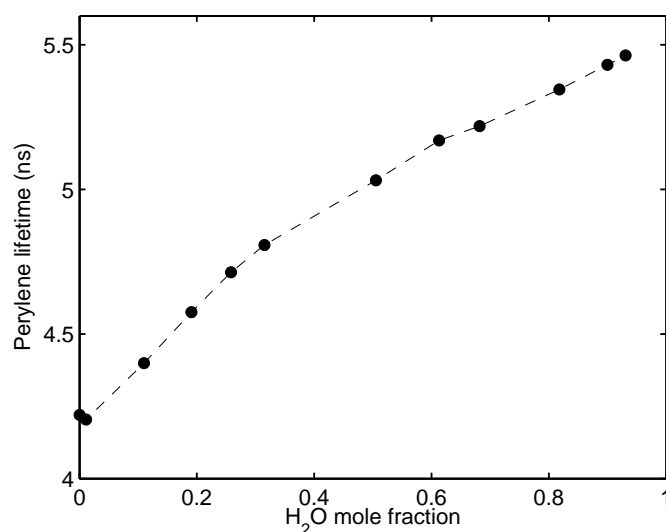


Figure 4.16: Fluorescence lifetime of perylene in water/methanol mixture.

Time-resolved fluorescence

A pulsed diode laser emitting at 405 nm was used as excitation source in all time-resolved studies with perylene. No emission monochromator was used, an absorption filter with 435 nm cut-off wavelength was inserted in the detection path to remove scattered excitation light.

The fluorescence lifetime of perylene in water/methanol mixture depends strongly on the content of water. As can be seen in figure 4.16, the lifetime of perylene increases with increasing water mole fraction³ in the sample. A decay of perylene in neat water was not recorded due to very low solubility. The perylene solubility in methanol, on the other hand, is high.

In neat methanol, perylene is strongly quenched in the presence of cobalt. The Stern-Volmer plot (figure 4.17) shows a linear dependence of τ_0/τ on the quencher concentration, as is expected for diffusion-controlled quenching. A slight deviation of recorded fluorescence decays from the single-exponential law was observed. This is believed to be due to the transient effect in quenching [77]. However, the deviation is minute in methanol.

Due to the perylene lifetime dependence on the solvent composition, it is necessary to verify that the perylene lifetime in a sol-gel does not change and all observed changes of the fluorescence decay are caused by interaction with quencher. The recorded decays of perylene in $S_{W:T} = 2$ and $S_{W:T} = 6$ sol-gels

³The mole fraction of i^{th} component in a mixture is defined as the amount of the substance divided by the total amount of all substances in the system,

$$x_i = \frac{n_i}{\sum_j n_j}$$

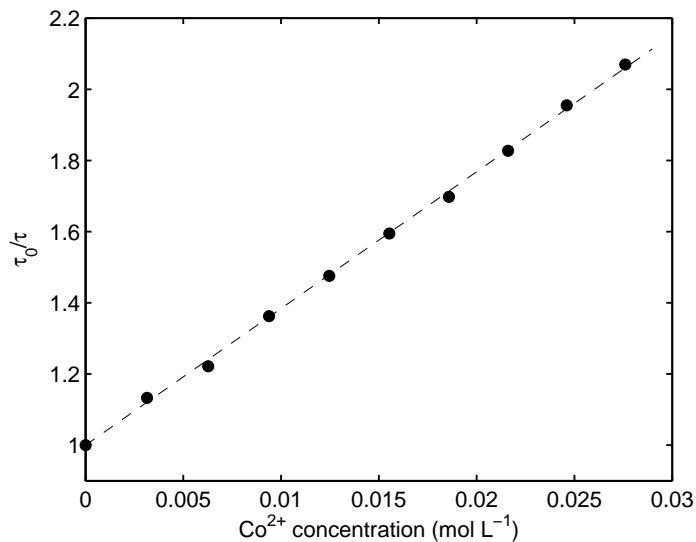


Figure 4.17: Stern-Volmer plot of perylene quenched by cobalt based on average perylene fluorescence lifetimes.

	time (hours)	τ (ns)	χ^2
$S_{W:T} = 2$	26.9	4.64	1.14
	44.6	4.43	1.07
	72.9	4.61	1.15
	120.1	4.55	1.10
	139.5	4.54	1.05
	144.4	4.51	1.20
	191.7	4.53	1.10
	194.5	4.52	1.05
$S_{W:T} = 6$	0.4	4.93	1.17
	0.9	4.94	1.01
	2.9	4.95	1.06
	5.7	4.95	1.12
	23.0	4.91	1.12

Table 4.9: Fluorescence lifetime of perylene in $S_{W:T} = 2$ and $S_{W:T} = 6$ gel without presence of quencher. Decay data fitted by single exponential model. The mean lifetime value is 4.54 ± 0.07 ns for $S_{W:T} = 2$ and 4.93 ± 0.02 ns for $S_{W:T} = 6$

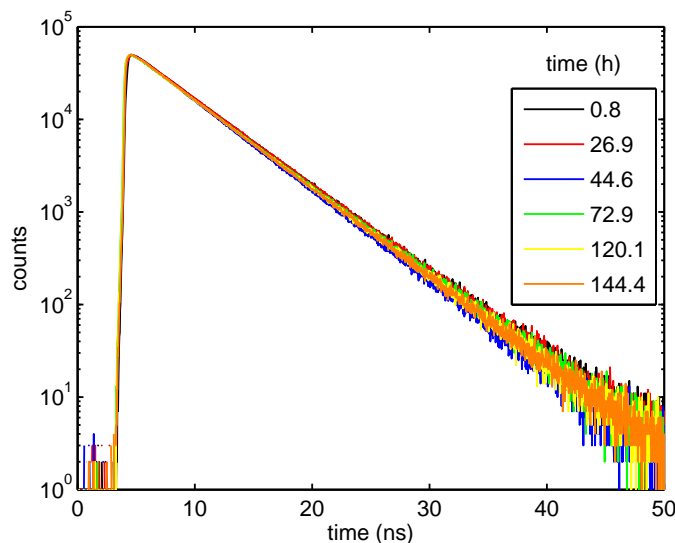


Figure 4.18: Fluorescence decays of perylene in $S_{W:T} = 2$ gel recorded at different times after sample preparation. Concentration of perylene $0.4 \mu\text{M}$.

do not indicate any fluorescence lifetime changes induced by changing composition of liquid-phase of the sol-gels. The lifetimes of recorded decays as well as the values of χ^2 are listed in table 4.9. For all decays, the single-exponential model yielded sufficiently good fits. Neither the perylene fluorescence lifetime nor χ^2 show any trend with polymerisation time. The mean fluorescence lifetime is 4.54 ns with standard deviation 0.07 ns for the sol-gel with $S_{W:T} = 2$ and $4.93 \pm 0.02 \text{ ns}$ for $S_{W:T} = 6$. The longer lifetime of perylene fluorescence in the sol-gel with the higher water content ($S_{W:T} = 6$) is consistent with lifetime dependency on water mole fraction in the water/methanol mixture (figure 4.16). The recorded decay curves for the $S_{W:T} = 2$ sol-gel are shown in figure 4.18.

As can be seen in figure 4.19, the fluorescence lifetime of perylene in the sample containing $[\text{Co}(\text{H}_2\text{O})_6]^{2+}$ is clearly decreasing with increasing polymerisation time. In other words, quenching of perylene by $[\text{Co}(\text{H}_2\text{O})_6]^{2+}$ gets more effective with ageing of the sol-gel.

In order to visualise the development of perylene quenching by $[\text{Co}(\text{H}_2\text{O})_6]^{2+}$, the *average fluorescence lifetime* was plotted as a function of polymerisation time in figure 4.20. The average lifetime of a multi-exponential fluorescence decay $I(t) = \sum_i \alpha_i e^{-\frac{t}{\tau_i}}$ is defined as

$$\tau_{avg} = \frac{\sum_i \alpha_i \tau_i}{\sum_j \alpha_j}. \quad (4.2)$$

This parameter is equal to the normalised area under the decay curve,

$$\int_0^\infty I(t) dt = \int_0^\infty \sum_i \alpha_i e^{-\frac{t}{\tau_i}} dt = \sum_i \alpha_i \tau_i = \tau_{avg} \sum_i \alpha_i$$

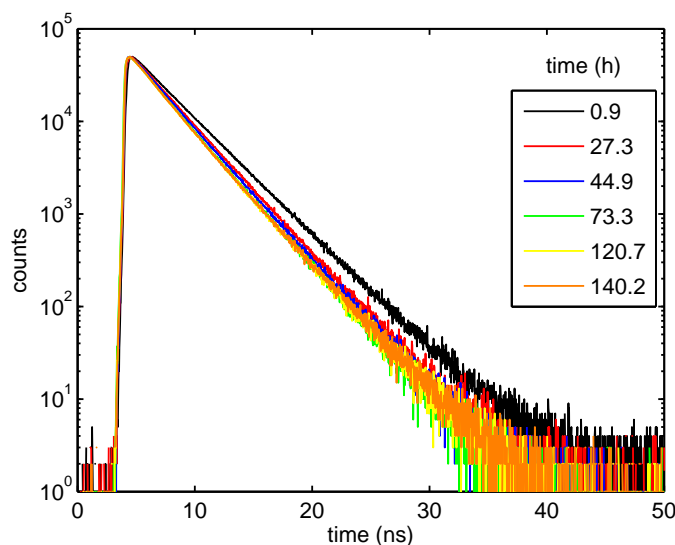


Figure 4.19: Decays of fluorescence of perylene and cobalt in $S_{W:T} = 2$ gel recorded at different times after sample preparation. Perylene concentration $0.4 \mu\text{M}$, $[\text{Co}(\text{H}_2\text{O})_6]^{2+}$ 20 mM .

and thus it is proportional to the quantum yield. The average fluorescence lifetime is therefore useful if one wants to express the quenching effect as a temporal dependency of a single parameter. The average fluorescence lifetime values plotted in figure 4.20 are calculated from the parameters yielded from the fit using the two-exponential model function, which gave reasonably good fits with χ^2 not exceeding 1.2 for both sol-gel compositions.

As can be seen from figure 4.20, the main change of the lifetime occurs prior to the gel point, which was ~ 118 hours for the $S_{W:T} = 2$ sol-gel and ~ 10 hours for the $S_{W:T} = 6$ sol-gel. In agreement with faster polymerisation with increasing $S_{W:T}$, the perylene lifetime change is faster for the $S_{W:T} = 6$ sol-gel. Because a similar behaviour of perylene fluorescence kinetics was observed on two different time scales, we can rule out the trivial explanation of lifetime shortening by an increase of the quencher concentration due to solvent evaporation.

The recorded decays of Perylene in the sol-gels containing $[\text{Co}(\text{H}_2\text{O})_6]^{2+}$ were fitted by reconvolution to the model function

$$I(t) = I_0 \exp \left[-at - 2b\sqrt{t} \right].$$

The results of the fitting are listed in table 4.10. The trend of a and b parameters are visualised in figure 4.21. The legitimacy of using this model is discussed in the next section. Both parameters show an increase with polymerisation time for both sol-gel compositions. The largest change occurs at the beginning of the sol-gel process and the parameters stabilise at about the gel point which is also indicated in the figure. Dependencies of a and b are noticeably smoother for $S_{W:T} = 6$ sol-gel. This is probably caused by the fact that measurements

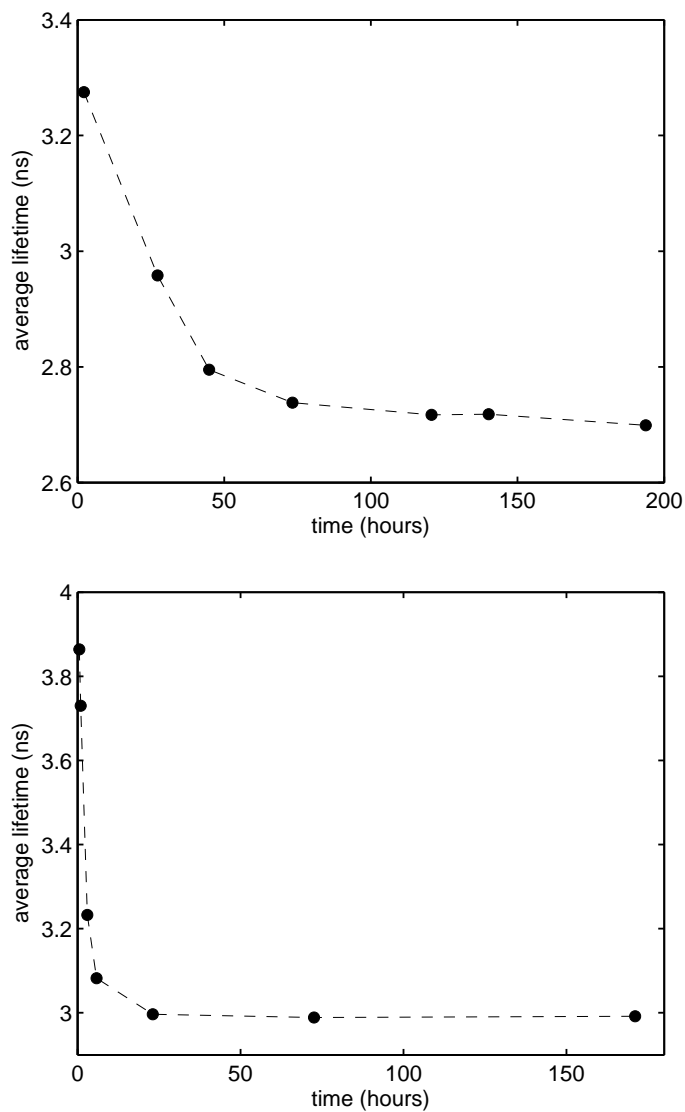


Figure 4.20: Time dependence of average fluorescence decay time of perylene in $S_{W:T} = 2$ (**top**) and $S_{W:T} = 6$ (**bottom**) sol-gel. Both sol-gels contained 20 mM $[\text{Co}(\text{H}_2\text{O})_6]^{2+}$. The average lifetime was calculated from two-exponential fit parameters.

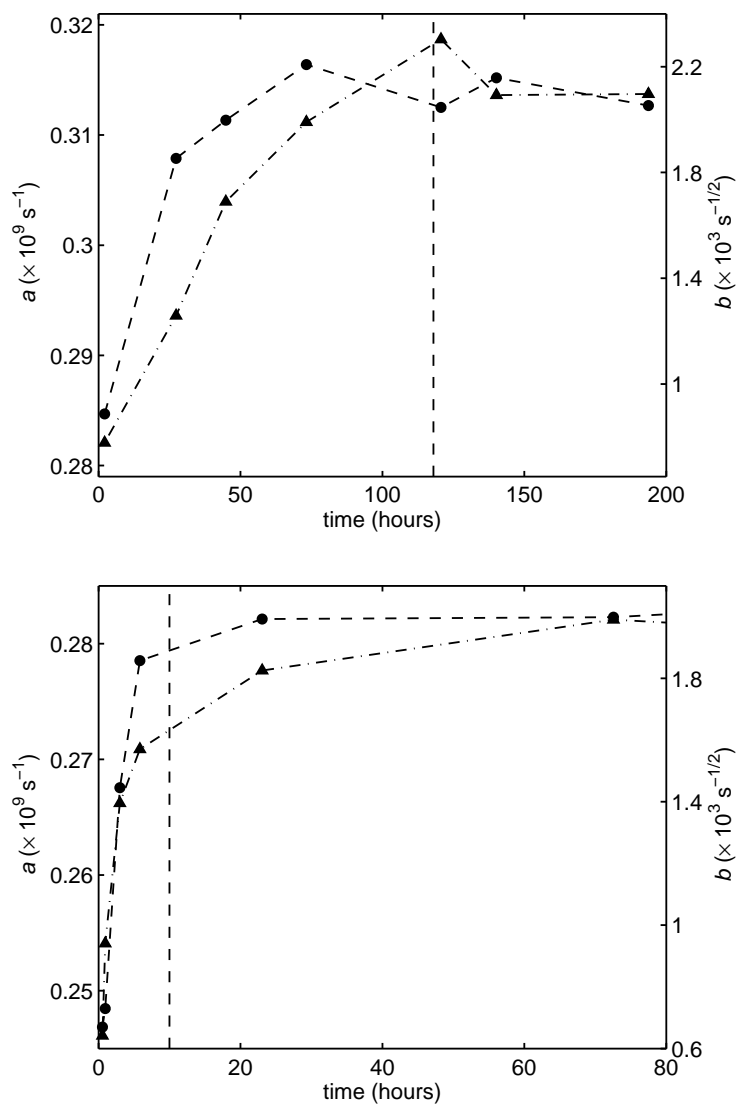


Figure 4.21: The trend in parameters a (\bullet) and b (\blacktriangle) for $S_{W:T} = 2$ (**top**) and $S_{W:T} = 6$ (**bottom**) sol-gels containing 20 mM $[\text{Co}(\text{H}_2\text{O})_6]^{2+}$. Based on data from table 4.10. The gel points are indicated by vertical dashed lines.

	time (hours)	a ($\times 10^9$ s $^{-1}$)	b (s $^{-1/2}$)	χ^2
$S_{W:T} = 2$	2.2	0.28	778	1.17
	27.3	0.31	1258	1.08
	44.9	0.31	1690	1.08
	73.3	0.32	1991	1.08
	120.7	0.31	2303	0.98
	140.2	0.32	2093	1.11
	193.8	0.31	2097	1.33
$S_{W:T} = 6$	0.6	0.25	641	1.08
	1.0	0.25	941	1.18
	3.0	0.27	1396	1.17
	5.8	0.28	1570	1.11
	23.1	0.28	1826	1.07
	72.6	0.28	1991	1.11
	171.1	0.29	1866	1.12

Table 4.10: Parameters of Perylene fluorescence decay in $S_{W:T} = 2$ and $S_{W:T} = 6$ sol-gels containing 20 mM $[\text{Co}(\text{H}_2\text{O})_6]^{2+}$. Fitted to the decay model given by equation 2.19.

with $S_{W:T} = 2$ sol-gel spanned over a considerably larger period (over a week) and the measuring device was several times switched on and off and even re-aligned for other measurements during this period, which can cause unbalanced performance of the instrument. With the $S_{W:T} = 6$ sol-gel, on the other hand, the apparatus was continuously running.

The measurement of a perylene fluorescence anisotropy decay can help to verify the localisation of the fluorophore, which is expected to be in the liquid phase filling the pores of the resulting gel structure. The anisotropy decay shown in figure 4.22 was recorded with the $S_{W:T} = 6$ sol-gel approximately 190 hours after sol-gel mixing – i.e. several days after the gel point. Sample was cooled to -27 °C (246 K). Anisotropy of perylene fluorescence decays to zero within less than 1 ns, which indicates fast fluorescence depolarisation due to Brownian rotation of the fluorophore. Therefore, we can assume that perylene is indeed localised in the liquid phase of the gel. Slightly lower value of the initial anisotropy⁴ can be caused by the limited temporal resolution of the measuring instrument as well as light depolarisation due to light scattering.

The effect of temperature on the quenching efficiency was studied with the sol-gel $S_{W:M} = 6$. The sample was left to gel (gel point was ~ 10 hours) and several days were allowed for the structure to strengthen. Fluorescence decays recorded at -27 , -13 , 1 and 15 °C are shown in figure 4.23. The average fluorescence lifetime is clearly shorter with increasing temperature which is a sign of collisional quenching.

⁴Initial anisotropy $r_0 = 0.34$ was recorded for perylene dissolved in glycerol at 20.3 °C using the same lifetime spectrophotometer.

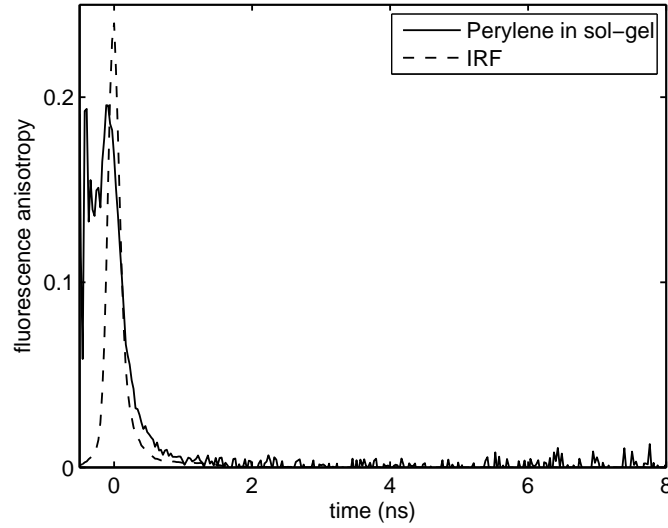


Figure 4.22: Fluorescence anisotropy of perylene in $S_{W:T} = 6$ sol-gel. Perylene $0.4 \mu\text{M}$, no $[\text{Co}(\text{H}_2\text{O})_6]^{2+}$ present, polymerisation time ~ 190 hours (i.e. several days after the gel point)

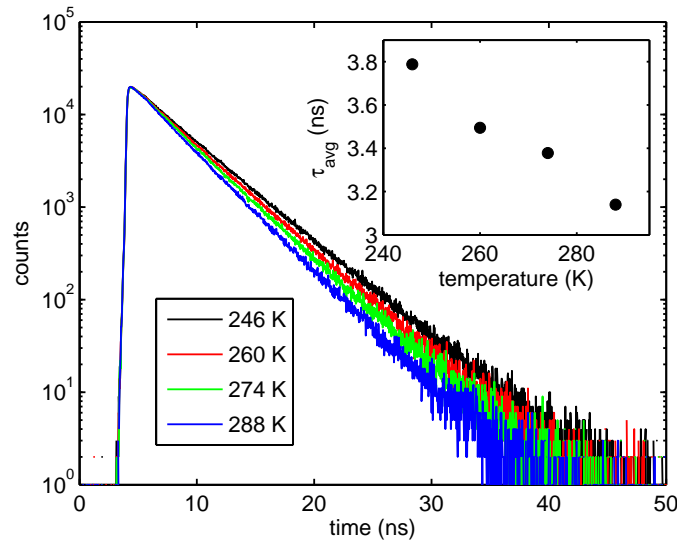


Figure 4.23: Fluorescence decays of perylene in $S_{W:M} = 6$ sol-gel containing $20 \text{ mM } [\text{Co}(\text{H}_2\text{O})_6]^{2+}$ recorded at different temperatures. Inserted: temperature dependence of the average fluorescence lifetime (based on two-exponential fits of the recorded decays).

4.2.3 Discussion

In the case of resonance energy transfer from a fluorescent donor to an acceptor with a random orientation ($\kappa^2 = 2/3$), fluorescence of the donor decays according to equation,

$$I(t) = I_0 \exp \left[-\frac{t}{\tau_D} - 2\gamma \sqrt{\frac{t}{\tau_D}} \right] \quad (4.3)$$

where τ_D is the lifetime of the donor in absence of an acceptor (see section 2.2.3). When this model is applied to the perylene fluorescence decays recorded in sol-gel containing $[\text{Co}(\text{H}_2\text{O})_6]^{2+}$, the fit generally gives an acceptable χ^2 , but the parameter τ_D does not recover the value of perylene fluorescence lifetime in sol-gel in absence of $[\text{Co}(\text{H}_2\text{O})_6]^{2+}$. In addition, when the τ_D parameter is fixed during the fitting process, equal to the value of perylene fluorescence lifetime recorded without $[\text{Co}(\text{H}_2\text{O})_6]^{2+}$, the model does not give satisfactory fits. In most cases, the minimum of the χ^2 even could not be found, i.e., the fitting routine failed. This strongly indicates that the model 4.3 is not appropriate.

The possible explanation is that before the energy from perylene is transferred to cobalt by the long-range dipole-dipole interaction, perylene is de-excited by collision with cobalt, as it was shown for low-viscosity solvent (methanol), where the diffusion length of perylene during the excited state lifetime is much larger than Förster radius for perylene-cobalt pair, $\sqrt{2D\tau_D} = l_{diff} \gg R_0$, where D is the sum of diffusion coefficients of the donor and the acceptor. Macnaught suggested to account for the effect of collisional quenching by adding a single-exponential decay component to 4.3, i.e.,

$$I(t) = I_0 \exp \left[-\frac{t}{\tau_D} - 2\gamma \sqrt{\frac{t}{\tau_D}} \right] + I_1 \exp \left[-\frac{t}{\tau_1} \right] \quad (4.4)$$

with τ_D fixed to the value of donor (perylene) fluorescence lifetime in absence of the acceptor [26]. This model supposes combination of two quenching mechanisms – FRET and collisional quenching. The parameter τ_1 would then reflect the frequency of collisions with the quencher. The application of decay model function 4.4 in the studied case, however, is not entirely correct because fluorescence of perylene quenched by cobalt in water/methanol mixtures showed slight deviation from the single-exponential behaviour, thus, purely collisional quenching would not result in a single-exponential decay which is supposed in 4.4. Despite that, using the model function 4.4 yields satisfactory fits. The contrary would be rather surprising since the recorded decay data can be fitted well with two-exponential model (with four independent parameters) and 4.4 contains five parameters - I_0 , I_1 , τ_D , τ_1 and γ . From trends of relative amplitudes I_0 and I_1 yielded by fitting recorded decays using 4.4, Macnaught concludes that the importance of collisional quenching decreases with increasing polymerisation time while the contribution of the FRET component increases, probably due to increasing viscosity of the sol-gel mixture.

The strong temperature dependency of the quenching efficiency suggests that collisional quenching might be a dominant effect in the studied case. It has been shown that perylene is located in the liquid filling the pores of the resulting gel structure and that the sol-to-gel transition does not affect its photophysics. Collisional quenching would require the presence of diffusing cobalt in the liquid

as well. Positive cobalt ions are attracted to the negatively charged silica surface through an electrostatic force [51]. Thus, it can be expected that some fraction becomes adsorbed on silica. A simple experiment showed that the coupling to the silica is pretty weak: if the monolith was fragmented into small pieces – in order to increase the interface area – and immersed in methanol, some fraction of cobalt would diffuse out of the gel fragments. This could be observed as a colouring of methanol. In other words, cobalt could be easily “washed out” of the solidified gel structure. Therefore, it can be assumed that a substantial fraction of cobalt ions can be located in the liquid phase and collisionally quench perylene fluorescence.

In order to test the possibility of interpretation of recorded data in terms of collisional quenching, the decay model function suggested by Ware *et. al.* [36–38] was applied in the data analysis,

$$I(t) = I_0 \exp \left[-at - 2b\sqrt{t} \right]. \quad (4.5)$$

The equation 4.5 has a similar form to 4.3 – it can be obtained from 4.3 by substituting $a = \tau_D^{-1}$ and $b = \gamma \times (\sqrt{\tau_D})^{-1}$. However, the two decay model functions originate in distinctive phenomena and the parameters are interpreted differently. The model 4.5 assumes diffusive character of quenching with a deviation from the single-exponential law caused by the transient effect (see section 2.2.2). Parameter

$$a = \frac{1}{\tau} = \frac{1}{\tau_0} + 4\pi D\sigma N_A [Q],$$

is an inverted value of a single fluorescence lifetime which is reduced compared to the unquenched lifetime τ_0 due to collisions with a quencher at rate given by Smoluchowski equation. The value of parameter

$$b = 4\sigma^2 N_A \sqrt{\pi D} [Q].$$

determines how much the decay deviates from single-exponential. The transient effect is usually negligible for small amounts of quenching and low viscosity solvents. It becomes more substantial in moderately viscous solvents and larger amounts of quenching. Recorded decays of perylene fluorescence quenched by $[\text{Co}(\text{H}_2\text{O})_6]^{2+}$ in neat methanol were slightly (but clearly) non-exponential and the deviation from the mono-exponential function was significant in sol-gels. This, together with the results of the fluorescence anisotropy experiment, suggests that the environment where the quenching happens has low to medium (micro-) viscosity. The increase of a and b with polymerisation time indicates that the rate of collisions increases and the deviation from single-exponential decay is stronger. Both a and b depend on σ , D and $[Q]$. The radius⁵ σ can be expected to be constant during the sol-gel process. The sum of fluorophore and quencher diffusion coefficients D is expected to decrease with polymerisation time due to increasing viscosity in the sample (although the micro-viscosity in the liquid phase is much smaller than the macroscopic viscosity and the change in D can be quite small). This leaves a conclusion that the quencher concentration $[Q]$, i.e., the concentration of Co^{2+} interacting with perylene, is increasing

⁵The kinetic model 4.5 supposes that the fluorophore is instantly de-excited upon contact with the quencher, i.e., when their mutual distance is smaller than σ – so-called *action sphere radius*. The value of σ for perylene quenched by $[\text{Co}(\text{H}_2\text{O})_6]^{2+}$ was determined to be ≈ 12 Å.[77]

with polymerisation time and thus the quenching of perylene gets more effective, despite slightly slower diffusion. That is, if the proposed kinetic model 4.5 is applicable. The amount of adsorbed Co^{2+} depends on the available silica surface. The structure of the resulting gel depends strongly on the water content in the pre-gel mixture. Sol-gels with higher water content are known to have more fractal-like structure and thus larger silica surface. This is consistent with the stronger quenching observed in the $S_{\text{W:M}} = 2$ gel compared to $S_{\text{W:M}} = 6$ at the same concentration of $[\text{Co}(\text{H}_2\text{O})_6]^{2+}$ – the average fluorescence lifetime recorded after the gel point was ≈ 2.7 ns for $S_{\text{W:M}} = 2$, and ≈ 3.0 ns for $S_{\text{W:M}} = 6$, both with 20 mM $[\text{Co}(\text{H}_2\text{O})_6]^{2+}$ (figure 4.20). Formation of clusters in the sol can considerably reduce the silica surface and lead to an increase of freely diffusing Co^{2+} .

No contradictory information was found that would reject the use of the fluorescence kinetic model 4.5 in the analysis of the recorded decays. Therefore one of the possible interpretations of the experimental observations is that quenching of perylene fluorescence by Co^{2+} is governed by diffusion of both fluorophore and the quencher. The actual mechanism of the de-excitation remains unclear – it can be collision-induced short-range Dexter exchange or dipole-dipole interaction or their combination. It should be noticed here that interpretation of non-exponential decays is a rather delicate problem. Several effects can result in a complicated fluorescence decay. Silica sol-gel is a complex environment offering many opportunities for inhomogeneous fluorophore-quencher interactions. For example, the viscosity, as well as the Co^{2+} concentration, can vary on the microscopic scale in a formed gel.

4.3 Improved biocompatibility of silica sol–gels

4.3.1 Introduction

In recent years the encapsulation of protein within silica has been demonstrated using the sol–gel process [86]. During gelation a hydrated biocompatible silica matrix containing pores of typically ~ 10 nm are formed around individual protein molecules, matching their size whilst connecting to the network by smaller pores of ~ 1 nm; the latter acting as a conduit for analytes of interest while excluding potentially interfering macromolecules. These features are ready-made for sensing applications and could potentially be used to simulate natural conditions in single protein research with a view to answering such fundamental questions as – do all proteins of a given type fold by the same pathway and how does protein aggregate? However, a well known problem when preparing silica sol–gels using orthosilicate precursors is the release of alcohol during the reaction, which denatures protein through an alteration of the native structure [87, 88]. The degree to which protein is altered by alcohol varies with each protein and protocols based on other than orthosilicate precursors have been shown to introduce new problems (e.g., sodium ions from water soluble silicate). Evaporation of alcohol from the sol prior to addition of protein is widely used, typically for 25 min as described for horseradish peroxidase [89].

In the work presented in this section, the polarity sensitive fluorescent probe prodan was used to monitor methanol and thereby define a protocol with enhanced bio-compatibility which uses a hydrolysis period of at least 24 h at $+5^\circ\text{C}$ followed by a vacuum distillation. This improved bio-compatibility was demonstrated on the environment-sensitive protein allophycocyanin (APC) which exists as a trimer in its native form, but readily dissociates into monomers in the presence of alcohol. The recorded fluorescence emission of encapsulated APC corresponds to the stable trimeric form in an aqueous environment, for an ageing period of up to approximately 500 h, which provides an opportunity for extensive investigation of the native form rather than distorting the native structure by having to covalently bind the monomer units into the trimeric form as was previously required. Most protein of interest to biology is extremely difficult to study at the single-molecule limit in natural form and this difficulty is exacerbated in sol–gel pores. However, a few studies have been reported on stable single proteins such as green fluorescent protein entrapped in a sol–gel matrix [16]. Consequently, the higher stability afforded by the protocol described here could open-up single molecule applications of wider bearing such as protein folding and aggregation.

APC belongs to the phycobiliprotein family present as aggregates in phycobilisomes that lie near chlorophyll reaction centers in *Cyanobacteria* and *Rhodophyta* (blue, green and red algae, respectively). In its trimeric form APC shows a fluorescence peak centered at 660 nm associated with exciton splitting between closely-spaced pairs of phycocyanobilin chromophores [90]. If the protein is exposed to organic solvents, e.g., methanol, the trimer is disaggregated into monomers and the chromophore–chromophore coupling falls off resulting in a blue shift of the phycocyanobilin peak emission to ~ 640 nm. Until the present work APC was difficult to study in the native form as covalent cross-linking was needed to preserve the trimeric form down to the single-molecule level [90]. Previous attempts at preserving the trimeric structure of APC in a sol–gel matrix

have been unsuccessful, even when maintaining neutral pH either before or after gelation [91], presumably due to the extreme sensitivity of the protein (through such mechanisms as disrupted hydrogen bonding) to the vicinal solvents and pH changes generated, resulting in dissociation to the monomeric form [92].

The ability to entrap a protein, as is demonstrated here with APC, illustrates the potential of single molecule fluorescence confined within nano-pores for studying the protein aggregation that underpins diseases such as the fatal prion disorders of protein folding (BSE, Creutzfeld-Jacob disease and possibly Alzheimer's and Parkinson's diseases) at their most fundamental level, with potentially step-change implications for generic understanding not only disease pathology but also therapeutics. The latter is facilitated because the connectivity of the conduit network to the protein in silica provides an ideal platform for studying toxicity, drug intervention therapies, etc., at the single molecule level. Also, the encapsulation of APC in silica sol-gel nano-pores demonstrates further progress towards metabolic sensing in protein based assays in general. APC is a naturally fluorescent protein in the visible region of the spectra and it has attracted considerable interest in various bio-assays. For example, APC labeling of the glucose-binding lectin, concanavalin A (Con A) has been used to detect glucose through a time-resolved fluorescence resonance energy transfer sensing scheme [93–95]. The problem of Con A agglomeration can in principle be overcome by means of a nano-porous structure and having a biocompatible and optically transparent matrix such as silica opens-up the possibility of achieving a practicable implant with which to detect blood glucose via optical interrogation. Similarly porous silica sol-gel materials may provide a platform for integration within “lab-on-a-chip” sensors which are capable of bringing to bear the whole panoply of fluorescence techniques and technology to the point-of-care. This includes for example, intrinsic protein fluorescence excited with ultra-violet light emitting diodes [96], microfluidics [97], fluorescence resonance energy transfer to detect metal ions either directly [98] or indirectly using a chelate [99] and anisotropy [100].

4.3.2 Experimental

Porous silica sol-gels were synthesized by acid-catalysed hydrolysis of tetramethyl orthosilicate (TMOS) with methanol as a side product. The simplified reaction mechanism was described in section 4.2.2. TMOS sol-gel was prepared by sonicating together, for 30 min, 4.5 mL TMOS, 5 mL distilled water and 0.1 mL hydrochloric acid (0.1 N); giving a molar ratio $\text{H}_2\text{O}/\text{TMOS} = 9.4$ where the excess water ensures complete hydrolysis of the orthosilicate. APC was not added at this point (as commonly done), but instead the sol was kept at $+4^\circ\text{C}$ for 5 days, allowing the hydrolysis step to effectively reach completion without promoting gelling through the condensation steps, and only then vacuum distilled at 50°C for $\sim 3-5$ min at 300 mbar to remove methanol. Distilling for any longer than this led to gelation before the APC could be added. Finally, the sol was neutralized by the addition of a mixture of 15 mL PBS (phosphate buffered saline, pH 7.4) and 15 mL borate buffer (pH 9.2). It would be preferable to only add PBS but this was found to induce a rapid transition into the gel state preventing a homogeneous dispersion of the protein. The addition of borate buffer was found to increase the sol phase lifetime to about 5 min allowing time for efficient mixing.

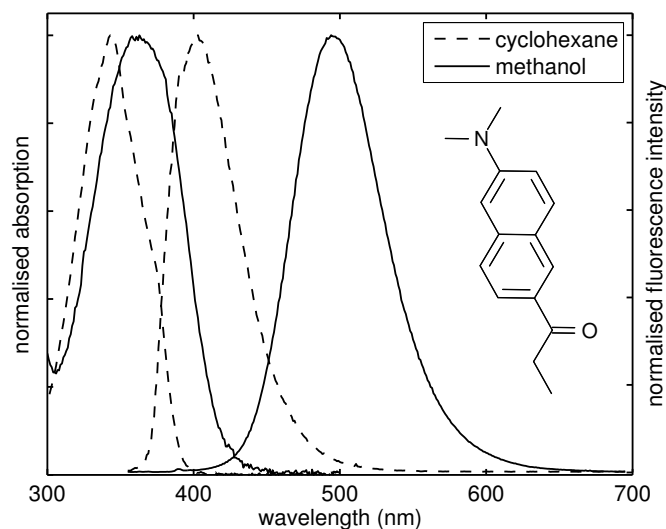


Figure 4.24: Comparison of absorption and fluorescence spectra of prodan in cyclohexane and methanol. Structure of prodan also shown.

The optimum times for the protocol were obtained using prodan (Sigma-Aldrich) in parallel measurements on equivalent sols used for protein encapsulation. Prodan was used at a concentration of $2.2 \mu\text{M}$.

APC (Sigma-Aldrich Ltd) was used without further purification. Stock solution was prepared in PBS (pH 7.4) and diluted into the vacuum distilled and neutralized sol at a concentration of $1.28 \times 10^{-7} \text{ mol dm}^{-3}$, the sol then being left to gel. Steady-state fluorescence spectra were recorded on a Jobin-Yvon Fluoromax 2 spectrometer and time-resolved decays were obtained from a Horiba Jobin Yvon IBH FluoroCube system using a NanoLED diode laser centered at 634 nm as excitation source.

4.3.3 Results and discussion

The optimum timings for hydrolysis and distillation of the silica sol were determined by investigating a separate and parallel series of samples without protein but containing fluorophore 6-propionyl-2-(dimethylamino)naphthalene (prodan) [101]. Prodan is a well-known polarity sensitive fluorescent probe (figure 4.24). The emission maximum shifts from 410 nm in cyclohexane to ~ 520 nm in water. The high sensitivity to polarity is caused by a large transition dipole moment due to photo-induced charge transfer from the amino group (electron donor) to carbonyl group (acceptor). Prodan and its derivatives (acrylodan, laurdan, patman, etc.) have become widely used in bio-medical research, e.g., studies of cell membranes.

In sol-gel, prodan is exposed to water/methanol mixture environment with increasing proportion of methanol released during the reaction. The response of prodan fluorescence to increasing methanol concentration is two-fold. Firstly

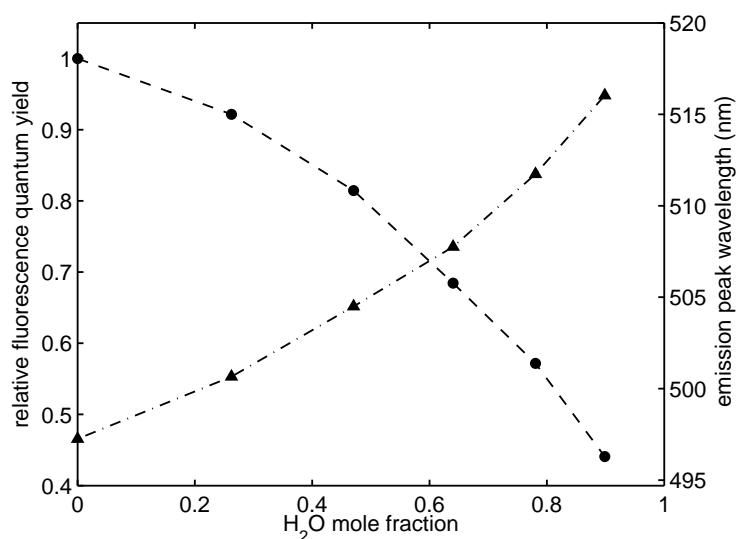


Figure 4.25: The recorded dependency of prodan quantum yield (●) and emission maximum position (▲) on water mole fraction in water/methanol solution. The concentration of prodan was 3 μ M in all samples.

a hypsochromic shift can be observed in the peak wavelength, as compared to water (in H₂O the spectrum peaked at 521 nm and in methanol at 498 nm) and secondly an increase in fluorescence intensity, i.e., quantum yield, occurs. In figure 4.25, the dependency of prodan fluorescence quantum yield and emission peak position is plotted as a function of water mole fraction in water/methanol solution.

In figure 4.26 it is shown that the fluorescence intensity of prodan dissolved in the silica sol increases for up to 24 h after initial mixing, reflecting an increased methanol concentration in the sol. After 24 h there was no change in the fluorescence intensity. Five days sol ageing was cautiously and arbitrarily chosen as a safe-period to allow hydrolysis to effectively complete. The methanol was then removed by vacuum distillation for a time as indicated by the prodan fluorescence on the same sample. The difficulty is if methanol removal is inadequate the protein denatures and if it is completely removed the gel sets before the protein is added. Figure 4.27 shows how the prodan peak fluorescence wavelength after 3 min of distillation is \sim 521 nm suggesting an aqueous environment to which protein can then be added safely. The distillation time can be extended to 5 min, beyond which the gel is formed too early for achieving a homogeneous protein dispersion.

APC dispersed in silica sol-gel monolith prepared according to the protocol presented in this report remained in a trimeric form for up to 500 h before dissociating. This is evident from the fluorescence emission spectra where a band can be seen centered at 660 nm corresponding to the exciton coupling of phycocyanin chromophores localized in different subunits of APC [92], see figure

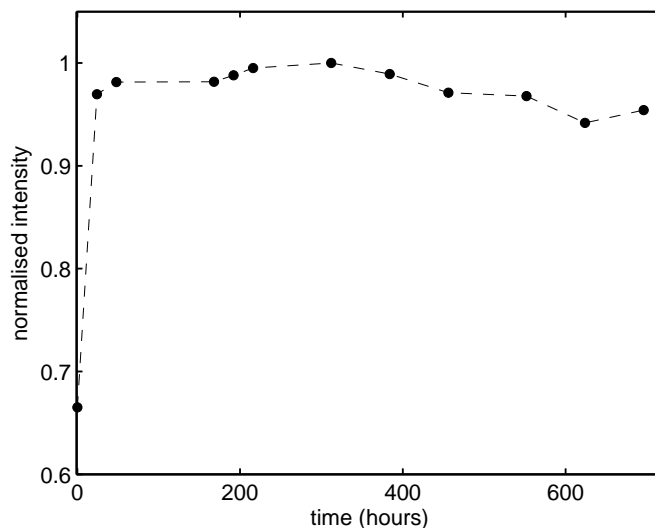


Figure 4.26: Fluorescence intensity recorded on prodan in a sol reflecting an initial increase of $\sim 50\%$ within 24 h due to methanol formation, and then stabilising. The excitation wavelength was 365 nm and the peak emission centred at 505 nm.

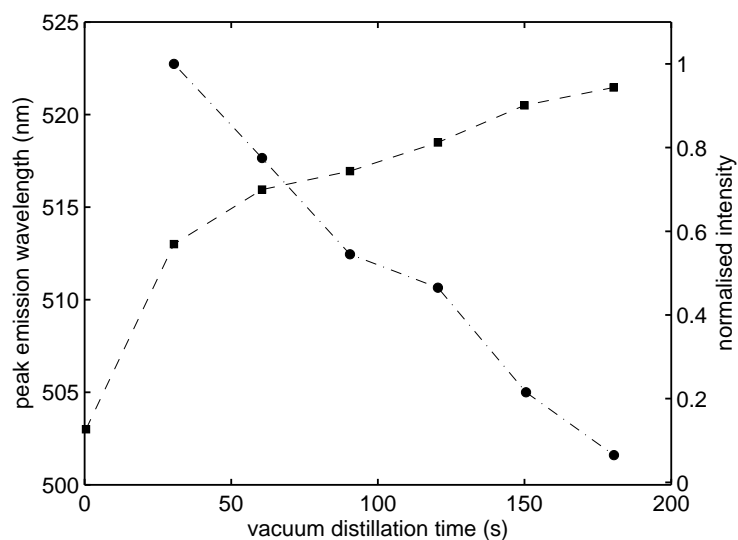


Figure 4.27: Peak emission wavelength (\bullet) and intensity (\blacksquare) observed for prodan as function of vacuum distillation time at 50°C and 300 mbar. After ~ 180 s the spectra resembles that observed for prodan in water

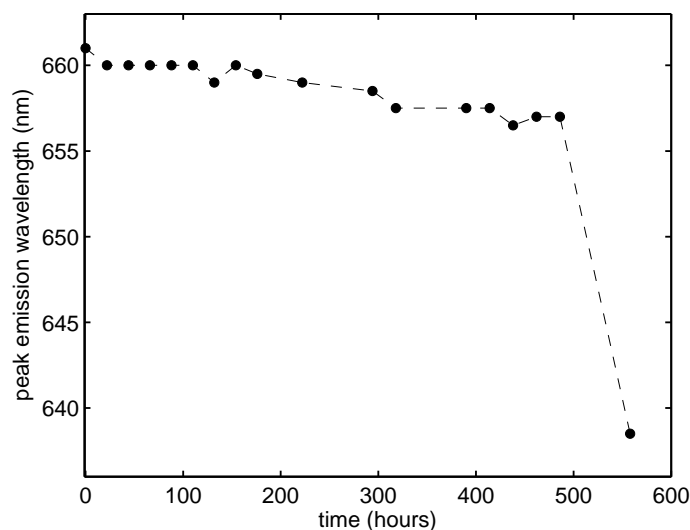


Figure 4.28: The APC fluorescence peak wavelength as function of sol-gel aging when excited at 550 nm

4.28. After ~ 500 h there is a sudden shift towards 638 nm associated with APC in the monomeric form. During this time solvent is also expelled from the silica monolith and accumulates to a ~ 1 mm thick liquid layer on the top of the sample. The change in protein is tentatively interpreted to pore shrinkage and increased exposure to silanol groups.

To illustrate the importance of complete hydrolysis on the stability of APC, the result is compared with a preparation method reported by Ferrer *et. al.* [89]. As can be seen from figure 4.29, the emission spectra recorded on APC dissolved in a sample without complete hydrolysis is consistent with the monomeric form, i.e., a blue shift in the peak wavelength and an increase in full width half maximum as compared to the spectra recorded on APC in the trimeric form. A monomer fluorescence spectrum, APC in aqueous solution at pH 4, is also shown in figure 4.29 for comparison.

Further evidence of preserving the trimeric form of APC by encapsulation can be found in ensemble fluorescence decay data. The fluorescence decay times of APC in a silica sol-gel monolith, prepared according to the protocol presented here, are shown in table 4.11 for two different polymerization times and compared to results in PBS buffer with and without methanol. The trimer decay times of 0.16 ns and 1.76 ns in PBS, as well as their relative intensities, are replicated in the sol-gel by the data taken after 24 h, indicating preservation of the trimeric form of APC. After 720 h, the value of the shorter decay component (τ_1) significantly increases and also its relative contribution increases, which indicates the presence of APC in the monomeric form.

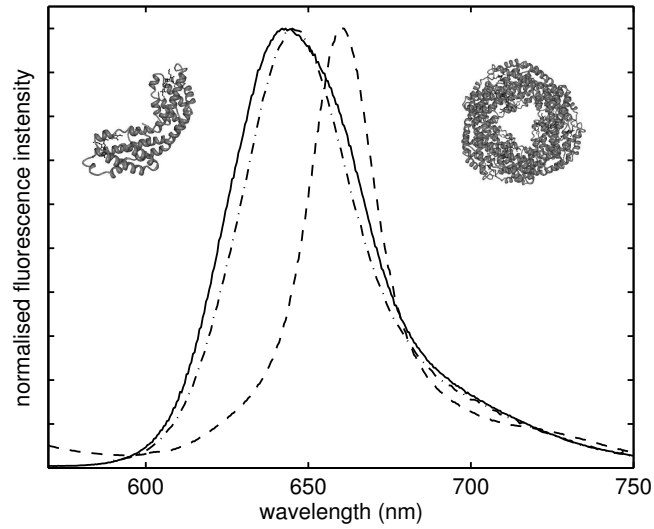


Figure 4.29: Fluorescence spectra of APC (excitation at 550 nm) encapsulated in a sol-gel monolith prepared according to the new protocol (—) and according to previous protocols (- · -). FWHM are indicated. For comparison the emission spectra of APC in its monomer form (—) is also shown (recorded for APC dissolved in water at pH 4)

APC system	a_1 (%)	τ_1 (ns)	a_2 (%)	τ_2 (ns)	χ^2
trimeric (in PBS)	2	0.16 ± 0.06	98	1.76 ± 0.01	0.97
monomeric (PBS:MeOH, 1:1)	15	0.72 ± 0.09	85	1.94 ± 0.02	1.24
sol-gel monolith 24 h	3	0.12 ± 0.02	97	1.73 ± 0.01	0.97
sol-gel monolith 720 h	19	0.72 ± 0.06	81	1.73 ± 0.01	1.07

Table 4.11: Fluorescence decay times recorded for APC. The uncertainties of the decay parameters are represented by the *asymptotic standard errors* ([5], page 134).

Chapter 5

Glucose sensing with engineered glucose binding protein

5.1 Introduction

In this chapter, a photophysical study is presented of a D-glucose/D-galactose binding-protein (GBP) labelled with the environmentally sensitive dye badan. Badan-GBP152C (the structure is shown in figure 5.1) was developed at the Diabetes Research Group, King's College, London School of Medicine, in the effort to find a suitable system for monitoring blood glucose level via fluorescence. This system exhibits a maximal $\sim 300\%$ fluorescence intensity increase when glucose is added. This range provides a sufficient dynamic range and badan-GBP152C is therefore a good candidate for construction of a fluorescence-based glucose sensor for clinical use.

Glucose sensing

Diabetic mellitus is a metabolic disease manifested by chronically elevated level of glucose in the blood of the patient. It is caused either by failure of the organism to produce enough *insulin* (type I diabetes) or defective responsiveness of cells to insulin (type II). Insulin is a hormon produced by *pancreas*. It is a peptide composed of 51 amino acids. Through the insulin production, a healthy body regulates the glucose uptake by cells from the blood. The chronic insulin deficiency causes *hyperglycemia*, i.e. high blood glucose, which can lead to a wide variety of serious health complications.

Diabetes is difficult to cure. It is treated by dietary management and appropriate medication. Depending on the severity of the disease, administration of exogenous insulin may be required. A patient with type I diabetic mellitus needs to take insulin several times throughout the day, most commonly by subcutaneous injection. The required amount of external insulin must be carefully estimated in order to ensure balanced glucose level. The excess of insulin together with insufficient nutrition income leads to acute *hypoglycemia*, i.e., low blood glucose. This state which is particularly dangerous to the nervous system.

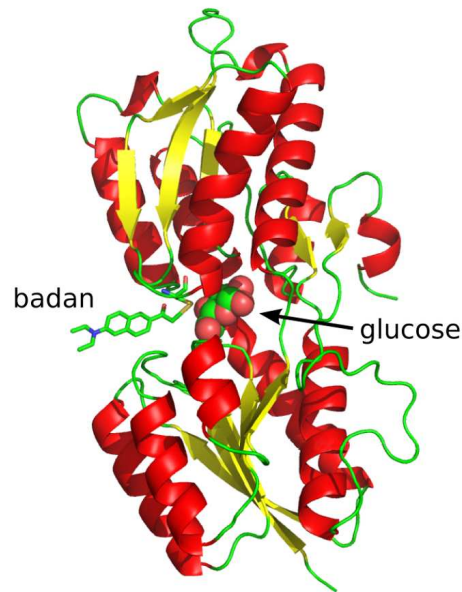


Figure 5.1: Structure of badan-GBP152C. A modified structure from Protein Data Bank repository (<http://www.pdb.org>) obtained by the X-ray diffraction method [102]. The label is located close to binding region

Therefore, the blood glucose level must be accurately and reliably monitored, so that an adequate amount of insulin can be administered. Most glucometers used today operate on the electrochemical principle. They require a blood sample obtained by pricking the skin (usually on a finger) by a small lancet. Although the volume of the blood needed by modern glucometers for the test is minimal, this method brings some discomfort to the patient, especially if more frequent reading is necessary. There is a search for novel methods for continuous and preferably non-invasive blood glucose monitoring which would improve the safety and life quality of a diabetic patient. One of proposed approaches for *in vivo* glucose monitoring is fluorescence-based sensing in which a sensor would generate a well-defined glucose-induced response detectable by the means of fluorescence spectroscopy, for example the change of fluorescence intensity or lifetime. Such sensor implanted in the body and thus permanently exposed to the blood, could be used together with an evaluation device in order to provide a feedback to an insulin pump, which would continuously adjust the administered dosage of exogenous insulin. Several systems based on glucose-sensitive bioreceptors, such as glucose dehydrogenase, glucose oxidase, lectin concanavalin A and bacterial glucose binding protein, have been studied [93, 94].

Engineered bacterial glucose binding protein

Protein is a linear chain of amino acids joined together by peptide bonds between the carboxyl and amino group of adjacent amino acid residues. The end of the chain with a free amino group is called the N-terminus and the end with a

free carboxyl group the C-terminus. The sequence of amino acid residues in the protein is defined by a sequence of a gene, which is encoded in a stretch of a DNA. In its natural form, protein is folded to a three-dimensional structure (so-called *protein tertiary structure*) which is determined by the amino acids sequence and the environment in which the protein is synthesized and allowed to fold. A globular protein is folded so that the exposure of non-polar (hydrophobic) amino acids to the surrounding water is minimised whereas polar (hydrophilic) amino acids are bound outwards, which makes the protein water soluble. Formation of intramolecular hydrogen bonds within the protein's hydrophobic core can significantly contribute to the protein's tertiary structure stability.

Some proteins may exhibit an intrinsic fluorescence (autofluorescence) due to the presence of aromatic residues – tryptophan, tyrosine or phenylalanine. In the interesting and important case of the green fluorescent protein (GFP) found in jellyfish *Aequorea victoria*, green fluorescence upon blue light exposure occurs due to a specific cyclization reaction within a tripeptide amino acid sequence consisting of serine, tyrosine, and glycine at positions 65–67 [104]. The autofluorescence can be used as diagnostics of the protein's conformation, or the fluorescent protein itself can serve, for example, as a biomarker in a study of cellular processes.

A protein can also be labelled by introduction of an extrinsic fluorescent probe that provide a fluorescence response to a conformational rearrangement of the protein which is often induced by the binding of a substrate molecule to the protein's active site. Thus, the natural behaviour of the protein can be utilised for detecting non-fluorescent molecules via fluorescence. This is the principle idea of detecting glucose using labelled D-glucose/D-galactose binding-protein (GBP) from bacteria *Escherichia coli* [106, 107]. GBP binds glucose with high affinity and galactose to a lesser degree. It is a globular protein consisting of two main domains that are connected with a “hinge” region where the active (sugar binding) site is located. When a glucose molecule is bound to GBP, the protein undergoes a large conformational change. There are two main strategies of detecting glucose using a sensor based on GBP [27]. One is to label the protein with a FRET pair – a fluorescent donor and an acceptor – at different sites on the protein. If the donor–acceptor distance differs substantially in the two conformational states, glucose can be detected via monitoring FRET rate. Other strategy is to label GBP with environment sensitive dye at suitable position. Most of GBP-based sensors are reported to have < 30% change of fluorescence signal and few up to ~ 300%.

One of GBP-based systems developed by Khan *et. al.* exhibits a 300% maximal increase of fluorescence intensity with glucose [27]. It was prepared by a site-specific labelling of the protein with environment sensitive 6-bromoacetyl-2-(dimethylamino)naphthalene (badan) at position C152¹. The procedure is described in [27] but it might be useful to give a brief overview here. To target the labelling position on the protein chain, a mutant of GBP was prepared by replacing histidine at position 152 with cysteine with site-directed mutagenesis. The cysteine residue in the resulting mutant, denoted as H152C (which means histidine at position 152 was replaced by cysteine), contains a thiol group (–S–H). The molecule of badan (structure shown in figure 5.2) contains a bromine

¹The position is expressed as the number of the amino acid in the protein sequence, counted from the N-terminus.

which readily reacts with the thiol group in the cysteine residue. As a result, badan is attached to the protein chain at the desired position through a thioether bond. The labelling of H152C mutant of GBP was accomplished by incubating a solution of the mutant in a buffer with excess of badan at room temperature. The remaining free dye is removed by gel-filtration chromatography. The abbreviation “badan-GBP152C” specifies that GBP is labelled by badan through cysteine at position 152.

5.2 Experimental

The solution of badan-labelled glucose binding protein in PBS was kindly supplied by Dr. Faaizah Khan from the Diabetes Research Group, King’s College, London School of Medicine, who performed the protein labelling and purification. The protein mutagenesis and subsequent dye labelling is quite complex and time consuming procedure. Thus, only limited amount of the protein was available and careful planning of experiments was in place. Immediately after it was delivered, the protein solution in PBS was aliquoted into plastic 1.5 mL Eppendorf test tubes and stored at approx. -5°C for later use. Entire dosage from one test tube was then diluted by PBS to fill the entire volume of a micro-cuvette.

Phosphate buffered saline and D-glucose powder were purchased from Sigma-Aldrich. Typically, 10 μL of glucose stock-solution in PBS of known concentration was successively added to the sample and sufficient time (at least 30 minutes) was allowed for the sample to stabilise before commencing measurements.

All measurements presented here were performed at room temperature, $24 \pm 1^{\circ}\text{C}$. Absorption spectra were recorded with Lambda 2 UV/Vis (PerkinElmer) spectrophotometer. Because the micro-cuvette was not suitable for absorption measurement due to the light beam geometry, absorption spectrum of badan-GBP152C was recorded using quartz $w \times l \times h = 5 \times 5 \times 40$ mm cuvette, which was carefully aligned to the beam path.

Fluorescence steady-state spectra were recorded with a FluoroMax-2 (Jobin Yvon) spectrofluorometer. The measurements on one sample spanned over a quite long period of time (up to a few days). Therefore, for monitoring of fluorescence intensity changes, a reference sample - perylene/cyclohexane solution - was used, in order to eliminate the drift of the instrument.

A TCSPC lifetime spectrofluorometer based on FluoroCube (HORIBA Jobin Yvon) was employed to record fluorescence decays. A diode laser emitting at 405 nm with $\lesssim 200$ ps FWHM of the pulse was used to excite badan. Coloured glass long-pass filter with 415 nm cut-off wavelength was used to suppress the scattered excitation light. Fluorescence decays of tryptophan were recorded using a light emitting diode with emission maximum at ~ 280 nm and ~ 1 ns FWHM.

In order to consume the smallest possible amount of sample, a quartz micro-cuvette with cell dimensions $w \times l \times h = 2 \times 10 \times 5$ mm (100 μL volume) was used for all fluorescence measurements. For recording both steady-state and time-resolved fluorescence anisotropy, it is critical to avoid any light reflections and scattering inside the sample that would lower the anisotropy value. Particularly, it turned out that the solution surface can significantly influence the anisotropy

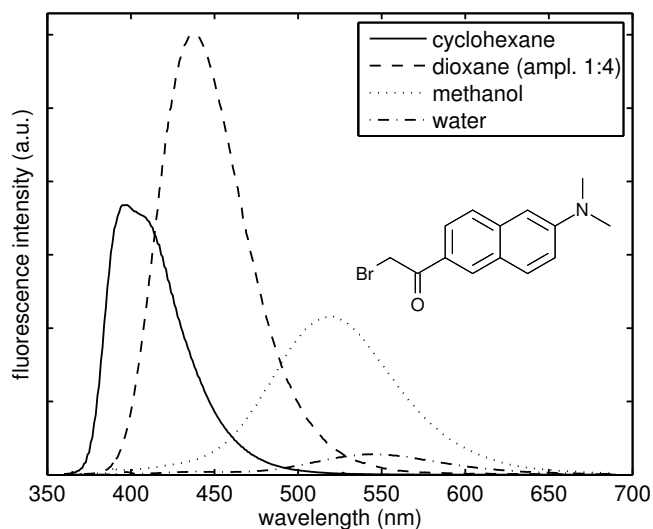


Figure 5.2: Fluorescence emission spectra of badan in different solvents. Spectra are normalised so that their area reflect relative quantum yield. The amplitude of spectrum of badan in dioxane is divided by four.

value if it overlaps the excitation or emission light path. Thus, sufficient amount of the sample had to be added into the micro-cuvette, $\geq 120 \mu\text{L}$. The feasibility of using the micro-cuvette for fluorescence anisotropy measurements was verified by measuring the anisotropy of a reference sample – perylene dissolved in glycerol. It turned out that the masking on the micro-cuvette’s facets helps to define the geometry of the arrangement and brings some advantage. However, it was necessary to carefully align the position of the micro-cuvette in the sample compartment, as well as prevent formation of air bubbles in the sample that can also lower the anisotropy value.

5.3 Results and discussion

Badan (6-bromoacetyl-2-dimethylaminonaphthalene) is a polarity sensitive fluorescent dye with a molecular structure similar to prodan (compare structures in figures 5.2 and 4.24). The only difference to prodan is the bromine atom on place of methyl in the propionyl group, which makes badan very reactive and thus allows to covalently bind badan to cystein residue in GBP by replacing hydrogen in the thiol group. Badan exhibits a large bathochromic shift (i.e., a shift to longer wavelengths) of fluorescence emission spectrum with increasing solvent polarity (figure 5.2). Badan also has a strongly solvent-dependent quantum yield. Fluorescence bandwidth, position, and decay parameters are listed in table 5.1.

	DMF	methanol	cyclohexane	dioxane
ϵ_r	38	33	2.02	2.3
λ_{max} (nm)	475.57	517.72	406.13	437.47
Δ (nm)	71.87	86.48	52.88	59.26
λ_{em} (nm)	470	540	410	-
τ_1 (%) (ns)	0.2 (3.4)	0.8 (36.9)	0.7 (21.6)	-
τ_2 (%) (ns)	1.4 (53.7)	2.5 (53.7)	2.8 (53.2)	-
τ_3 (%) (ns)	3.3 (42.9)	0.1 (9.4)	0.2 (25.2)	-
χ_2	1.40	0.99	1.17	-

Table 5.1: Photophysical properties of badan in different solvents: the solvent relative permittivity ϵ_r , the position of the emission maximum λ_{max} , the full width at half maximum Δ , the relative contribution a_i of the lifetime component τ_i . DMF = dimethylformamide

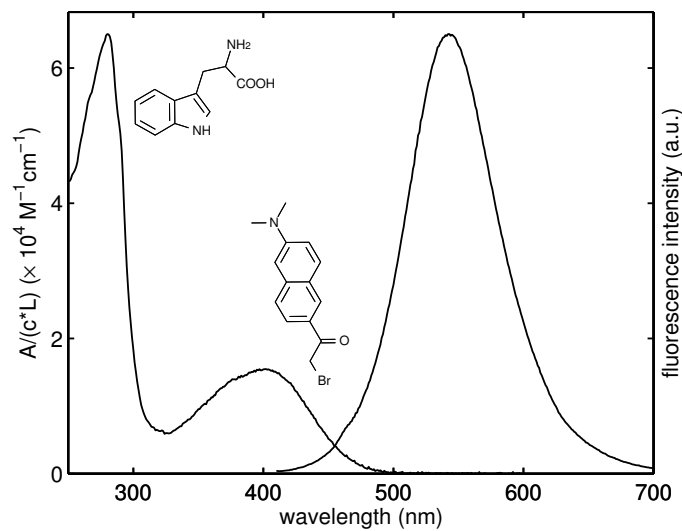


Figure 5.3: Absorption and fluorescence emission spectra of badan-GBP152C. Fluorescence spectrum was recorded using 400 nm excitation wavelength

5.3.1 Steady-state spectra

The absorption and fluorescence emission spectra of badan-GBP152C in phosphate buffered saline (PBS), pH 7.3, is shown in figure 5.3. There are two distinctive peaks in the absorption spectrum of badan-GBP152C. The peak at 400 nm is the first absorption peak of badan. The peak at 280 nm is assigned to absorption of tryptophan which is an intrinsic fluorophore in the GBP. Although the extinction coefficient of badan ($\sim 15,000 \text{ M}^{-1}\text{cm}^{-1}$) is higher than that of tryptophan ($\sim 5,600 \text{ M}^{-1}\text{cm}^{-1}$), the absorption of badan-GBP152C at Trp peak is clearly stronger than at badan peak. This is partly caused by the fact that GBP intrinsically contains 5 Trp residues – at positions 127, 133, 183, 195 and 284. In addition, tryptophans from unlabelled GBP entities present in the sample also contribute to the absorption at 280 nm. It is, in principle, possible to estimate the labelling efficiency from the proportions of the two peaks and known extinction coefficients of badan and tryptophan. However, one must have on mind that badan fluorophores can also bind non-specifically to the protein, i.e., they do not bind to the desired location but reside in other hydrophobic part of the folded protein.

The fluorescence emission spectrum of badan-GBP152C excited at 400 nm shows a peaks at 546 nm corresponding to badan emission (figure 5.3). When exciting at 280 nm (Trp peak absorption), the spectrum contains both badan and Trp (peak at 340 nm) fluorescence bands (data not shown). The changing amplitude proportion of the two emission peaks with changing excitation wavelength confirms that two different fluorescent species are present in the sample.

A strong increase of relative fluorescence emission intensity was observed with successive glucose addition until it reaches $\sim 400\%$ at saturation. Approximately 5 nm overall shift of the emission spectrum to shorter wavelengths (hypsochromic shift) was recorded. This is consistent with less polar environment of the fluorescent probe upon substrate (glucose) binding by the protein.

Figure 5.4 shows the temporal evolution of badan-GBP152C fluorescence intensity following after addition of glucose into the sample. The sample was excited at 400 nm and the fluorescence was monitored at 540 nm. The speed of the fluorescence intensity change reflects the time it takes for the new equilibrium to establish. From measured curves, it can be concluded that ~ 30 min period is needed for the sample to stabilise.

Several observations indicated that badan-GBP152C is not very photostable. If the sample was left in the dark for some time (~ 0.5 h) and several subsequent scans of fluorescence emission were performed, a decrease of the peak amplitude was clearly noticeable between the first and the second scan. Each following scan retraced the second scan, i.e., no further decrease was observed. Strangely, the same behaviour could be reproduced, once the sample was again left in the dark. This effect had to be considered during the fluorescence anisotropy measurements in which several scans with different arrangements of polarisers were recorded. The excitation light intensity was much higher when measuring steady-state spectra. During the time-resolved measurements, no indication of sample instability was observed – the recorded decays were verified to be fairly reproducible. Often rather extensive measurements were performed on a single sample (after each addition – measurements of absorption, fluorescence anisotropy scans, fluorescence decays recorded at several emission wavelengths,

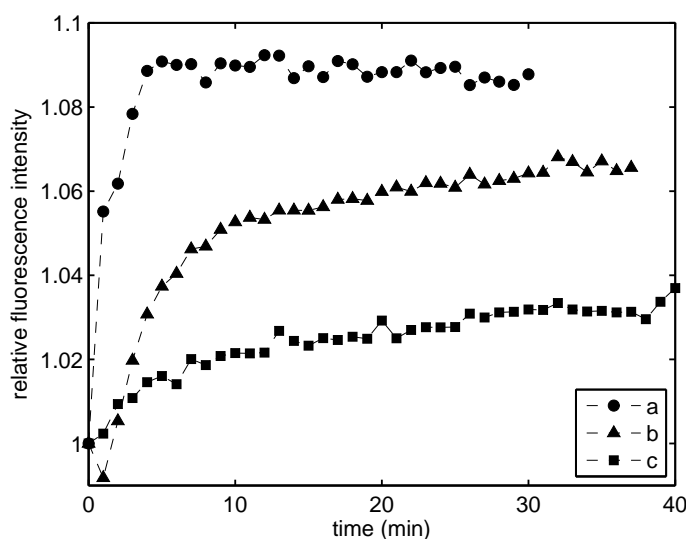


Figure 5.4: Fluorescence intensity evolution following after adding glucose to the sample. Concentration of glucose was successively increased from 0.04 to 0.41 μM (a), from 4.6 to 7.6 μM (b) and from 10.3 to 13.0 μM (c)

anisotropy decay measurements). The extended period during which the sample was irradiated by excitation light might have caused somewhat reduced overall increase of fluorescence intensity induced by glucose addition and therefore limit the reproducibility of the intensity (and possibly other) measurements.

The steady-state spectrum of badan-GBP152C recorded at 4.7 μL glucose concentration is shown in figure 5.5. The spectrum is quite constant in the region of fluorescence emission maximum. The faint fluorescence anisotropy peak around 450 nm is most probably caused by Raman scattering by water. The shape of the badan-GBP152C fluorescence anisotropy is independent of the glucose concentration. The anisotropy mean value shows a slight decrease with increasing glucose concentration – see figure 5.6. A decrease of fluorescence anisotropy would indicate that in the bound state i) either the rotation of the protein is faster due to more compact form or ii) the motion of the fluorescent probe is more restricted. However, the recorded decrease compared to the measurement precision is too small to be conclusive.

5.3.2 Time-resolved studies

Fluorescence intensity decay of badan-GBP152C was studied at different glucose concentrations. After glucose was added to the sample, decays were recorded at over 10 wavelength points covering the badan emission. The decay data were analysed by reconvolution using DAS6 (IBH) software. The fitted parameters of the recorded fluorescence decays are summarised in tables 5.3, 5.4, 5.5 and 5.6. Selected decay data are plotted in figure 5.7. The decay of fluorescence of badan-GBP152C is clearly wavelength-dependent. The multi-exponential

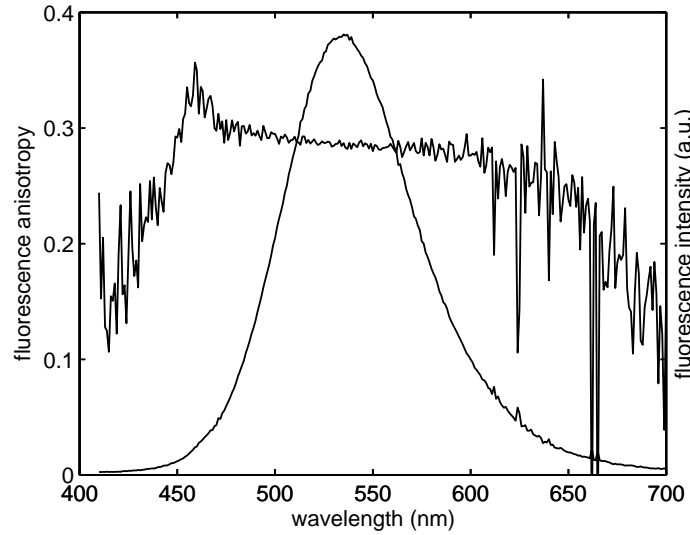


Figure 5.5: Spectrum of badan-GBP152C fluorescence anisotropy (emission scan). Excitation wavelength 400 nm, glucose concentration $4.7 \mu\text{M}$.

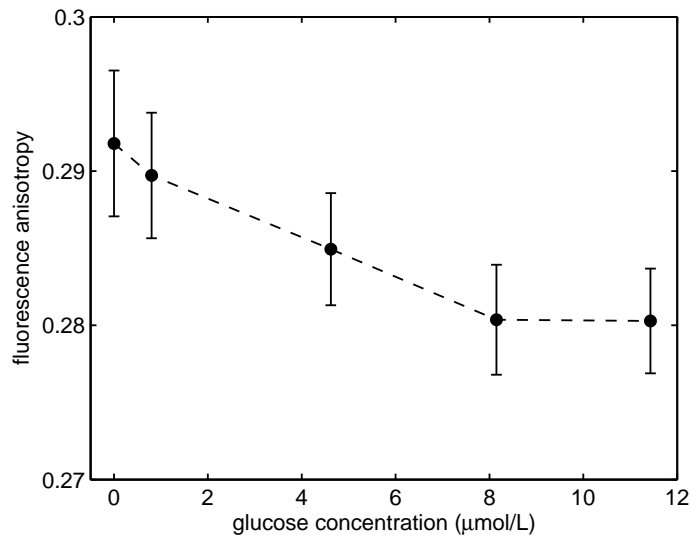


Figure 5.6: Dependence of mean fluorescence anisotropy on glucose concentration in the sample. The excitation wavelength was 400 nm emission fluorescence anisotropy was averaged over the range from 510 to 580 nm. Error bars indicate standard deviations from the mean value.

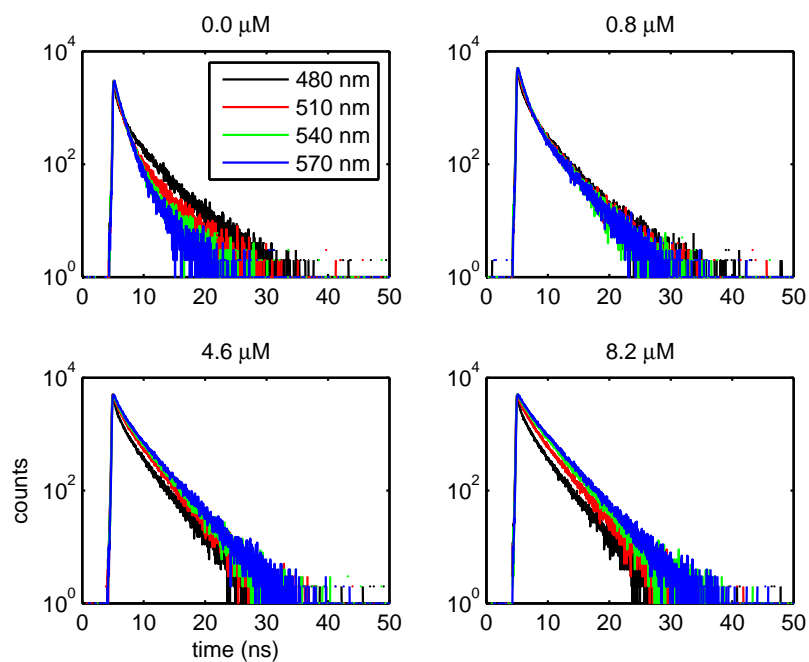


Figure 5.7: Recorded fluorescence decays of badan-GBP152C at different glucose concentration in the sample. The decays were recorded using a diode laser emitting at 400 nm. The monochromator bandwidth was set to 12 nm.

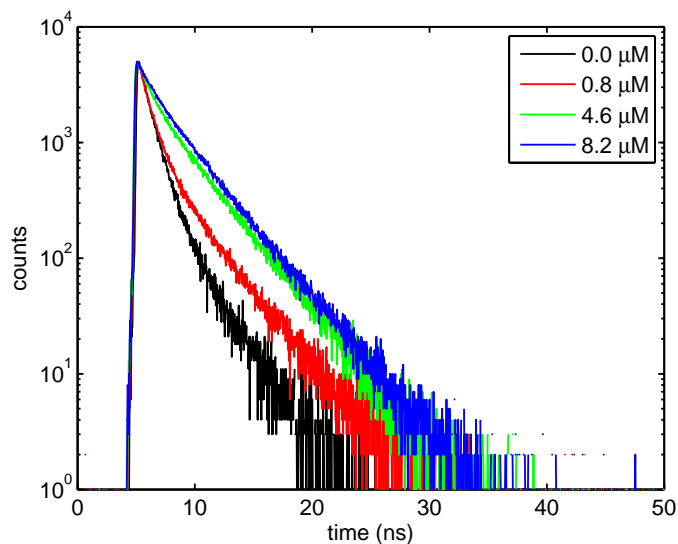


Figure 5.8: Comparison of badan-GBP152C fluorescence decays recorded at emission wavelength 550 nm at different concentration of glucose in the sample.

model function had to be used to obtain a good fit. With no glucose added to the sample, fluorescence decays longer at shorter emission wavelengths (top-left, figure 5.7), whereas at 8.2 μM glucose concentration, the decay times increases with wavelength (bottom-right). A kind of intermediate state can be recognised at 0.8 μM glucose concentration, where the decays recorded at all wavelengths are similar (top-right).

Recorded decays were fitted by reconvolution with DAS6 (IBH) software using multi-exponential kinetic model

$$I(t) = \sum_i \alpha_i e^{-\frac{t}{\tau_i}}.$$

Two- or three-exponential models were used, depending on which provided the best χ^2 . No parameter was fixed during the fitting procedure. At short-wavelength side of the emission, three exponentials were always needed to describe the recorded decays, whereas at long-wavelength side, the decays are less complicated (with exception of decays recorded at 0.8 μM glucose, where three exponentials had to be used at all wavelengths).

It should be pointed out that interpretation of individual components yielded from fitting by the multi-exponential kinetic model can be rather delicate. It is known that in certain cases, different combinations of α_i and τ_i can provide indistinguishable decays, even for decay with only two components (see an example on page 103 in [5]). Each parameter of the multi-exponential model can be varied within a certain range without any effect on the goodness of the fit – if other parameters can compensate for the change. In other words, parameters α_i and τ_i are correlated. This is particularly true when the lifetimes are close in magnitude (such as, for example, 6 and 8 ns). Therefore, it is possible that different combination of parameters than those listed in tables 5.4 – 5.6 can describe the recorded decays equally well and the presented values are “pre-determined” to a certain extent by the arbitrary initial guess of the fitting.

In general, a wavelength-dependent fluorescence decay can be a result of several phenomena and their combinations. For instance, it can be caused by the presence of two or more populations with different lifetimes and emission bands shifted with respect to each other. This can be expected in the case of badan-GBP152C – when the protein is bound to glucose, the badan intensity decay is longer and its emission is slightly blue-shifted with respect to the unbound form.

Another important effect related to fluorescence of badan and similar fluorophores is spectral relaxation, i.e., the shift of emission spectral band to longer wavelength within the fluorescence lifetime. The fluorophore undergoes a charge redistribution upon excitation and surrounding solvent molecules (in the case of dye dissolved in a liquid) start to reorient in order to establish a new equilibrium. This is referred to as *solvent relaxation*. It happens on a ~ 10 ps time scale in low viscosity solvents, i.e., much faster than what can be resolved with a common TCSPC experiment. When the speed of solvent relaxation is of the same order as the spontaneous emission, fluorescence occurs from partially relaxed state. The movement of, for instance, water molecules at a surface of a protein or inside the hydrophobic region of a membrane (often referred to as “bound” or “biological” water) can be slowed down sufficiently to be studied by an analysis of time-resolved emission spectra recorded by TCSPC [34, 111].

Since it was first introduced, prodan and its derivatives have been widely used as a fluorescent probes in research of proteins, lipids and cellular membranes [112–115]. Photophysical properties of prodan itself has been subject to numerous studies, both experimental and theoretical. The fluorophore moieties in the structure of prodan and badan are identical and their photophysical behaviour can be expected to be very similar. The great sensitivity of these dyes are based on the internal charge transfer from the electron donor group to the electron acceptor group. The character of the charge transfer is strongly influenced by the environment of the fluorophore. In a non-polar environment, the emission occurs from a locally excited state (i.e., the initially excited state) while in polar solvent the emission occurs from a charge transfer state in either planar or twisted conformation [116, 117]. The conformational change between the two charge transfer states can also contribute to fluorescence relaxation [113].

The situation is more complicated by the possibility of non-specific labelling. When the mutant protein is being labelled with badan, most fluorophores link to cystein by a chemical reaction. However, a small fraction of the dye can attach to the protein non-covalently and reside on a different location on the surface of the protein. The environment of such fluorophore can be more hydrophobic than that of the dye located at the desired position. At zero glucose concentration, a ~ 4 ns decay component is observed at the short wavelength side of the emission spectrum (τ_3 in table 5.3 and figure 5.8, top-left). Its relative contribution to the overall fluorescence is decreasing with wavelength. This component can be assigned to non-specifically located fluorophores located in a less polar environment and thus having blue-shifted emission.

The spectral relaxation, on the other hand, is manifested by shorter decay times at shorter wavelengths – the fluorophores observed at short emission wavelength are de-excited by both spontaneous emission and relaxation – as can be observed at 8.2 μM glucose concentration (figure 5.8, bottom-right).

Figure 5.9 shows the comparison of the relative fluorescence intensity and the relative average fluorescence lifetime recorded for different concentrations of glucose at 550 nm emission wavelength. The average lifetime, for a multi-exponential decay defined by equation 4.2, is proportional to the area beneath the decay curve and its relative change thus reflects the change of the quantum yield. The glucose-induced change of the relative average fluorescence lifetime is smaller than that of the steady-state intensity, i.e., the change in the lifetime does not fully cover the increase of the steady-state intensity. In a quenching experiment, this would indicate presence of static quenching. In this case, however, an increase of molar absorption coefficient might occur when the environment of the fluorescent probe changes to less polar. (For example, prodan, a dye very similar to badan, has molar absorption coefficient 14,500 $\text{M}^{-1}\text{cm}^{-1}$ in an aqueous solution and 18,400 $\text{M}^{-1}\text{cm}^{-1}$ in less polar ethanol.) This would cause the intensity increase to be higher than that of the quantum yield. Unfortunately, the change in the absorbance of the sample was not verified because the use of micro-cuvette did not allow reliable absorption measurements.

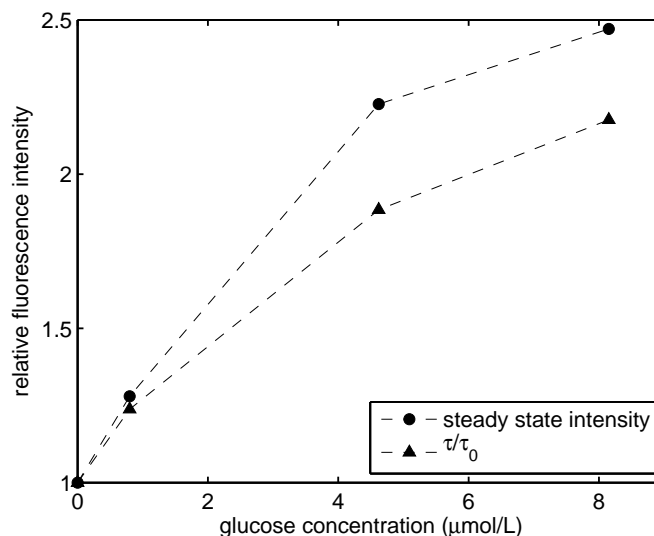


Figure 5.9: Comparison of the relative fluorescence intensity dependence on glucose concentration based on steady-state and time-resolved measurements. The monitored emission wavelength was 550 nm.

gluc. conc. (μM)	r_0	θ_1 (ns)	β_1	θ_2 (ns)	β_2	χ^2	d (nm)
0	0.34	0.12	0.08	27.50	0.26	1.05	5.96
0.8	0.39	0.06	0.12	24.22	0.27	1.05	5.72
4.7	0.37	0.06	0.10	18.73	0.27	1.07	5.25
8.2	0.30	0.19	0.04	17.23	0.26	1.07	5.10

Table 5.2: Fitted anisotropy decay parameters and a hydrodynamic diameter d corresponding to θ_2 ; $\beta_1 + \beta_2 = r_0$

Time-resolved anisotropy

The decays of badan-GBP152C fluorescence anisotropy recorded at four different glucose concentrations are shown in figure 5.10. Good anisotropy fits were obtained using two-exponential model,

$$r(t) = \beta_1 \exp\left(-\frac{t}{\theta_1}\right) + \beta_2 \exp\left(-\frac{t}{\theta_2}\right),$$

The fitted parameters are listed in table 5.2. All parameters were left free during the fitting procedure. The longer correlation time corresponds to global protein rotation. The shorter component can be assigned to relatively a fast “wobbling” motion of the fluorescent label. The fitted values of both correlation times indicate that the real values lie outside the interval in which the fluorescence anisotropy decay measurement is reliable. The values of the fast component, θ_1 , are approaching the limit that can be resolved by the used experimental technique. The values of the second component, θ_2 , corresponding to the slow rotation of the protein are substantially larger than the fluorescence

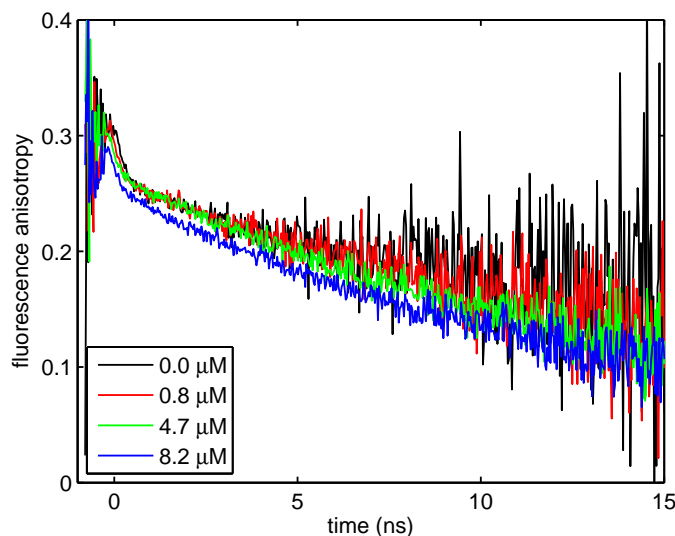


Figure 5.10: Recorded decays of badan-GBP152C fluorescence anisotropy at different glucose concentrations. Excitation wavelength 400 nm, emission wavelength 560 nm, monochromator bandwidth 16 nm.

decay time of badan-GBP152C, which somewhat reduces the reliability of the recovered values. The fitted values of θ_1 are smaller than 200 ps, which is similar to the FWHM of the instrument response function recorded with the same set-up. Therefore, we can not expect to be able to recover subtle changes in that parameter by the used experimental method. It is not surprising that the fitted values of θ_1 differ quite a lot from each other (in their relative value), showing no trend. However, it can be concluded from the shape of the recorded fluorescence anisotropy decays that the contribution from the fast component to the total depolarisation remains more or less constant, independently of the glucose concentration. That would mean that there is no substantial change in the restriction of the probe's fast movement. The long correlation time, θ_2 , changes from 28 ns at 0 glucose concentration to 17 ns at 8.4 μM glucose. Although absolute values of θ_2 are not very reliable for the reason mentioned above, the decrease would correspond to a faster rotation of the protein in the bound state compared to the open state. In other words, upon binding a molecule of glucose, the protein changes its geometry to a more compact shape. Values of the hydrodynamic diameter d also listed in table 5.2 were calculated from θ_2 using formula 2.27 for Brownian rotation, i.e.,

$$d = \sqrt[3]{\frac{6k_B T \theta_2}{\pi \eta}}.$$

The viscosity $\eta = 1.003 \times 10^{-3}$ Pa s of water at 20.0 °C was considered. Formula 2.27 is only an estimate of the protein size and the specific interaction of the surface with surrounding solvent molecules is not considered. The glucose-induced conformational change can cause different side chains to be exposed

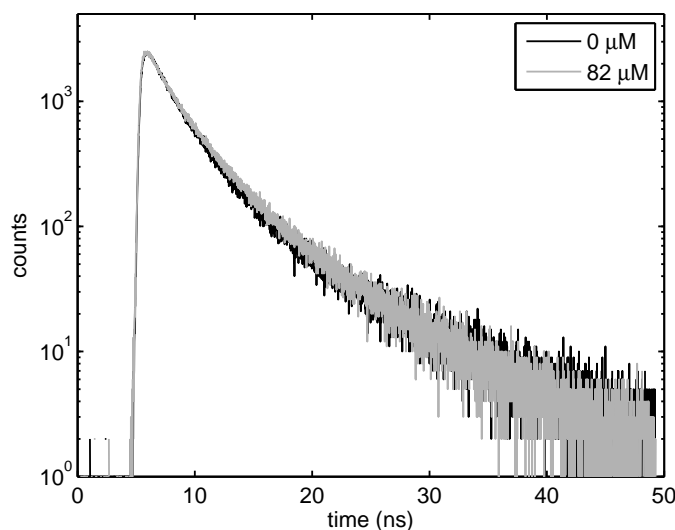


Figure 5.11: Comparison of badan-GBP152C fluorescence decay recorded at 0 and 82 μM glucose concentration. A light emitting diode with emission maximum at ~ 280 nm was used for excitation, excitation wavelength 296 nm was selected by the monochromator, the emission monochromator was set to 350 nm (tryptophan fluorescence) with 12 nm bandwidth

to water and thus binding of glucose can affect the badan-GBP152C rotation through surface-water interaction. Nevertheless, values of d are comparable to crystal unit-cell dimensions. Lattice parameters determined by high-resolution X-ray diffraction are $a = 61.26 \text{ \AA}$, $b = 36.58 \text{ \AA}$, $c = 64.94 \text{ \AA}$ and $\alpha = 90.00^\circ$, $\beta = 107.19^\circ$, $\gamma = 90.00^\circ$ (from <http://www.pdb.org>, doi:10.2210/pdb2hph/pdb). These parameters were recorded with GBP bound to glucose.

As was already mentioned, the decrease of θ_2 indicates faster rotation of badan-GBP152C in the bound state. However, it should be pointed out that below saturation both bound and unbound forms of the protein contribute to overall fluorescence from the sample. The decrease of θ_2 is caused by increasing dominance of the contribution from bound proteins which have higher quantum yield and more compact shape. The highest glucose concentration used in the time-resolved anisotropy measurements (8.4 μM) is still below saturation. Therefore, further decrease of θ_2 can be expected.

Fluorescence kinetics of tryptophan residues

Fluorescence decays of the emission band corresponding to tryptophan fluorescence were recorded in absence and excess of glucose. Both the wild-type and the mutated form of GBP contain 5 tryptophan residues. One of the tryptophan residues – at position 183 – is located quite close to badan. There is a possibility of some interaction between them, e.g., resonance energy transfer due to an overlap of tryptophan emission and badan absorption. A strong in-

teraction would affect the decay of tryptophan fluorescence. The comparison of recorded decays is shown in figure 5.11. The decay kinetics is non-exponential and does not change with glucose addition. Therefore, it can be concluded that the glucose-induced change of the protein's shape does not affect the interaction (if there is any) between tryptophan and badan.

The utilisation of intrinsic fluorescence of GBP to estimate the protein size via time-resolved anisotropy, as was demonstrated with badan, is complicated by the high number of tryptophan residues in the protein. It is known that tryptophan at different locations within the same protein can have dissimilar motions and associated anisotropy decay [5]. The anisotropy decay of tryptophan fluorescence of GBP is therefore expected to be probably too complex to interpret. The measurement of tryptophan fluorescence depolarisation was not attempted because material of polarisers used in the measuring apparatus does not allow to work with wavelengths $\lesssim 350$ nm.

λ_{em} (nm)	τ_1 (ns)	τ_2 (ns)	τ_3 (ns)	a_1 (%)	a_2 (%)	a_3 (%)	χ^2
450	0.1	1.2	3.9	10.0	29.1	60.9	1.16
480	0.1	0.9	3.7	12.1	32.9	55.0	1.03
490	0.1	0.9	3.7	12.1	41.3	46.6	1.12
490	0.1	0.9	3.6	11.6	41.6	46.7	1.09
500	0.1	0.9	3.6	11.2	51.9	36.8	0.97
510	0.2	0.9	3.3	11.5	56.8	31.7	1.02
520	-	0.8	2.8	0	64.3	35.7	1.09
530	-	0.8	2.5	0	66.4	33.6	1.12
540	-	0.8	2.4	0	67.4	32.6	1.18
550	-	0.8	2.3	0	69.0	31.0	1.09
560	-	0.8	2.2	0	69.5	30.5	1.07
570	-	0.8	2.1	0	68.2	31.8	1.22
580	-	0.8	2.1	0	67.6	32.4	1.3
590	-	0.8	2.1	0	69.4	30.6	1.36
600	-	0.8	2.2	0	70.7	29.3	1.38
610	-	0.8	2.1	0	70.2	29.8	1.35

Table 5.3: Glucose concentration 0 μ M

λ_{em} (nm)	τ_1 (ns)	τ_2 (ns)	τ_3 (ns)	a_1 (%)	a_2 (%)	a_3 (%)	χ^2
480	0.1	0.8	3.3	30.6	12.6	56.8	1.27
490	0.1	0.9	3.4	36.0	11.3	52.7	1.24
500	0.1	0.8	3.3	38.7	10.1	51.2	1.25
510	0.1	0.8	3.2	41.5	8.7	49.8	1.37
520	0.0	0.8	3.2	45.2	7.6	47.2	1.06
530	0.3	1.0	3.3	49.4	8.1	42.5	1.06
540	0.3	1.0	3.3	49.9	7.7	42.4	1.09
550	0.2	0.9	3.3	53.4	4.3	42.3	1.15
560	0.3	1.0	3.4	53.9	6.6	39.5	1.03
570	0.6	1.2	3.5	38.4	25.6	36.0	1.11
580	0.5	1.1	3.5	47.7	15.8	36.5	1.03
590	0.5	1.1	3.4	49.0	14.6	36.4	1.12
600	0.6	1.3	3.6	38.7	29.6	31.7	1.13
610	0.5	1.1	3.5	51.3	13.6	35.1	1.10

Table 5.4: Glucose concentration 0.8 μ M

λ_{em} (nm)	τ_1 (ns)	τ_2 (ns)	τ_3 (ns)	a_1 (%)	a_2 (%)	a_3 (%)	χ^2
470	0.1	0.8	3.1	13.4	26.2	60.4	1.13
480	0.1	0.9	3.2	10.0	27.0	63.0	1.21
490	0.2	1.3	3.2	10.5	28.9	60.6	1.39
500	0.3	1.4	3.3	11.1	25.6	63.3	0.99
510	0.2	1.0	3.2	5.2	22.4	72.4	0.92
520	0.4	1.4	3.4	7.3	26.1	66.6	1.01
530	-	0.8	3.2	0	21.6	78.4	1.09
540	-	0.8	3.3	0	20.5	79.5	1.14
550	-	0.9	3.4	0	21.9	78.1	1.06
560	-	0.9	3.4	0	20.8	79.2	1.05
570	-	0.9	3.4	0	21.4	78.6	1.10
580	-	0.8	3.4	0	20.8	79.2	1.11
590	-	0.9	3.5	0	22.7	77.3	1.04
600	-	0.8	3.5	0	22.0	78.0	1.03
610	-	0.9	3.5	0	22.8	77.2	1.18

Table 5.5: Glucose concentration 4.62 μM

λ_{em} (nm)	τ_1 (ns)	τ_2 (ns)	τ_3 (ns)	a_1 (%)	a_2 (%)	a_3 (%)	χ^2
460	0.1	1.0	3.2	15.0	30.3	54.7	1.04
470	0.1	0.8	3.0	13.1	25.7	61.2	1.11
480	0.1	1.0	3.1	10.4	25.4	64.2	1.03
490	0.2	1.1	3.2	8.0	24.5	67.5	1.03
500	0.2	1.2	3.2	6.2	23.0	70.8	0.99
510	0.2	1.2	3.3	4.3	21.5	74.2	1.03
520	0.3	1.3	3.3	4.3	18.6	77.1	1.00
530	0.2	1.2	3.4	1.9	18.4	79.7	1.07
540	0.4	1.6	3.5	4.4	18.5	77.1	1.09
550	0.1	1.2	3.5	1.6	15.4	83.0	0.98
560	-	1.0	3.5	0	13.8	86.2	1.02
570	-	1.0	3.5	0	14.1	85.9	1.08
580	-	1.0	3.6	0	14.4	85.6	1.08
590	-	0.9	3.5	0	12.5	87.5	1.05
600	-	1.0	3.6	0	13.0	87.0	1.18
610	-	1.0	3.6	0	13.0	87.0	1.14

Table 5.6: Glucose concentration 8.15 μM

Chapter 6

Single molecule detection

6.1 Introduction

Single molecule fluorescence spectroscopy is an extremely sensitive analytical method. Spectroscopic study of a single molecular entity gives an opportunity to observe behaviour which is otherwise “obscured” by averaging over a large ensemble of copies of the molecule, e.g., single molecule fluorescence blinking or spectral fluctuations. Thanks to recent advances in the instrumentation of visible light microscopy, microscope systems are available on the market, that have sufficient sensitivity to detect fluorescence of a single molecule with an adequate signal-to-noise ratio.

Experiments presented in this chapter were performed in order to test the applicability of α -SNOM (WITec GmbH, Germany), described in section 3.1.3, for single molecule fluorescence imaging and spectroscopy. Some time after the microscope was installed, it was upgraded to allow confocal Raman microscopy. When equipped with a spectrograph, the microscope can also record a fluorescence emission spectrum for each point of an image. It was not clear, however, whether the detection sensitivity of the system is high enough, so that a single molecule spectrum can be successfully measured.

The secondary aim of the “pioneering” work presented here was to adopt single molecule spectroscopy for future research in the Photophysics group – to get hands-on experience with the technique, sample preparation issues, and to learn the limits for possible applications. Because of the possibility to avoid ensemble averaging, single molecule spectroscopy is believed to become a routine technique, complementary to conventional “bulk” molecular spectroscopy methods.

6.2 Experimental results

In order to test the possibility of using α -SNOM for single molecule imaging, a well defined sample is needed with the simplest possible preparation protocol. Rhodamine 6G (Rh6G) or rhodamine B (RhB) adsorbed on a glass surface at low concentration was chosen to serve as a standard reference system. A protective polymer layer can be also applied to reduce photobleaching of fluorophores.

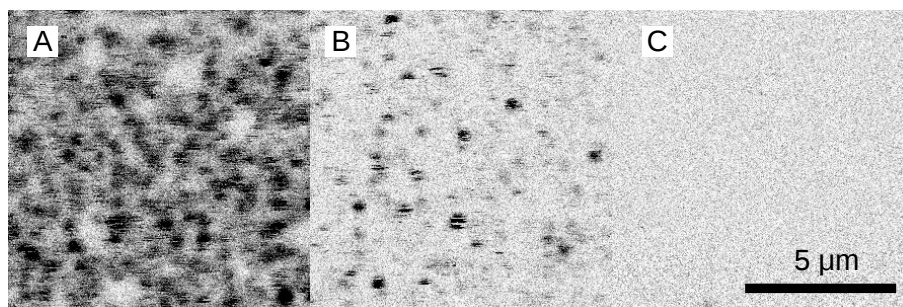


Figure 6.1: Comparison of fluorescence from untreated microscope slide (a), slide washed in methanol (b) and slide treated by “piranha” etching solution (c).

Rh6G and RhB dyes are obvious choices thanks to their high quantum yield and photostability that also makes them popular laser dyes. Both dyes can be efficiently excited with 532 nm wavelength used in the microscope. The use of RhB brings a slight advantage over Rh6G because the short wavelength side of the emission spectrum of Rh6G partially overlaps the cut-off wavelength of the holographic edge filter, hence a fraction of fluorescence is filtered out with reflected excitation light. Both absorption and emission spectrum of RhB is shifted to longer wavelengths with respect to Rh6G.

Note

Fluorescence images in this chapter are presented in greyscale. White color means the lowest fluorescence intensity, black represents the highest intensity. If two fluorescence images are compared to each other (such as in figure 6.6), the conditions during the data acquisition (alignment of the instrument, excitation power, etc.), as well as the color scale, are the same.

To avoid confusion, the term *pixel* is used here for a point of an intensity raster image, not for an element in a CCD camera array. The CCD was used here only for recording spectra, not imaging.

6.2.1 Sample preparation and impurity issues

Several sample preparation protocols have been tested. The most reliable and reproducible way was to deposit a solution of a dye in methanol onto a surface of a clean microscope cover slip and leave the solvent to evaporate. The cover slip was then spin-coated with poly(methyl methacrylate) dissolved in dimethyl carbonate. Typically, 3 – 5 μL of ~ 1 nM (10^{-9} mol dm⁻³ concentration) solution of the dye in a spectrophotometric grade methanol was deposited and 150 μL of 25 mg/100 mL PMMA solution in dimethyl carbonate was used for spin-coating. Alternatively, the cover slip could be spin-coated with a solution of both the dye and PMMA.

Due to the ultimate sensitivity of single molecule detection, even a minor impurity can result in corrupted data. Contamination of used chemicals, pipettes, and the substrate with unwanted fluorescent material must be avoided. Figure

6.1 illustrates the importance of substrate cleaning. As can be revealed by scanning the surface without any dye applied, an out-of-the-box microscope slide, although apparently clean, contains quite large amount of fluorescent contamination (a) which can not be fully removed by sonicating the slide in spectrophotometric grade methanol (b). Therefore, more drastic methods of substrate cleaning were employed.

A reliable method to remove any organic material from the substrate is the treatment with the so-called “piranha” solution – a mixture of concentrated sulphuric acid (H_2SO_4) and hydrogen peroxide (H_2O_2). This mixture is a strong oxidiser and will remove most of organic matter from the glass surface. It will also hydroxylate the surface, i.e., increase the number of silanol groups, which will leave the surface hydrophilic. Figure 6.1 (c) shows that no fluorescence was detected from glass cover slip treated with 7:3 mixture of 98% H_2SO_4 and 30% H_2O_2 . The hydrophilicity of the surface is also a positive feature regarding the dye deposition and spin-coating. However, using “piranha” solution is discouraged because of accompanying safety issues. Mixing the solution is an exothermic reaction and can be rather violent. There is even a risk of explosion when a larger quantity of organic solvent is added to the solution.

Alternatively, the glass cover slips could be immersed in a concentrated (~ 5 wt%) methanol or ethanol solution of potassium hydroxide (KOH) for 24 hours and than washed with deionized water. This method also gives sufficient substrate purity and is far less dangerous compared to cleaning with the piranha solution.

For imaging of single molecules dispersed on a surface, the distance between individual molecules must be obviously larger than is the optical resolution of the microscope. It is difficult to estimate the resulting surface concentration of fluorophores from the known initial concentration of the deposited solution. Fluorophores are often inhomogeneously distributed on the surface, due to the progress of solvent evaporation. The dye can be also partly washed away when the polymer layer is applied by spin-coating. The suitable concentration was therefore found by preparing a set of sample with different initial concentrations, $\sim 10^{-7}$, 10^{-8} , 10^{-9} mol dm $^{-3}$, etc., and examining their fluorescence images. At high initial concentration, the images of individual fluorophores overlap and the fluorescence signal is spatially continuous (although often not homogeneous). For a sufficiently low concentration, individual fluorescence spots can be observed.

6.2.2 Single molecule imaging

The most convenient arrangement for recording single molecule images with α -SNOM (see section 3.1.3 for the description) is the reflection confocal mode of operation. The microscope can also be used in SNOM mode with a special microfabricated cantilever [44]. SNOM would in principle allow single-molecule imaging with superior spatial resolution [120]. However the alignment of the instrument for SNOM measurements is considerably more complex and time consuming than for confocal microscopy. Moreover, the cantilever used in α -SNOM is a rather expensive consumable. Nevertheless, the confocal mode of operation offered satisfactory performance for imaging of single molecules and far less complicated alignment procedure was needed.

Parameters of a scan – the excitation power, the integration time per pixel and the pixel size – must be chosen carefully. Any unfavourable change in those parameters makes imaging of single molecules impossible. For a successful detection of a single fluorophore, the signal S must be comparable to fluctuations in S , the background signal B and the dark noise N . Under the assumption of Poisson statistics of fluctuations, the fluorescence signal-to-noise ratio is [4, 5]

$$\text{SNR} = \frac{S}{\sqrt{S + B + N}}$$

For example, if the excitation intensity is too small (at a given pixel integration time), the fluctuations in N simply obscure the fluorescence signal. If the power is too high, the increased contribution of the background signal B (autofluorescence of the sample, Rayleigh- or Raman-scattered light) also reduce the SNR. Furthermore, at high excitation rates, fluorophores often photobleach within the observation period and after that only B and N are detected. An excitation rate allowing adequate SNR should therefore be selected and, in order to detect as many photons as possible without affecting SNR, the observation period of a single molecule should roughly match the time the fluorophore can emit before it is destroyed.

Photobleaching happens when the structure of the fluorophore is irreversibly modified due to a photo-induced chemical reaction with another molecule. This reaction proceeds more easily in the excited state than in the ground state. The photostability of a dye can be quantified by the *quantum yield for photobleaching*, Φ_B , which is defined as [121, 122]

$$\Phi_B = \frac{\text{number of photobleached fluorophores}}{\text{total number of absorbed photons}}$$

An inverted value of Φ_B gives an average number of excitation–relaxation cycles that a fluorophore can undergo prior to its irreversible photodestruction. The value of Φ_B depends strongly on the molecular structure of the fluorophore and its local environment (such as the concentration and mobility of oxygen [123]) as well as the excitation power [121, 124]. For rhodamines, it is estimated to be in the order of $\sim 10^{-6} - 10^{-7}$ for irradiances below 10^3 W cm^{-2} [121]. The probability for photobleaching can be used for estimation of the mean “survival” time of a Rh6G fluorophore at given illumination conditions. On average, a fluorophore is destroyed after

$$t_b = \frac{1}{\Phi_B} \frac{Ah\nu}{\sigma_A P_0}, \quad (6.1)$$

where P_0 is the power of the excitation light, A the beam area, ν the excitation light frequency, and σ_A is the absorption cross-section of the fluorophore. (The expression $(\sigma_A P_0)/(Ah\nu)$ gives the number of absorbed photons per unit time.) If $\Phi_B = 8.9 \times 10^{-6}$ [5], $A = 7.9 \times 10^{-9} \text{ cm}^2$ ($1 \mu\text{m}$ beam diameter), $\nu = 5.7 \times 10^{14} \text{ Hz}$ (i.e. 530 nm wavelength), $\sigma_A = 4.43 \times 10^{-16} \text{ cm}^2$ (for Rh6G in water at $\lambda = 530 \text{ nm}$), and $P_0 = 10 \mu\text{W}$, the fluorophore can be detected for $\sim 0.1 \text{ s}$ before it is destroyed. This estimate is, of course, only illustrative, however, it can serve as a basis for definition of optimal scan parameters.

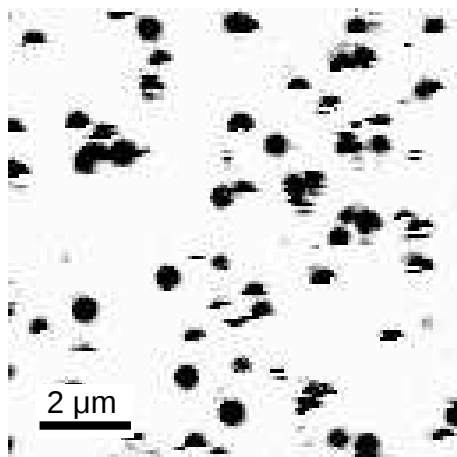


Figure 6.2: Fluorescence image of RhB molecules dispersed on a glass surface

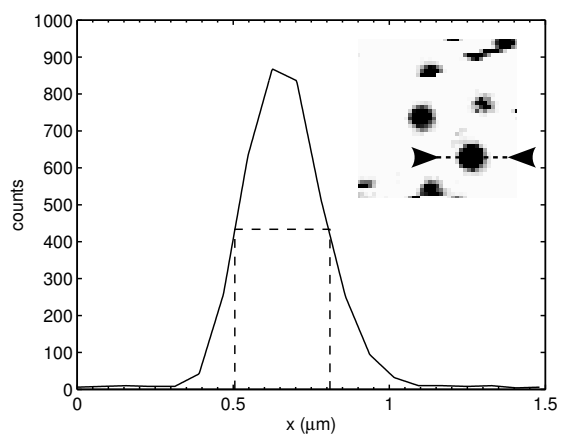


Figure 6.3: Intensity cross-section of fluorescence image of RhB dispersed on a glass surface

Figure 6.2 shows a typical fluorescence image of Rhodamine B (RhB) molecules adsorbed on a glass surface. The sample was prepared by deposition of 5 μL of 0.5×10^{-9} mol dm^{-3} RhB solution in methanol. The sample was left for approx. 20 min to evaporate the solvent. No protective polymer layer was applied. The resolution of the image is 128×128 pixels and the size of the scanned area was 10×10 μm , which results in 78×78 nm pixel size. The integration time per pixel was 5 ms, so the image acquisition time was 1:22 min. The power of the excitation laser was set to ≈ 10 μW . The image was recorded with the collection multi-mode fibre coupled directly to the APD. It is possible to record an image with a higher resolution, but the scan parameters must be adjusted accordingly. The fluorescence signal rate from areas in between the spots is ~ 10 counts per pixel, which is of the same order as was recorded at the same instrumental conditions from a clean substrate.

In the chosen colour representation (see the note on page 87), molecule images appear as dark spots on the light background. Images of unbleached molecules are circular spots with a size given by the diffraction-limited resolution of the microscope objective. An example of the count rate along the scanning line crossing the maximum of one of the spots, i.e., intensity cross-section, is shown in figure 6.3. It has full width at half maximum (FWHM) ~ 0.35 μm which is in a good agreement with Rayleigh's criterion. According to that, diffraction limited resolution of the used NCG (no cover glass) microscope objective with numerical aperture $N.A. = 0.9$ working at $\lambda = 532$ nm wavelength is

$$\Delta \approx 0.61 \frac{\lambda}{N.A.} = 361 \text{ nm}$$

The images of individual molecules are not equal in their intensity. This is believed to be caused by different orientation of the molecule transition dipole moment in respect to the polarization of the excitation light [5]. The most intense spots in the image are composed of $\sim 10^4$ counts in total.

Photobleaching of a fluorophore during the image acquisition results in its disappearance on subsequent scans. Since the images are acquired by raster scanning, a bleached fluorophore appears as half circle or, more precisely, a circular segment in the fluorescence image. Unlike in the case of macroscopic objects (e.g. cells) labelled with a large number of fluorophores, where photobleaching is manifested as gradual fading of the fluorescence image with exposure time, the photobleaching of a single fluorophore occurs as a sudden drop of fluorescence intensity to the background value.

Some molecules display blinking, i.e. the single molecule fluorescence is switching on and off during the observation time, which is thought to be caused by intersystem crossing to a metastable dark state. Some molecules remain in the dark state for a long period, so that whole lines of their image are missing. A molecule image then appears to be horizontally "striped". The blinking behaviour is a consequence of an interaction of the fluorophore with its immediate environment. Since the blinking and bleaching is observed only for some molecules in figure 6.2, it appears that the local environment is not the same for all molecules on the glass substrate.

Larger fluorescence spots with irregular shape can be assigned to a few fluorophores located close to each other so that their images partially overlap. The occurrence of these clusters is smaller when the amount of the deposited dye is decreased.

In summary – fluorescence spots have a circular symmetry and their size corresponds to the resolution of the objective. The density of the spots depends on the amount of the deposited dye. Bleaching and blinking of some molecules is observed and the signal rate from in between the fluorescence spots is the same as from “blank” substrate. All these characteristics of recorded fluorescence images indicate that single molecules can be successfully detected and imaged with the instrument.

6.2.3 Single molecule spectra

When equipped with a spectrograph, α -SNOM allows recording of a complete spectrum at each pixel. The alignment of the instrument for spectral imaging is similar to that used for single molecule imaging (i.e., the microscope operating in confocal microscopy mode in reflection), only the output multi-mode fibre is coupled to a spectrograph.

As was already hinted in the previous section, truly every photon is valuable in single molecule imaging and spectroscopy. The ensemble steady-state emission spectra presented in this thesis are typically composed of $\sim 10^7$ counts. A rhodamine fluorophore usually emits $10^5 - 10^6$ photons in a single molecule experiment before it is destroyed due to photobleaching. The number of detected photons from a single molecule is further reduced by the limited detection efficiency which is estimated to be 5% or even less. Therefore, one can not expect to record a smooth high-resolution spectrum from one molecule. The single molecule spectrum, if it can be recorded at all, will most probably be constructed from sparse data.

To record an emission spectrum, a dispersive element – diffraction grating – must be inserted in the detection path. Unlike in the case of imaging, where one-channel detector (APD) is used, the fluorescence is divided between many detectors – pixels in the CCD array. Thus, the signal rate on each detector of the array is reduced. There are also additional optical losses inside the monochromator. The spatial, spectral, and time resolution of the experiment must be compromised in order to maximise the number of photons detected in each channel (wavelength).

There are three gratings with different dispersion mounted on a turret inside the monochromator. The grating giving the smallest dispersion was chosen (150 grooves/mm), so that the emission is projected on the smallest possible area of the CCD array. The resolution image should be high enough to resolve individual molecules, but a spot corresponding to one molecule should be covered by the smallest number of pixels (ultimately one molecule = one pixel). A longer pixel integration time allows more photons to be detected from one molecule. On the other hand, it should not exceed substantially the photobleaching time of an illuminated fluorophore, otherwise the SNR would be reduced due to fluctuations in the dark noise and the background signal, and the image total acquisition time would be unnecessarily long.

Figure 6.4 shows an image of fluorescence of RhB adsorbed on a glass surface recorded with the spectrograph (left pane). Spectrum from each pixel was taken during the scan. A software filter was applied on the spectral data, so that the intensity image shows the total signal detected only in the region of RhB emission (540 – 650 nm).

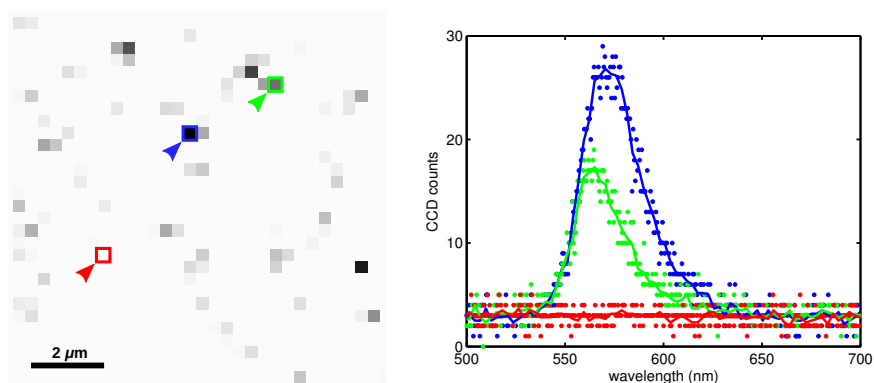


Figure 6.4: Integral intensity image. Rhodamine B molecules adsorbed on the surface of a microscope slide (**left**). The spectra were recorded from different pixels of the image as indicated by colour (**right**).

The image scan area was $10 \times 10 \mu\text{m}$ with resolution only 32×32 pixels. The pixel integration time was 1 s, thus the total image acquisition time was 17:04 minutes. One pixel then corresponds to the sample area of $313 \times 313 \text{ nm}$. With picture of this resolution, the circular symmetry of fluorescence spots can hardly be verified. However, the image was recorded with the same sample that was used for recording image 6.2. Several high-resolution fluorescence intensity images recorded with the sample using APD indicated that single molecules can be detected on different areas of the sample and that the surface density of fluorophores is fairly homogeneous. Therefore, it is highly probable that a spectrum recorded from one pixel of $0.3 \times 0.3 \mu\text{m}$ size is from a single molecule. In addition, since the resolution of the instrument is roughly matching the pixel size, fluorescence from a single molecule is focused in only 1 – 4 pixels.

Examples of spectra taken at different positions of the sample are shown in the right pane in figure 6.4. Although the y -axis is labelled as “CCD counts”, the signal in each channel (wavelength) is, in fact, only proportional to the number of incident photons. This is because CCD is not a photon-counting detector, but it is an integrating detector. Here the notation from the microscope control software ScanCtrl Spectroscopy Plus (WITec) is adhered to. The pixels in the intensity image corresponding to the spectra are indicated by respective colours. As can be noticed from figure 6.4, the spectra of individual RhB molecules differ not only in their amplitude but also in their spectral position. This also indicates that the local environment of individual fluorophores is not homogeneous, together with the fact that only some fluorophores display the blinking behaviour, as was described in the previous section.

The fluorescence spectrum shown in figure 6.5 (solid curve) was obtained by averaging the spectra from all pixels of the image. The emission spectrum of RhB in methanol is shown for comparison (dashed). A strong sharp peak at 532 originates in the scattered/reflected excitation laser light. A holographic edge filter together with a dichroic beam splitter are used to separate the excitation light from the collected fluorescence. The peak can not be observed in any individual spectrum (see the right pane in figure 6.4), but when all $32 \times 32 = 1024$

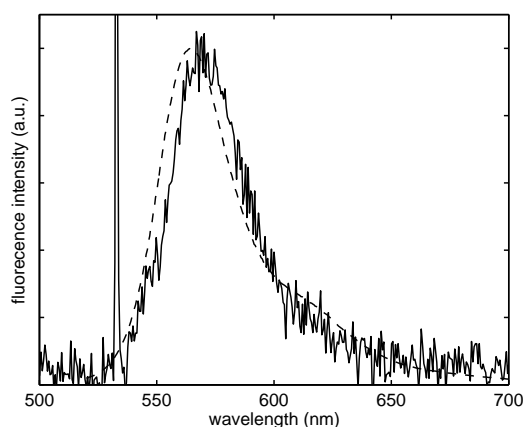


Figure 6.5: Comparison of the fluorescence spectrum of RhB in methanol (dashed) and the averaged spectrum from the entire image area (solid).

spectra are summed together, the excitation peak clearly arises and its amplitude is higher than that of RhB fluorescence band. This is not surprising since only few spots contribute to the fluorescence signal while the background signal comes from entire area of the image. It seems, however, that this “leaked” excitation light is the only significant contribution to the background signal.

The scanning speed during the spectral imaging (figure 6.4) was set very low in order to “harvest” as many photons as possible from each molecule in the scanned area. The pixel size is roughly matching the size of the area illuminated by the excitation light. Therefore, a fluorophore is continuously excited for the duration of the pixel integration time which was 1 s. This value exceeds the estimated photobleaching time for Rh6G tenfold. Since the photobleaching time for RhB can be expected to be of the same order as for Rh6G, it can be expected that most fluorophores in the scanned area would be destroyed after such exposure.

Figure 6.6 a) shows a fast intensity image scan of RhB molecules on a glass substrate recorded with APD. Five microlitres of 2×10^{-9} M dye solution were deposited on the substrate. The surface density of fluorophores is obviously higher than in figure 6.2. Intensity scan of the same sample shown in figure 6.6 b) was performed on an area previously scanned slowly in the spectral imaging mode (using the spectrograph) with settings similar to the scan shown in figure 6.4. It is obvious that a vast majority of fluorophores were indeed destroyed during the spectral imaging and the area is nearly perfectly bleached.

6.2.4 Allophycocyanin single molecule fluorescence

Utilising the protocol presented in section 4.3, allophycocyanin (APC) molecules in the trimeric form can be immobilized in a silica sol-gel monolith in order to facilitate true single protein investigations under controlled conditions. Figure 6.7 shows a typical confocal image recorded on a sol-gel prepared according to

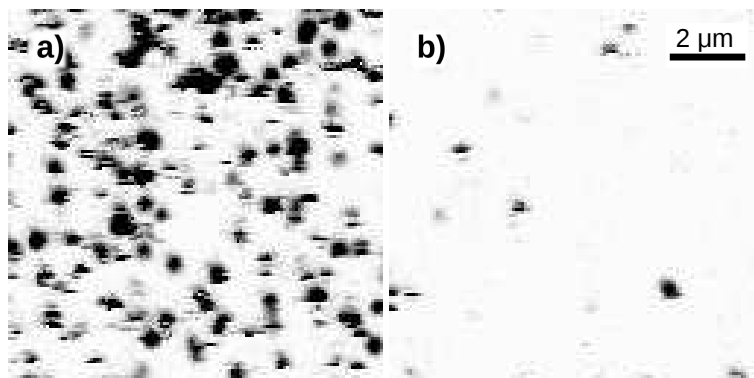


Figure 6.6: Devastating consequences of single molecule spectra measurement. A fluorescence intensity image of the sample before (a) and after spectral imaging scan (b).

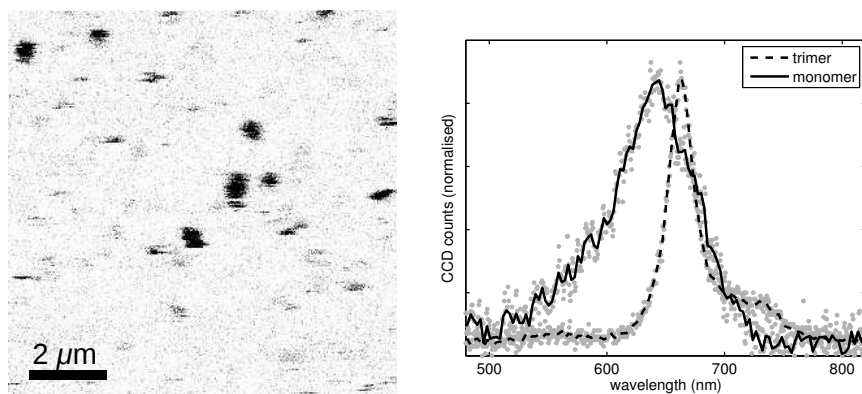


Figure 6.7: Single molecule APC fluorescence in sol-gel nano-pores. Fluorescence intensity image (**left**). Trimer and monomer fluorescence spectra for single APC molecules entrapped in the pores of the sol-gel monolith (**right**). The trimer spectrum was recorded using a sol-gel monolith prepared as described here with methanol removed as opposed to the monomer spectrum recorded in a monolith with methanol present and without pH adjustment. The spectra have been normalised to equal intensity and the baseline set to zero.

the new protocol. Fluorescence from individual APC molecules is clearly shown. The APC concentration was $\leq 10^{-9}$ mol dm $^{-3}$ and the sol was applied onto a microscope slide and then allowed to gel. Images were obtained by focusing the laser ~ 1 μ m beneath the sample surface and collecting the fluorescence through a 645 nm Schott long pass filter. The single molecule images display a range of sizes and shapes as the fluorophore is sometime bleached during a sample scan.

Figure 6.7 also shows the corresponding single-molecule emission spectra to be consistent with APC in the trimeric form. For comparison the emission spectrum recorded on APC under the same conditions but with methanol present due to incomplete hydrolysis is also shown. In the latter case, APC is clearly shown to be dissociated into the monomeric form.

6.3 Summary and discussion

Experiments with standard reference samples demonstrated that fluorescence of single immobilised molecules can be imaged using commercial α -SNOM microscope. The microscope was later equipped with a spectrograph to allow Raman confocal microscopy. The detection efficiency of the upgraded instrument is sufficient for recording a fluorescence emission spectrum from a single molecule. The measurement procedure is as follows: i) The detectability of individual immobilised fluorophores is first assured by a few (relatively) fast scans of different areas of the sample using a single channel detector (APD). The focusing and excitation intensity are optimised to yield the highest possible signal-to-noise ratio. ii) The detector is swapped by coupling the output multimode fibre to the spectrograph and slow scan is performed while a complete spectrum is recorded from each point of the scanned area. The performance of both single molecule imaging and spectroscopy is limited by the slow scanning speed, which is necessary to reach reasonable SNR, and by the photobleaching phenomenon.

Direct observations of fluorophore diffusion using single molecule imaging have been reported [125, 126]. The time needed to acquire an intensity image of individual fluorophores with reasonable resolution and SNR was typically several minutes when using scanning confocal microscopy with α -SNOM. This somewhat limits the range of diffusion rates that can be observed using this method. Bopp *et al.* [125] studied single molecule diffusion in a polymer film using SNOM with sequence period 13 min, which is similar to what can be achieved with α -SNOM. They report the average diffusion constant of Rh6G in a polyvinylbutyral film to be $D = 2.6 \pm 0.2 \times 10^{-15}$ cm 2 s $^{-1}$. A different experimental setup must be used to track a single molecule diffusing at higher speeds. Imaging with CCD camera is more suitable than scanning confocal microscopy because it allows to take an image of entire observed area at once. For example, diffusion of streptocyanine molecules in the porous silica sol-gel with $D = 4.7 \times 10^{-9}$ cm 2 s $^{-1}$ was monitored using a wide-field imaging setup [126] which allowed to record a short clip with up to 28 s $^{-1}$ frame rate.

The spectral resolution of the single molecule spectrum measurement is sufficient to observe larger shifts. Thus, the instrument can be used for example to investigate inhomogeneous local environment of fluorescent probes immobilised in a transparent host or on a surface. Less subtle changes in spectral position and shape can not be accurately measured due to the scarceness of data. Single molecule spectral diffusion, i.e., different spectra observed for the

same fluorophore at different times, at room temperature has been reported [2, 14, 127, 128]. Similar studies might be difficult to perform with α -SNOM since most fluorophores bleached during the time needed to obtain a single molecule spectrum.

Badan-labelled glucose binding protein described in chapter 5, together with single molecule detection technique, gives an opportunity for glucose sensing at ultimate single molecule level. A suitable host material must be employed for this purpose, which would prevent the translation diffusion of the protein while the substrate molecules (glucose) would be allowed to diffuse to reach the receptor. This can be accomplished by using for example polyacrylamide or agarose gels or a modified silica sol-gel such as that prepared by the method described in section 4.3. Non-fluorescent substrate – glucose – would be detected by enhancement of fluorescence emission from single immobilised badan-BGP152C. Imaging of the unbound form of the protein might be difficult or even impossible due to its low quantum yield. The difference of the peak emission wavelength between the bound and unbound protein might be too small to be reliably resolved in spectra of individual molecules (recall the limited amount of data available from each molecule). However, the analysis of intensity fluctuations of single molecule fluorescence can be used to study binding kinetics – measurement of association and dissociation rates of the reaction [5].

Single molecule imaging and spectroscopy of badan-GBP152C using α -SNOM is not straightforward because the instrument is optimised to work on a 532 nm wavelength which is not suitable for excitation of the protein. To allow measurements using 400 nm excitation light (badan-GBP152C absorption maximum) some of the optics would have to be replaced – single mode fibre, dichroic beam splitter, holographic edge filter. Conventional microscope objectives are designed to work in the visible range of wavelengths. The 400 nm wavelength is on the edge of their best performance, especially due to the limited transmittance of the anti-reflection coating and cementing material in the UV region.

In general, it is difficult to reach high SNR in single molecule studies in the UV spectral region. The background signal due to Rayleigh scattering increases with the fourth power of the excitation light frequency. Although imaging of single molecules in deep UV region at room temperature has been reported [130, 131], a majority of single molecule studies involve photostable red dyes such as rhodamines, Cy3, Cy5, DiI and Texas red. These dyes have high molar absorption coefficients and can be excited by popular Argon (514 nm) and Nd:YAG lasers (532 nm – second harmonic). Also, they emit in the region where the quantum efficiency of silicon-based detectors is highest (red – near infra-red). Therefore, from the perspective of single-molecule sensing, an analogous system to badan-GBP152C which would be possible to excite with green light would be desirable.

Chapter 7

Conclusion

Fluorescence spectroscopy was applied to study the interaction between cationic laser dye rhodamine 6G and SiO₂ nanoparticles in colloidal aqueous solutions. It was discovered that multiple labelling of one silica particle leads to significant aggregation of the dye. Unfortunately, due to the inaccuracy of estimation of the particle concentration in the colloids, the probability of occurrence of two fluorophores on one particle could not be reliably correlated with the concentration of dimers. Formation of non-fluorescent aggregates leads to selective quenching of dye that is non-covalently attached to the surface of particles. This mechanism is probably responsible for faster fluorescence depolarisation with increasing number of dye molecules per particle. No experimental evidence was found that would indicate fluorescence depolarisation mechanism other than Brownian rotation of labelled silica nanoparticles and free fluorophores. The presented work could be extended by an experimental study of various factors affecting the formation of dye aggregates and their fluorescent or non-fluorescent character (e.g. addition of surfactants or co-solvents). Results could have implications for research on dye-doped solids or particle labelling.

Quenching of perylene fluorescence by cobalt ions in silica sol-gels was studied in order to reveal the mechanism of quenching and explain its enhancement with increasing polymerisation time. It was proposed that collisions due to diffusion can be the dominant mechanism of the quenching. The deviation of recorded fluorescence decay kinetics might be caused by the transient effect in collisional quenching. No information was found that would contradict this hypothesis. However, the environment in sol-gel is strongly inhomogeneous and the nature of the interaction between the dye and the quencher may vary considerably on a microscale. Thus, the system is probably too complex to be studied by the used methods.

Polarity-sensitive dye prodan was used to define an optimal protocol for encapsulation of an environment sensitive protein in a water-filled inorganic silica matrix. Prodan was used to determine the optimal timing for removal of methanol which is released during the sol-gel process. The presence of methanol is undesirable because it often leads to denaturation of biomolecules through alteration of their native structure. The biocompatibility of the material prepared according to the developed protocol was demonstrated by successful encapsulation of protein allophycocyanin, preserving its native trimeric form for up to 500 h. The improved stability afforded by the protocol has potential impact in

nanomedicine where the ability to study single biomolecules is a primary goal as it underpins our understanding of disease pathology and therapeutics at the most fundamental level.

The photophysics was studied of a H152C mutant of glucose/galactose binding protein labelled with polarity-sensitive reactive dye, badan. Badan-GBP152C exhibits a large change of fluorescence intensity as a consequence of glucose concentration increase. This makes badan-GBP152C a promising candidate for construction of inexpensive fluorescence-based glucose sensor for clinical use. The analysis of spectroscopic data is somewhat complicated by the heterogeneity of the ensemble – it contains bound and unbound forms of the protein and possibly also a small fraction of non-specifically labelled specimens. The use of single-molecule fluorescence spectroscopy would allow to study both populations separately and might give valuable information about the glucose binding process. However, the excitation wavelength required for photoexcitation of badan-GBP152C was not compatible with the available instrument capable to perform single molecule spectroscopy.

The applicability of commercial scanning confocal/SNOM/AFM microscope α -SNOM (WITec GmbH, Germany) for single molecule fluorescence imaging and emission spectroscopy was demonstrated by measurements on a standard reference sample – fluorescent dye Rhodamine B adsorbed on a glass surface. The detection sensitivity of the system is high enough to detect a single fluorophore and even to record its emission spectrum. The microscope can be used for spectroscopy analysis of strongly heterogeneous samples, where ensemble averaging needs to be avoided. The imaging feature of the microscope allows single molecule measurements on immobilised fluorophores. Fluorescence from a single molecule can thus be monitored for a period limited only by the photostability of the studied specimen.

Bibliography

- [1] T. Basché, S. Xie, W.E. Moerner, M. Orrit, and U.P. Wild. *Single-molecule optical detection, imaging and spectroscopy*. VCH Weinheim, 1997.
- [2] W.E. Moerner. A dozen years of single-molecule spectroscopy in physics, chemistry, and biophysics. *J. Phys. Chem. B*, 106(5):910–927, 2002.
- [3] M. Orrit and J. Bernard. Single pentacene molecules detected by fluorescence excitation in a p-terphenyl crystal. *Physical review letters*, 65(21):2716–2719, 1990.
- [4] W.E. Moerner and D.P. Fromm. Methods of single-molecule fluorescence spectroscopy and microscopy. *Review of Scientific Instruments*, 74(8):3597–3619, 2003.
- [5] J. R. Lakowicz. *Principles of Fluorescence Spectroscopy*. Springer, third edition, 2006.
- [6] W.E. Moerner and M. Orrit. Illuminating single molecules in condensed matter. *Science*, 283(5408):1670, 1999.
- [7] C. Gell, D. Brockwell, and D.A. Smith. *Handbook of single molecule fluorescence spectroscopy*. Oxford University Press, USA, 2006.
- [8] M. Kumbhakar, S. Nath, T. Mukherjee, J.P. Mittal, and H. Pal. Single-molecule detection in exploring nanoenvironments: an overview. *Journal of Photochemistry and Photobiology C: Photochemistry Reviews*, 5(2):113–137, 2004.
- [9] M.J. Levene, J. Korlach, S.W. Turner, M. Foquet, H.G. Craighead, and W.W. Webb. Zero-mode waveguides for single-molecule analysis at high concentrations. *Science*, 299(5607):682, 2003.
- [10] M. Foquet, K.T. Samiee, X. Kong, B.P. Chauduri, P.M. Lundquist, S.W. Turner, J. Freudenthal, and D.B. Roitman. Improved fabrication of zero-mode waveguides for single-molecule detection. *Journal of Applied Physics*, 103:034301, 2008.
- [11] R.X. Bian, R.C. Dunn, X.S. Xie, and PT Leung. Single molecule emission characteristics in near-field microscopy. *Physical review letters*, 75(26):4772–4775, 1995.

-
- [12] L. Brand, C. Eggeling, C. Zander, K.H. Drexhage, and C.A.M. Seidel. Single-molecule identification of Coumarin-120 by time-resolved fluorescence detection: comparison of one- and two-photon excitation in solution. *J. Phys. Chem. A*, 101(24):4313–4321, 1997.
- [13] E.J. Sanchez, L. Novotny, G.R. Holtom, and X.S. Xie. Room-temperature fluorescence imaging and spectroscopy of single molecules by two-photon excitation. *J. Phys. Chem. A*, 101(38):7019–7023, 1997.
- [14] M.A. Weber, F. Stracke, and A.J. Meixner. Dynamics of single dye molecules observed by confocal imaging and spectroscopy. *Cytometry Part A*, 36(3):217–223, 1999.
- [15] S. Brasselet, E.J.G. Peterman, A. Miyawaki, and W.E. Moerner. Single-molecule fluorescence resonant energy transfer in calcium concentration dependent cameleon. *J. Phys. Chem. B*, 104(15):3676–3682, 2000.
- [16] G. Chirico, F. Cannone, S. Beretta, A. Diaspro, B. Campanini, S. Bettati, R. Ruotolo, and A. Mozzarelli. Dynamics of green fluorescent protein mutant2 in solution, on spin-coated glasses, and encapsulated in wet silica gels. *Protein Science*, 11(5):1152–1161, 2002.
- [17] M. Böhmer and J. Enderlein. Fluorescence spectroscopy of single molecules under ambient conditions: Methodology and technology. *ChemPhysChem*, 4(8):792–808, 2003.
- [18] J. Enderlein. Single molecule spectroscopy: basics and applications. In M. Hof, R. Hutterer, and V. Fidler, editors, *Fluorescence spectroscopy in biology*, Springer Series on Fluorescence, chapter 7, pages 104–130. Springer Berlin Heidelberg, 2005.
- [19] R. Rigler and H. Vogel. *Single molecules and nanotechnology*. Springer Verlag, 2008.
- [20] X. Michalet, S. Weiss, and M. Jaeger. Single-molecule fluorescence studies of protein folding and conformational dynamics. *Chem. Rev*, 106(5):1785–1813, 2006.
- [21] E.J.G. Peterman, S. Brasselet, and W.E. Moerner. The fluorescence dynamics of single molecules of green fluorescent protein. *J. Phys. Chem. A*, 103(49):10553–10560, 1999.
- [22] S. Weiss. Fluorescence spectroscopy of single biomolecules. *Science*, 283(5408):1676, 1999.
- [23] B. Schuler and W.A. Eaton. Protein folding studied by single-molecule FRET. *Current opinion in structural biology*, 18(1):16–26, 2008.
- [24] J. Eid, A. Fehr, J. Gray, K. Luong, J. Lyle, G. Otto, P. Peluso, D. Rank, P. Baybayan, B. Bettman, et al. Real-time DNA sequencing from single polymerase molecules. *Science*, 323(5910):133, 2009.

- [25] P.M. Lundquist, C.F. Zhong, P. Zhao, A.B. Tomaney, P.S. Peluso, J. Dixon, B. Bettman, Y. Lacroix, D.P. Kwo, E. McCullough, et al. Parallel confocal detection of single molecules in real time. *Optics letters*, 33(9):1026–1028, 2008.
- [26] G. Macnaught. *Characterisation of fluorescence nanotomography: A method for recovering the donor-acceptor distance distribution from FRET-modified fluorescence decays*. PhD thesis, University of Strathclyde, Department of Physics, 2006.
- [27] F. Khan, L. Gnudi, and J.C. Pickup. Fluorescence-based sensing of glucose using engineered glucose/galactose-binding protein: A comparison of fluorescence resonance energy transfer and environmentally sensitive dye labelling strategies. *Biochemical and biophysical research communications*, 365(1):102–106, 2008.
- [28] A. Einstein. Strahlungs-emission und absorption nach der quantentheorie. *Deutsche Physikalische Gesellschaft*, 18:318–323, 1916.
- [29] W.H. Louisell. *Quantum statistical properties of radiation*. John Wiley & Sons, Inc., 1973.
- [30] P. Atkins and J. de Paula. *Physical chemistry*. Oxford University Press, eighth edition, 2006.
- [31] P.F. Bernath. *Spectra of atoms and molecules*. Oxford University Press, 1995.
- [32] W. Demtröder. *Laser spectroscopy*. Springer, third edition, 2002.
- [33] R. Jimenez, G.R. Fleming, P.V. Kumar, and M. Maroncelli. Femtosecond solvation dynamics of water. *Nature*, 369(6480):471–473, 1994.
- [34] J. Sýkora, P. Kapusta, V. Fidler, and M. Hof. On what time scale does solvent relaxation in phospholipid bilayers happen? *Langmuir*, 18(3):571–574, 2002.
- [35] A. Szabo. Theory of diffusion-influenced fluorescence quenching. *The Journal of Physical Chemistry*, 93(19):6929–6939, 1989.
- [36] W.R. Ware and T.L. Nemzek. The direct observation of transient effects in diffusion-controlled fluorescence quenching. *Chemical Physics Letters*, 23(4):557–560, 1973.
- [37] J.C. Andre, M. Niclause, and W.R. Ware. Kinetics of partly diffusion controlled reactions. I. Transient and apparent transient effect in fluorescence quenching. *Chemical Physics*, 28(3):371–377, 1978.
- [38] J.C. Andre, M. Bouchy, and W.R. Ware. Kinetics of partly diffusion controlled reactions. III. Competition between physical and chemical kinetics. Experimental results. *Chemical Physics*, 37(1):119–131, 1979.
- [39] Jobin Yvon IBH. *DAS6 Fluorescence Decay Analysis Software*, 2002. User guide.

-
- [40] D.V. O'Connor and D. Phillips. *Time-correlated single photon counting*. Academic Press, London, 1984.
- [41] W. Ibach and O. Hollricher. *High resolution optical microscopy*. WITec Wissenschaftliche Instrumente und Technologie GmbH, 2002. Tutorial.
- [42] B.E.A. Saleh and M.C. Teich. *Fundamentals of photonics*. John Wiley & Sons, Inc., 1991.
- [43] WITec Wissenschaftliche Instrumente und Technologie GmbH. *Alpha-SNOM operation manual*, 2002. User guide.
- [44] R. Eckert, J.M. Freyland, H. Gersen, H. Heinzelmann, G. Schürmann, W. Noell, U. Staufer, and N.F. de Rooij. Near-field fluorescence imaging with 32 nm resolution based on microfabricated cantilevered probes. *Applied Physics Letters*, 77:3695, 2000.
- [45] E.A. Burstein and V.I. Emelyanenko. Log-normal description of fluorescence spectra of organic fluorophores. *Photochemistry and Photobiology*, 64(2):316–320, 1996.
- [46] E.A. Burstein, S.M. Abornev, and Y.K. Reshetnyak. Decomposition of protein tryptophan fluorescence spectra into log-normal components. I. Decomposition algorithms. *Biophysical Journal*, 81(3):1699–1709, 2001.
- [47] V.I. Emelyanenko and E.A. Burshtein. Analytical description of the fluorescence spectra of aromatic amino acids and proteins. *Journal of Applied Spectroscopy*, 65(3):372–378, 1998.
- [48] J. Hixon and Y.K. Reshetnyak. Algorithm for the analysis of tryptophan fluorescence spectra and their correlation with protein structural parameters. *Algorithms*, 2(3):1155–1176, 2009.
- [49] H. Langhals. A re-examination of the line shape of the electronic spectra of complex molecules in solution: log-normal function versus gaussian. *Spectrochimica Acta Part A: Molecular and Biomolecular Spectroscopy*, 56(11):2207–2210, 2000.
- [50] Y.K. Reshetnyak and E.A. Burstein. Decomposition of protein tryptophan fluorescence spectra into log-normal components. II. The statistical proof of discreteness of tryptophan classes in proteins. *Biophysical Journal*, 81(3):1710–1734, 2001.
- [51] C.J. Brinker and G.W. Scherer. *Sol-gel science: the physics and chemistry of sol-gel processing*. Academic Press, 1990.
- [52] R. Gupta and N.K. Chaudhury. Entrapment of biomolecules in sol-gel matrix for applications in biosensors: Problems and future prospects. *Biosensors and Bioelectronics*, 22(11):2387–2399, 2007.
- [53] K. Apperson, J. Karolin, R.W. Martin, and D.J.S. Birch. Nanoparticle metrology standards based on the time-resolved fluorescence anisotropy of silica colloids. *Measurement Science and Technology*, 20:025310, 2009.

- [54] C.D. Geddes, K. Apperson, and D.J.S. Birch. New fluorescent quinolinium dyes – applications in nanometre particle sizing. *Dyes and Pigments*, 44(2):69–74, 2000.
- [55] C.D. Geddes and D.J.S. Birch. Nanometre resolution of silica hydrogel formation using time-resolved fluorescence anisotropy. *Journal of Non-Crystalline Solids*, 270(1-3):191–204, 2000.
- [56] D.J.S. Birch and C.D. Geddes. Sol-gel particle growth studied using fluorescence anisotropy: An alternative to scattering techniques. *Physical Review E*, 62(2):2977–2980, 2000.
- [57] A. Cleary, J. Karolin, and D.J.S. Birch. pH tracking of silica hydrogel nanoparticle growth. *Applied Physics Letters*, 89(11):113125, 2009.
- [58] T.A. Kikteva, B.V. Zhmud, N.P. Smirnova, A.M. Eremenko, Y. Plevaya, and M. Ottolenghi. Probing the sol-gel conversion in the tetraethoxysilane/alcohol/water system with the aid of diffusion-controlled fluorescence quenching. *Journal of colloid and interface science*, 193(2):163–166, 1997.
- [59] N. Negishi, T. Fujii, and M. Anpo. Characteristics of the fluorescence spectra of pyrene molecules during the sol to gel to xerogel transitions of silica-titania binary oxide systems. *Langmuir*, 9(11):3320–3323, 1993.
- [60] E. I. du Pont de Nemours & Co. *Ludox colloidal silica: properties, uses, storage and handling*, 1987. Datasheet.
- [61] D. Magde, R. Wong, and P.G. Seybold. Fluorescence quantum yields and their relation to lifetimes of rhodamine 6G and fluorescein in nine solvents: Improved Absolute Standards for Quantum Yields. *Photochemistry and photobiology*, 75(4):327–334, 2002.
- [62] A.N. Watkins, C.M. Ingersoll, G.A. Baker, and F.V. Bright. A parallel multiharmonic frequency-domain fluorometer for measuring excited-state decay kinetics following one-, two-, or three-photon excitation. *Analytical Chemistry*, 70(16):3384–3396, 1998.
- [63] F.V. Bright. A new fiber-optic-based multifrequency phase-modulation fluorometer. *Applied Spectroscopy*, 42(8):1531–1537, 1988.
- [64] F. Olivini, S. Beretta, and G. Chirico. Two-photon fluorescence polarization anisotropy decay on highly diluted solutions by phase fluorometry. *Appl. Spectrosc.*, 55(3):311–317, 2001.
- [65] O. Valdes-Aguilera and DC Neckers. Aggregation phenomena in xanthene dyes. *Accounts of Chemical Research*, 22(5):171–177, 1989.
- [66] D. Toptygin, B.Z. Packard, and L. Brand. Resolution of absorption spectra of rhodamine 6G aggregates in aqueous solution using the law of mass action. *Chemical Physics Letters*, 277(5-6):430–435, 1997.
- [67] K. Kemnitz and K. Yoshihara. Entropy-driven dimerization of xanthene dyes in nonpolar solution and temperature-dependent fluorescence decay of dimers. *The Journal of Physical Chemistry*, 95(16):6095–6104, 1991.

- [68] K. Kemnitz, N. Tamai, I. Yamazaki, N. Nakashima, and K. Yoshihara. Fluorescence decays and spectral properties of rhodamine B in submono-, mono-, and multilayer systems. *The Journal of Physical Chemistry*, 90(21):5094–5101, 1986.
- [69] S. Salleres, F.L. Arbeloa, V. Martínez, T. Arbeloa, and I.L. Arbeloa. Adsorption of fluorescent R6G dye into organophilic C12TMA laponite films. *Journal of colloid and interface science*, 321(1):212–219, 2008.
- [70] H. Wang, Q. Yang, L. Sun, S. Wang, W. Wang, C. Zhang, Y. Li, S. Xu, and Y. Li. Aggregation states of rhodamine 6G in electrospun nanofibrous films. *Journal of colloid and interface science*, 341(2):224–231, 2010.
- [71] A. Anedda, C.M. Carbonaro, R. Corpino, P.C. Ricci, S. Grandi, and P.C. Mustarelli. Formation of fluorescent aggregates in Rhodamine 6G doped silica glasses. *Journal of Non-Crystalline Solids*, 353(5-7):481–485, 2007.
- [72] S. Błoński. Aggregation of rhodamine 6g in porous silica gels. *Chemical Physics Letters*, 184(1-3):229–234, 1991.
- [73] L. Malfatti, T. Kidchob, D. Aiello, R. Aiello, F. Testa, and P. Innocenzi. Aggregation states of rhodamine 6G in mesostructured silica films. *The Journal of Physical Chemistry C*, 112(42):16225–16230, 2008.
- [74] F. del Monte, J.D. Mackenzie, and D. Levy. Rhodamine fluorescent dimers adsorbed on the porous surface of silica gels. *Langmuir*, 16(19):7377–7382, 2000.
- [75] F. del Monte, M.L. Ferrer, and D. Levy. Preferred formation of coplanar inclined fluorescent J-dimers in rhodamine 101 doped silica gels. *Langmuir*, 17(16):4812–4817, 2001.
- [76] M. Kasha, H.R. Rawls, and M.A. El-Bayoumi. The exciton model in molecular spectroscopy. *Pure Appl. Chem*, 11(3-4):371–392, 1965.
- [77] T. Salthammer, H. Dreeskamp, D.J.S. Birch, and R.E. Imhof. Fluorescence quenching of perylene by Co^{2+} ions via energy transfer in viscous and non-viscous media. *Journal of Photochemistry and Photobiology A: Chemistry*, 55(1):53–62, 1990.
- [78] A.S. Holmes, D.J.S. Birch, K. Suhling, R.E. Imhof, T. Salthammer, and H. Dreeskamp. Evidence for donor–donor energy transfer in lipid bilayers: perylene fluorescence quenching by Co^{2+} ions. *Chemical Physics Letters*, 186(2-3):189–194, 1991.
- [79] A.S. Holmes, D.J.S. Birch, and T. Salthammer. Quenching of perylene fluorescence by Co^{2+} ions in dipalmitoylphosphatidylcholine (DPPC) vesicles. *Journal of Fluorescence*, 3(2):77–84, 1993.
- [80] A.S. Holmes, K. Suhling, and D.J.S. Birch. Fluorescence quenching by metal ions in lipid bilayers. *Biophysical Chemistry*, 48(2):193–204, 1993.
- [81] O.J. Rolinski, D.J.S. Birch, L.J. McCartney, and J.C. Pickup. A method of determining donor-acceptor distribution functions in Förster resonance energy transfer. *Chemical Physics Letters*, 324(1-3):95–100, 2000.

- [82] O. Rolinski and D. Birch. Fluorescence nanotomography: Recent progress, constraints and opportunities. In M. Hof, R. Hutterer, and V. Fidler, editors, *Fluorescence Spectroscopy in Biology*, Springer Series on Fluorescence, chapter 4, pages 56–70. Springer, 2005.
- [83] M. Arduini, L. Armelao, S. Gross, F. Mancin, S. Marcuz, M. Montolli, and C. Sada. Chemical optimisation of a sol-gel procedure for the development of fluorescence Cu (II) nanosensors. *Applied Surface Science*, 253(17):7178–7187, 2007.
- [84] D. Balköse, U. Köktürk, and H. Yilmaz. A study of cobaltous chloride dispersion on the surface of the silica gel. *Applied Surface Science*, 147(1-4):77–84, 1999.
- [85] V.S. Gladkikh, A.I. Burshtein, H.L. Tavernier, and M.D. Fayer. Influence of diffusion on the kinetics of donor-acceptor electron transfer monitored by the quenching of donor fluorescence. *J. Phys. Chem. A*, 106(30):6982–6990, 2002.
- [86] W. Jin and J.D. Brennan. Properties and applications of proteins encapsulated within sol-gel derived materials. *Analytica Chimica Acta*, 461(1):1–36, 2002.
- [87] I. Gill and A. Ballesteros. Encapsulation of biologicals within silicate, siloxane, and hybrid sol-gel polymers: An efficient and generic approach. *J. Am. Chem. Soc.*, 120(34):8587–8598, 1998.
- [88] R.B. Bhatia, C.J. Brinker, A.K. Gupta, and A.K. Singh. Aqueous sol-gel process for protein encapsulation. *Chem. Mater*, 12(8):2434–2441, 2000.
- [89] M.L. Ferrer, F. del Monte, and D. Levy. A novel and simple alcohol-free sol-gel route for encapsulation of labile proteins. *Chem. Mater*, 14(9):3619–3621, 2002.
- [90] L. Ying and X.S. Xie. Fluorescence spectroscopy, exciton dynamics, and photochemistry of single allophycocyanin trimers. *J. Phys. Chem. B*, 102(50):10399–10409, 1998.
- [91] Z. Chen, DL Kaplan, K. Yang, J. Kumar, KA Marx, and SK Tripathy. Phycobiliproteins encapsulated in sol-gel glass. *Journal of Sol-Gel Science and Technology*, 7(1):99–108, 1996.
- [92] R. MacColl, K. Csatorday, D.S. Berns, and E. Traeger. Chromophore interactions in allophycocyanin. *Biochemistry*, 19(12):2817–2820, 1980.
- [93] J.C. Pickup, F. Hussain, N.D. Evans, O.J. Rolinski, and D.J.S. Birch. Fluorescence-based glucose sensors. *Biosensors and Bioelectronics*, 20(12):2555–2565, 2005.
- [94] O.J. Rolinski, D.J.S. Birch, L.J. McCartney, and J.C. Pickup. A time-resolved near-infrared fluorescence assay for glucose: opportunities for trans-dermal sensing. *Journal of Photochemistry and Photobiology B: Biology*, 54(1):26–34, 2000.

- [95] OJ Rolinski, DJS Birch, LJ McCartney, and JC Pickup. Sensing metabolites using donor–acceptor nanodistributions in fluorescence resonance energy transfer. *Applied Physics Letters*, 78:2796, 2001.
- [96] C.D. McGuinness, K. Sagoo, D. McLoskey, and D.J.S. Birch. Selective excitation of tryptophan fluorescence decay in proteins using a subnanosecond 295 nm light-emitting diode and time-correlated single-photon counting. *Applied Physics Letters*, 86(26):261911, 2005.
- [97] A. Cleary, A. Glidle, PJR Laybourn, S. Garcia-Blanco, S. Pellegrini, C. Helfter, GS Buller, JS Aitchison, and JM Cooper. Integrating optics and microfluidics for time-correlated single-photon counting in lab-on-a-chip devices. *Applied Physics Letters*, 91:071123, 2007.
- [98] DJS Birch, AS Holmes, and M. Darbyshire. Intelligent sensor for metal ions based on fluorescence resonance energy transfer. *Measurement Science and Technology*, 6:243, 1995.
- [99] O.J. Rolinski and D.J.S. Birch. A fluorescence lifetime sensor for Cu(I) ions. *Measurement Science and Technology*, 10:127, 1999.
- [100] D.J.S. Birch, A.S. Holmes, J.R. Gilchrist, R.E. Imhof, S.M. Alawi, and B. Nadolski. A multiplexed single-photon instrument for routine measurement of time-resolved fluorescence anisotropy. *Journal of Physics E: Scientific Instruments*, 20:471, 1987.
- [101] G. Weber and F.J. Farris. Synthesis and spectral properties of a hydrophobic fluorescent probe: 6-propionyl-2-(dimethylamino) naphthalene. *Biochemistry*, 18(14):3075–3078, 1979.
- [102] N.K. Vyas, M.N. Vyas, and F.A. Quiocho. Sugar and signal-transducer binding sites of the Escherichia coli galactose chemoreceptor protein. *Science*, 242(4883):1290, 1988.
- [103] J.C. Pickup, Z.L. Zhi, F. Khan, T. Saxl, and D.J.S. Birch. Nanomedicine and its potential in diabetes research and practice. *Diabetes/metabolism research and reviews*, 24(8):604–610, 2008.
- [104] M. Ormo, A.B. Cubitt, K. Kallio, L.A. Gross, R.Y. Tsien, S.J. Remington, et al. Crystal structure of the Aequorea victoria green fluorescent protein. *Science(Washington)*, 273(5280):1392–1392, 1996.
- [105] M. Chalfie, Y. Tu, G. Euskirchen, W.W. Ward, D.C. Prasher, et al. Green fluorescent protein as a marker for gene expression. *Science*, 263(5148):802–805, 1994.
- [106] L. Tolosa, I. Gryczynski, L.R. Eichhorn, J.D. Dattelbaum, F.N. Castellano, G. Rao, and J.R. Lakowicz. Glucose sensor for low-cost lifetime-based sensing using a genetically engineered protein. *Analytical biochemistry*, 267(1):114–120, 1999.
- [107] V. Scognamiglio, V. Aurilia, N. Cennamo, P. Ringhieri, L. Iozzino, M. Tartaglia, M. Staiano, G. Ruggiero, P. Orlando, T. Labella, L. Zeni, A. Vitale, and S. D’Auria. D-galactose/D-glucose-binding protein from

- Escherichia coli as probe for a non-consuming glucose implantable fluorescence biosensor. *Sensors*, 7(10):2484–2491, 2007.
- [108] S. D’Auria, A. Ausili, A. Marabotti, A. Varriale, V. Scognamiglio, M. Staiano, E. Bertoli, M. Rossi, and F. Tanfani. Binding of glucose to the *d*-galactose/*d*-glucose-binding protein from escherichia coli restores the native protein secondary structure and thermostability that are lost upon calcium depletion. *Journal of biochemistry*, 139(2):213, 2006.
- [109] T. Saxl, F. Khan, D.R. Matthews, Z.L. Zhi, O. Rolinski, S. Ameer-Beg, and J. Pickup. Fluorescence lifetime spectroscopy and imaging of nano-engineered glucose sensor microcapsules based on glucose/galactose-binding protein. *Biosensors and Bioelectronics*, 24(11):3229–3234, 2009.
- [110] F. Khan, T.E. Saxl, and J.C. Pickup. Fluorescence intensity-and lifetime-based glucose sensing using an engineered high- K_d mutant of glucose/galactose-binding protein. *Analytical biochemistry*, 399(1):39–43, 2010.
- [111] P. Jurkiewicz, J. Sýkora, A. Olżyńska, J. Humpolíčková, and M. Hof. Solvent relaxation in phospholipid bilayers: Principles and recent applications. *Journal of Fluorescence*, 15(6):883–894, 2005.
- [112] P. Abbyad, X. Shi, W. Childs, T.B. McAnaney, B.E. Cohen, and S.G. Boxer. Measurement of solvation responses at multiple sites in a globular protein. *J. Phys. Chem. B*, 111(28):8269–8276, 2007.
- [113] R.B.M. Koehorst, S. Laptinok, B. van Oort, A. van Hoek, R.B. Spruijt, I.H.M. van Stokkum, H. van Amerongen, and M.A. Hemminga. Profiling of dynamics in protein-lipid-water systems: a time-resolved fluorescence study of a model membrane protein with the label BADAN at specific membrane depths. *European Biophysics Journal*, 39(4):647–656, 2010.
- [114] M. Vincent, B. de Foresta, and J. Gallay. Nanosecond dynamics of a mimicked membrane-water interface observed by time-resolved Stokes shift of LAURDAN. *Biophysical journal*, 88(6):4337–4350, 2005.
- [115] M. Viard, J. Gallay, M. Vincent, O. Meyer, B. Robert, and M. Paternostre. Laurdan solvatochromism: solvent dielectric relaxation and intramolecular excited-state reaction. *Biophysical journal*, 73(4):2221–2234, 1997.
- [116] B.C. Lobo and C.J. Abelt. Does PRODAN possess a planar or twisted charge-transfer excited state? Photophysical properties of two PRODAN derivatives. *J. Phys. Chem. A*, 107(50):10938–10943, 2003.
- [117] A.B.J. Parusel, W. Nowak, S. Grimme, and G. Kohler. Comparative theoretical study on charge-transfer fluorescence probes: 6-propanoyl-2-(*N,N*-dimethylamino) naphthalene and derivatives. *J. Phys. Chem. A*, 102(36):7149–7156, 1998.
- [118] P. Anger, P. Bharadwaj, and L. Novotny. Enhancement and quenching of single-molecule fluorescence. *Phys. Rev. Lett.*, 96(11):113002, Mar 2006.

- [119] P. Bharadwaj, P. Anger, and L. Novotny. Nanoplasmonic enhancement of single-molecule fluorescence. *Nanotechnology*, 18(4):044017, 2007.
- [120] F. Vargas, O. Hollricher, O. Marti, G. De Schaetzen, and G. Tarrach. Influence of protective layers on the blinking of fluorescent single molecules observed by confocal microscopy and scanning near field optical microscopy. *Journal of Chemical Physics*, 117(2):866–871, 2002.
- [121] C. Eggeling, J. Widengren, R. Rigler, and C.A.M. Seidel. Photobleaching of fluorescent dyes under conditions used for single-molecule detection: evidence of two-step photolysis. *Anal. Chem*, 70(13):2651–2659, 1998.
- [122] C. Eggeling, A. Volkmer, and C.A.M. Seidel. Molecular photobleaching kinetics of rhodamine 6G by one- and two-photon induced confocal fluorescence microscopy. *ChemPhysChem*, 6(5):791–804, 2005.
- [123] D.S. English, A. Furube, and P.F. Barbara. Single-molecule spectroscopy in oxygen-depleted polymer films. *Chemical Physics Letters*, 324(1-3):15–19, 2000.
- [124] L.A. Deschenes and D.A. Vanden Bout. Single molecule photobleaching: increasing photon yield and survival time through suppression of two-step photolysis. *Chemical Physics Letters*, 365(5-6):387–395, 2002.
- [125] M.A. Bopp, A.J. Meixner, G. Tarrach, I. Zschokke-Gränacher, and L. Novotny. Direct imaging single molecule diffusion in a solid polymer host. *Chemical Physics Letters*, 263(6):721–726, 1996.
- [126] C. Hellriegel, J. Kirstein, C. Bräuchle, V. Latour, T. Pigot, R. Olivier, S. Lacombe, R. Brown, V. Guieu, C. Payrastra, et al. Diffusion of single streptocyanine molecules in the nanoporous network of sol-gel glasses. *J. Phys. Chem. B*, 108(38):14699–14709, 2004.
- [127] H.P. Lu and X.S. Xie. Single-molecule spectral fluctuations at room temperature. *Nature*, 385(6612):143–146, 1997.
- [128] A.J. Meixner and M.A. Weber. Single molecule spectral dynamics at room temperature. *Journal of Luminescence*, 86(3-4):181–187, 2000.
- [129] T. Ha, T. Enderle, D.F. Ogletree, D.S. Chemla, P.R. Selvin, and S. Weiss. Probing the interaction between two single molecules: fluorescence resonance energy transfer between a single donor and a single acceptor. *Proceedings of the National Academy of Sciences of the United States of America*, 93(13):6264, 1996.
- [130] Q. Li, T. Ruckstuhl, and S. Seeger. Deep-UV laser-based fluorescence lifetime imaging microscopy of single molecules. *J. Phys. Chem. B*, 108(24):8324–8329, 2004.
- [131] Q. Li and S. Seeger. Label-free detection of single protein molecules using deep UV fluorescence lifetime microscopy. *Anal. Chem*, 78(8):2732–2737, 2006.